Numerical Simulations in Support of a Long-Term Test of Gas Production From Hydrate Accumulations on the Alaska North Slope: Water Production and Associated Design and Management Issues

George J. Moridis[*1,2], Matthew T Reagan[2] and Tianjia Huang[1]

1: Texas A&M University, Petroleum Engineering Dept., College Station, TX 77845

2: Lawrence Berkeley National Laboratory, Energy Geosciences Division, Berkeley, CA 94720

**Corresponding author: gjmoridis@lbl.gov*

ABSTRACT

We investigated by numerical simulation strategies for a long-term test of depressurization-induced gas production from the B1 Sand of Unit B at the Hydrate-01 Stratigraphic Test Well. The main objective of this study was to estimate fluid production rates (with emphasis on water production) under a variety of conditions and production scenarios, and contribute new insights to the design and management of the field test. In the first part of the study, we investigated system response to a three-step depressurization process using two limiting sets of flow properties—the expected maximum and minimum intrinsic and effective permeabilities—for the very heterogeneous reservoir. In the second part, we investigated the effect of production interval length and placement within the formation relative to the boundaries of the hydrate-bearing unit. The best-performing well configuration was used in the third part of the study, which used the most representative subsurface flow properties to investigate the effect of the depressurization strategy on production performance.

The best overall performance (largest gas production with modest water production and a strong response at the observation wells) was obtained with a 10 m long well situated 3 m below the top of the formation and a three-step depressurization scheme at 15-day intervals to a terminal bottomhole pressure of 2.8 MPa. Overall production performance was enhanced by a faster rate of depressurization. Estimated water production rates in all cases were limited and easily manageable. None of the tested well configurations or depressurization strategies significantly reduced water production without also severely reducing gas production. In all the investigated cases, the 95% of the long-term fraction of produced water was replenished by inflows from the boundaries, and could not be reduced. These substantial water inflows are an unavoidable feature of HU-B and cannot be easily mitigated by means of hydraulic control.

1. INTRODUCTION

1.1. Background information

Methane gas hydrate reservoirs occur beneath terrestrial permafrost and along the marine continental slope, containing quantities of natural gas significant to the global energy economy.[1] The solid hydrate phase must depressurized and dissociated to create free natural gas that can subsequently be produced by conventional means. Ongoing research has identified production methods effective for permafrost reservoirs[2-4] and oceanic reservoirs[5-6], and production testing has shown that such production is feasible on timescales of days to weeks. After decades of preliminary research, it is now time for long-term tests to establish the commercial viability of the hydrate-reservoir production process.

Such tests have increased in length and sophistication over the past two decades, in tandem with our understanding of the methods required to exploit hydrate reservoirs effectively. The Mallik field tests in 2002 and 2007 were limited to only 5 days[7,8], followed by the 37-day Ignik Sikumi tests of 2012[2], the 42-day Nankai Trough offshore tests in 2017[6], and the 60-day Shenhu test in 2017[10]. These tests are described in detail in the review by Yamamoto et al.[9], which argues that the next step in the evolution of hydrate production technologies requires long-term production testing on commercial timescales. Commercial operations will be forced to manage a number of challenges and uncertainties, including the geomechanical response of the reservoir to production, the effect of reservoir boundaries (open vs. closed), and permeability management. All of these issues have been studied extensively via numerical simulation[11-15], but have never been tested at-scale in the field.

A long-term field test of production from a suitable permafrost-associated hydrate reservoir on the Alaska North Slope began with the recent drilling of the Hydrate-01 Stratigraphic Test Well within the Prudhoe Bay Unit.[16] A multi-national research effort has been in progress for a number of years to prepare for the test, to anticipate the engineering challenges expected, and to design the test[17-22].

This study is part of that larger planning effort, and consists of a numerical simulation investigation that will inform the design parameters of the proposed production test. A previous paper[23], focused on the development of a detailed numerical model of the proposed test, and described the impact of temporary interruptions (shut-ins) on the expected production performance controlled depressurization over different time scales. The previous study also highlighted the importance and effectiveness of multi-step depressurization strategies, raised important concerns about the quantity of produced water, and validated the proposed monitoring strategy for the test. The current paper is a continuation of the numerical investigations in support of the planned long-term test of production from the hydrate-bearing B1 Sand of the stratigraphic Unit B—at the site of the Hydrate-01 Stratigraphic Test Well within the Prudhoe Bay Unit[16]—by means of controlled depressurization operations. Here the focus of the investigation is the analysis of water and gas (with emphasis on water) production under a variety of conditions and production scenarios, and its impact on the design and management of the field test.

1.2. Objectives

The main objectives of this phase of the scoping studies are the following:

- To obtain estimates of the maximum and minimum expected rates of water production in the course of the depressurization-induced gas production from the hydrate accumulation at the site of the field test. This is to be accomplished by using permeability estimates (sets A and B) from two different interpretations of flow and geophysical data[22] that yielded larger and more conservative estimates of the flow properties, respectively, of the various geologic units at the site. The expectation is that the actual rate will be within this bracketed range of rates. In essence, this component of the study addresses the effect of flow properties on production.
- Using a set of flow properties[22] (Set C) that is considered a more realistic interpretation of the data, to estimate the fluid production rates associated with the position of the well relative to the hydrate-bearing layer in the B1 Sand and the length of the production interval.
- After determining the well location and production interval that yields optimal results, to further refine and improve the design of the field test by evaluating alternative production scenarios associated with management of the time-variable bottomhole pressure at the well.

Note that the effort does not aim to simply develop operation management strategies to minimize in absolute terms the large water production seen in the earlier simulation study[23], but to determine the test design that best serves the totality of objectives and expectations of this test. This being a gas production test, minimization of water production is not an acceptable goal if this is associated with minimal gas production. We seek the combination of well design and operation parameters and practices that can yield a relatively modest and easily managed water production rate (not necessarily the minimum) that is associated with the highest gas production rate and the strongest system response during the field test. Thus, an additional objective of this study is to glean all possible additional information from the various cases that can be used to guide the decisions about production strategies and the associated operational parameters, and to improve the overall design not only of the long-term test, but also of possible future full-production of commercial-scale operations.

2. NUMERICAL SIMULATION AND PROBLEM DESCRIPTION

2.1. The hydrate simulator

In this study, as in the previous work[23], we used the pTOUGH+HYDRATE V1.5 code[24-27] (hereafter referred to as pT+H), a parallel implementation of the serial TOUGH+HYDRATE V1.5 code.[28,29] The pT+H code incorporates the most recent advances in numerical solvers, physics, thermodynamics, and hydrate science.[30] pT+H V1.5 is a fully implicit, fully compositional simulator that describes CH_4-hydrate behavior in geological media, and as such is suitable for modeling all system behavior in hydrate-bearing geologic media from the laboratory to the field scales [31-35]. In its current state, it accounts for all known flow, thermal, physical-chemical, and thermodynamic processes involved in the formation/dissociation of CH_4-hydrates, which can be described by either an equilibrium or a kinetic reaction. It can describe all methods of hydrate dissociation: depressurization, thermal stimulation, inhibitor effects, and combinations thereof. It solves the coupled equations of heat and mass balance for all components involved in a hydrate-bearing geologic system, *i.e.*, H_2O, CH_4, inhibitor(s) and, in the case of a kinetic

reaction, CH4·N_H H_2O (hydrate). These mass components are distributed among four possible phases (gas, aqueous, ice, and hydrate) in 14 out of the 15 possible states of phase existence and co-existence – the only excluded state is that of 100% CH4-hydrate, which is practically impossible in geologic media. Parallelization in pT+H V1.5 is implemented using (a) OpenMPI multi-threading, (b) the METIS[36,37] domain decomposition package, and (c) the most recent version of PETSc[38], a fast, scalable, customizable toolkit for linear algebra in parallel scientific computing.

Because preliminary scoping calculations for the previous numerical study[23] on the same system—conducted using pT+H fully coupled with the RGMS geomechanical simulator[24,26,27]—did not indicate significant deformations even in the vicinity of the production wells during the duration of the production test, the simulations in this study did not involve coupling with a full geomechanical simulator. However, changes in the porosity ϕ and intrinsic permeability k caused by changes in pressure P and in the hydrate saturation S_H—the result of hydrate dissociation or formation that can significantly affect the mechanical strength and the geomechanical behavior of the system—were described using the simplified geomechanical model based on the S_H-dependent pore compressibility model[28,29] available in pT+H.

2.2. Geology, geometry and configuration

A detailed description of the geology, stratigraphy, geometry, and the various units at the site is provided by Boswell et al.[16] and Tamaki et al.[19], was also discussed in our earlier study[23], and will not be repeated here. **Figure 1** provides a simplified description of the simulated system, including its relationship to the geology, minerology and stratigraphy at the site and the dimensions of its various geologic units. The testing configuration involves a single vertical production well, with two observation wells located at a distance of r = 30 m and 50 m from the production well. Note that one of the evaluation criteria of the various production schemes in this and the previous studies is the response of the system at the two observation wells.

The cylindrical domain used in this and in the previous study[23] is standard in single vertical well studies, and is chosen for this study also due to the lack of information on the spatial distribution of heterogeneities in key properties (k, ϕ) and conditions (S_H) in the subsurface profile. The computational efficiency of this 2D cylindrical domain—compared to that associated with a 3D domain necessitated by heterogeneity—was also a bonus. The vertical dimension of the system and the thicknesses of the overburden and underburden followed faithfully the geology and stratigraphy of the system and were selected based on our previous experience with simulating systems of this size and scope[29-33]. Continuous monitoring at the top and bottom boundaries of the system indicated that these were true boundaries, characterized by constant pressures and temperatures, thus validating the domain definition. The radial dimension was determined by preliminary computations that indicated negligible fluid and heat exchange at a radius of r = 800 m from well within a year of production.

The simulated domain includes the hydrate-bearing B1 Sand layer of Unit B (hereafter referred to as the HU-B layer), the additional hydrate-bearing C1 Sand and D1 Sand layers of Units C and D (hereafter referred to as the HU-C and HU-D layers, respectively), the hydrate-free, water-saturated interlayers BC and CD, and the underburden (see **Figure 1**). Of those, HU-B is of paramount importance because it is the target of the gas production test from its hydrate deposit.

2.3. System properties and well description

The hydraulic properties of the layers in the various strata and units of the domain, and their spatial variability with depth, were obtained from logging-while-drilling (LWD) data acquired at the Hydrate-01 STW[39] and pressurized side-wall core samples[17,19]. These sources of data were used to develop different estimates (A, B, and C) of the spatial distributions of the intrinsic and of the effective permeability in the profile of the subsurface. Thus, the B-estimates were based on the interpretation of nuclear magnetic resonance (NMR) data[39] and the use of the Timur-Coates equation, yielding the lower intrinsic and effective permeabilities (k_L and k_{eL}, respectively) shown in **Figures 2(a)** and **3(a)**.

The A-estimates were based on recalibration of these data to match core-derived k (an approach that implies a permeability shift throughout the system) and involved the Kozeny-Karman equation[40] to yield the higher intrinsic and effective permeabilities (k_H and k_{eH}, respectively) shown in Figures 2 and 3. The C-estimates (**Figure 2** and **4**) are a combination of A and B and are considered more representative of the hydraulic properties of the system[22]. The C-interpretation is of particular significance in HU-B (the production target, and the unit which **Figure 4** describes), in which it applies the core-based values only to the upper part of the unit, the log-based k estimates to the non-reservoir part of the system below HU-B and uses a transition (gradual shift) between the two in the lower part of the reservoir. The interested reader is directed to an earlier publication[22] for a more detailed discussion on the subject.

The ϕ and S_H estimates in **Figure 2** are the same in all three interpretations, as are those of the irreducible aqueous saturation S_{irA} (**Figures 3** and **4**). The variations of these key data (k, k_e, S_{irA} and S_H data) with the elevation z were used to determine the corresponding relative permeabilities of the aqueous and of the gas phase (k_{rA} and k_{rG}, respectively) in the subsurface at the site according to the models

$$k_{rA}=\frac{k_e}{k}=\left(S_A^{¿}\right)^n \text{ and } k_{rG}=\left(S_G^{¿}\right)^m, \text{ where } S_A^{¿}=\frac{S_A-S_{irA}}{1-S_{irA}}, S_G^{¿}=\frac{S_G-S_{irG}}{1-S_{irA}},$$

$S_A = 1–S_H–S_G$, with S_G and S_{irG} representing the gas saturation and the irreducible gas saturation, respectively. In essence, the relative permeability behavior is determined from the estimation of the exponent n corresponding to each one of the A, B and C interpretations of the data. Analysis of (a) the lower k_L and k_{eL} estimates (corresponding to interpretation B) and (b) of the higher k_H and k_{eH} estimates (corresponding to interpretation A) provided the $n_{max}(z)$ and $n_{min}(z)$, respectively, in the entire domain. **Figure 3(c)** shows the variations with depth of $n_{max}(z)$ and $n_{min}(z)$ within the all-important HU-B. The variation of the exponent n in the more representative C-interpretation ais shown in **Fig. 4**.

The field data informed the simulation parameters for all simulations performed in this and the earlier design studies[22,23]. Given the significant heterogeneity evidenced in Figures 2 to 4, to represent the variability of the properties with, and to map those properties over the high-resolution vertical discretization of the simulation domain (which did not coincide with sampling frequency of the data), the system properties in each layer were averaged from the corresponding (A, B, or C) dataset[23] according to the following equation:

$$\acute{X}_{\Delta z} = \frac{\int_{z_1}^{z_2} X\, dz}{\Delta z}, \Delta z = z_2 - z_1$$

where $\acute{X}_{\Delta z}$ is the average value of the property X within the Δz subdivision between the z_1 and z_2 elevations, and is obtained from the numerical integration of all the raw data of X vs. z. This approach maintains maximum fidelity to the field data.

The integrals of the heterogeneous vertical distributions of $n_{min}(z)$ and $n_{max}(z)$ – corresponding to interpretations A and B, respectively – in the HU-B are shown in **Figure 5**. Similarly, the integrals of the heterogeneous vertical distributions of $\ln(k)$, ϕ, S_H, and S_{irA} corresponding to interpretation C are shown in **Figure 6**. The same approach was used consistently for the estimation of all the flow properties from the three data interpretations in all the subdomains of the simulated system (Figure 1). Note that, in the absence of any initial free gas in the system, there we no data that could be used for the estimation of k_{rG}. This being the case, the exponent m that describes the relative permeability of the gas phase was estimated from the equation

$$m = n - 0.5\ \text{Max}\{0.0,\ n\text{-}2\}$$

that had been used in the earlier study[23], which was based on analogs from porous media with similar flow characteristics[22,23] and which prevents unrealistically high k_{rG} estimates. To address the possibility of a gas phase appearing in the BC and CD interlayers and/or in the underburden in the course of production, the m and n values for these media were approximated using data and parameters from earlier studies of systems featuring similar reservoir properties[32,33,41,42]. A similar approach was used for providing capillary pressure P_{cap} estimates for all formations; beginning with the base-case P_{cap} data corresponding to interpretation C (see **Table 1**), P_{cap} was adjusted for the effects of varying k and ϕ in the various formations of the different interpretations according to the Leverett J-function[43].

The relative permeability and the capillary pressure functions, and the thermal properties of the various geological media are listed in **Table 1**. Parameter values for the van Genuchten equation[44] for fully water-saturated media were obtained from appropriate analogs in earlier studies[33,42] Thermal conductivity values are consistent with those of media with the same type and texture, and reasonable specific heat values were assumed for all the geologic media[33,42] in lieu of field data.

We approximated wellbore flow with Darcian flow using the established approach[33] of a pseudo-porous medium with porosity $\phi = 1$, a very high $k = 5\text{x}10^{-9}$ m^2 (= 5,000 Darcies), a capillary pressure $P_c = 0$, a relative permeability that is a linear function of the phase saturations in the wellbore, and a low (but nonzero) irreducible gas saturation $S_{irG} = 0.001$ (necessary to allow the emergence of a free gas phase in the well). This approach was selected because earlier scoping calculations using the more appropriate physics of fluid flow in wells according to the Drift Flux Model model[45] did not show significant deviations from the pseudo-porous medium approximation but was significantly more computationally intensive.

2.4. Domain discretization

The significant vertical heterogeneity in the domain required the use of the same very fine discretization in z used in the earlier study[23]. The very steep thermal and pressure gradients associated with the strong endothermic reaction of hydrate dissociation also demands the use of

very fine grids, and this is particularly important in the vicinity of the well where these gradients are the steepest.[46] We used (a) a uniform discretization of Δz = 0.1 m in the HU-B layer, (b) a uniform discretization of Δz = 0.25 m in the hydrate-bearing HU-C layer, (c) a uniform discretization of Δz = 0.51 m in the HU-D layer (not in communication with the HU-B layer), and (d) variable Δz ranging from 0.1 m to 5.0 m in the water-filled interlayers and in the underburden. The variability in Δz with depth is fully described in **Figure 7**.

Very fine radial discretization was also used in the vicinity of the well, beginning with a well radius of 0.05 m, followed by Δr increments ranging from 0.1 and 0.3 for r < 100 m, and then logarithmically increasing to 6.2 m at the final $r = R$ = 800 m.[23] The domain discretization included (a) top and bottom boundaries held at constant P and T conditions, each with a Δz = 0.01 m, and (b) a Δr = 0.01 m constant-P and T boundary at r = 800 m.[23] Continuous monitoring of flows through the cylindrical interface at $r = R$ indicated imperceptible fluid flows during the duration of the simulations, confirming its function as a true, time-invariant boundary.

The discretization of the simulated domain was sufficiently fine to cover even the most demanding of the various production schemes, allowing the use of the same grid without modifications for all of the simulated cases. The cylindrical domain was discretized into 641 x 343 = 219,0863 gridblocks in (r,z) using the MeshMaker package.[47,48] Treating hydrate dissociation as an equilibrium reaction[49] and accounting for the effect of the salinity[17-19] (which was low, but not negligible) on hydrate dissociation resulted in a system of ~880K equations, which, as in the previous study,[23] exceeded the capabilities of any serial computation and necessitated the use of the pT+H MPI-based parallel simulator for efficient solution within a reasonable time frame (see Section 2.1).

2.5. Initial and boundary conditions

Initialization involved simulations over an extremely long time, i.e., until flow, thermal, thermodynamic and chemical equilibrium is attained and the system remains time-invariant in the absence of disturbances caused by the presence of wells or by different boundary conditions. The creation of initial conditions followed the well-established methods described by Moridis et al.[15,46,50] and these studies used the same initial conditions as in the previous study.[23] The initial P- and T-distributions within in the domain reflect hydrostatic conditions and the geothermal gradient at that site.

As already indicated, the top and bottom layers of the grid represented boundaries that were permeable and were kept at constant P and T conditions, as was the outermost radial increment that defined the lateral boundary of the system. These boundaries defined an *open* system that allowed fluid and heat exchanges with its surroundings and were located at distances that had been proven to be sufficient far from the well to ensure that P and T-changes caused by hydrate dissociation and gas production would not reach them during the simulation period.

The uppermost gridblock of the well was treated as an internal boundary condition, describing fluid production in response to a time-variable bottomhole pressure P_w. The final P_w = 2.8 MPa used during production is selected to be sufficiently high to prevent the formation of ice and its adverse effect on effective permeability.

2.6. Production scenarios and simulated cases

In all the simulated cases, the CH_4 production from the HU-B layer in the Hydrate-01 STW is based on depressurization-induced dissociation of hydrates. Our studies included the following cases:

- *Cases H and L*: These studies were conducted using the properties and conditions estimated from the A- and B-interpretations of the field data. Thus, Case H involved the highest k_H and k_{eH} estimates and the lowest n_{min}; Case L involved the lowest k_L and k_{eL} estimates and the highest n_{max} (see Section 2.3, **Figures 2, 3 and 5**). The production interval of the wells in Cases H and L are W_L = 10 m long and their tops coincide with the top of HU-B. The results of these two cases are expected to bracket the expected fluid production estimates, and also provide criteria about the permeability-related limits of applicability of the depressurization-based production from hydrate deposits. It is expected that Case H will provide estimates of the upper limit of the water production rate and a clear indication if such production can overwhelm the facilities available for the test. The depressurization regime (similar to the previous study[23]) in these cases is shown in **Figure 8** and involves a step-wise decrease in P_w at 30-day intervals: beginning with an initial P_w = 6.6 MPa at the onset of production (t = 0), P_w is lowered to P_w = 4.6 MPa at t = 30 days and to P_w = 2.8 MPa at t = 60 days, beyond which time it remains constant until the end of the simulation.
- *Cases wX (X = 05, 10, 15) and R*: These studies (and all subsequent ones) were conducted using the properties and conditions estimated from the more realistic C-interpretation of the field data, yielding the properties and conditions depicted in **Figures 4 and 6**. The focus of this study is the evaluation of the effect of the location and of the length of the completed production interval W_L of the well on fluid production and the overall system response. In Cases w05, w10 and w15, W_L = 5, 10 and 15 m, respectively, with the top of the well coinciding with the top of the HU-B layer. In Case R (the reference case, selected as such because, as will be seen, is the most promising), the length of the well is 10 m, but its top is located 3 m below the top of the HU-B layer, i.e., deeper within the hydrate body and below the elevations where the highest S_H levels occur. In all these studies, the depressurization regime is as in Cases L and H (see Figure 8).
- *Cases R, L2m, L6m and D15*: The simulations in these cases (a) are based on the properties from the C-interpretations of the field data (**Figures 4 and 6**) and (b) involve wells that are as in Case R (included for reference), i.e., with W_L = 10 m and with their tops 3 m below the top of HU-B. The reason for these cases is to evaluate the effect of different production management regimes on fluid production and system response, as defined by different modes of P_w lowering. Thus, in Cases L2m and L6m, P_w is lowered linearly and continuously from $P_w = P_0$ at t = 0 to P_w = 2.8 MPa at t = 60 days (2 months) and t = 180 days (6 months), respectively. In Case D15, the depressurization regime involves a step-wise decrease in P_w at 15-day intervals: beginning with an initial P_w = 6.6 MPa at t = 0, P_w is lowered to P_w = 4.6 MPa at t = 15 days and to P_w = 2.8 MPa at t = 30 days. The different depressurization regimes are shown in Figure 8.

In all cases, after P_w reached 2.8 MPa, it remained constant until the end of the simulation. Although the original design of the field test called for a 6-month duration of production, the

simulations went well beyond that time (and often exceeded 360 days) in an effort to get a deeper understanding of the longer-term behavior and response of the system under production.

2.7. Simulation process, outputs, and evaluation method

In the course of the simulation, the following flow-related conditions and parameters were monitored: the spatial distributions of P, T, and gas and hydrate phase saturations (S_G and S_H, respectively); the volumetric rates of (i) CH_4 released from dissociation Q_{mR}, (ii) CH_4 well production in the gaseous phase, in the aqueous phase and the total CH_4 production (Q_{mG}, Q_{mA} and Q_{mT}, respectively); (iii) the cumulative volumes of CH_4 released from dissociation, produced at the well in the gas phase and in the aqueous phase, and remaining in the deposit as free gas (V_R, V_{mG}, V_{mA}, V_{mT} and V_F, respectively); (iv) the water mass production rate at the well (Q_{wW}) and the cumulative mass of produced water (M_{wW}); (v) the water inflow rates from the top and bottom boundaries (Q_{wT} and Q_{wB}, respectively), and the total water inflows $Q_{wTB} = Q_{wT} + Q_{wB}$; (vi) the cumulative mass of water inflows from the top and bottom boundaries (M_{wT} and M_{wB}, respectively), and the total mass of water inflows $M_{wTB} = M_{wT} + M_{wB}$; (vii) the water replenishment ratio $R_{wR} = Q_{wTB} / Q_{wW}$ that describes the fraction of the withdrawn amount of water that is replaced by water inflows from the boundaries; (viii) the aqueous CH_4 production fraction $R_{mAT} = Q_{mA} / Q_{mT}$ that describes the fraction of the total gas production originating from dissolved CH_4; and (ix) the instantaneous and cumulative water-to-gas ratio ($R_{Qwm} = Q_{wW}/Q_{gT}$ and $R_{Mwm} = M_{wW}/V_{mT}$, respectively).

We evaluated the production potential of the hydrate deposit in HU-B—the only dissociating accumulations in the subsurface; HU-C and HU-D (included in the simulation domain) were unaffected for the duration of the simulation—by using two *production* criteria[11,51]: an absolute criterion and a relative criterion. Because water production is the main focus of the study, the absolute criterion is reversed from what we have used in other production studies[51] and is now satisfied by a low water production potential (i.e., low Q_{wW}, M_{wW}, R_{wR}, R_{mAT}, R_{Qwm}, and R_{Mwm} values) over the duration of the study. High water production is undesirable not only because it may indicate significant water inflows from the boundaries and inefficient depressurization, and is inevitably associated with higher production costs associated with water lift and disposal. As already indicated, minimization of water production is not a necessary and sufficient criterion because it defeats the purpose of a gas production test if it is not accompanied by as high as possible (or, at least, reasonable) gas production. This is addressed by the relative criterion, which is satisfied when, for a given water production, (a) Q_{mG}, Q_{mT}, V_{mG}, V_{mT} , and V_F are maximized and (b) Q_{mA}, V_{mA}, R_{mAT}, R_{Qwm}, and R_{Mwm} are minimized.

It is important to indicate that the results of this and all related studies are applicable only to the planned long-term test, and cannot be extrapolated or transferred to a full operation of gas production from the deposit. This is because the localized no-flow boundaries at the confluence of the individual well subdomains—in a system of multiple interacting wells associated with full production operations—are expected to effect a substantially stronger depressurization (and, consequently, a larger gas production) than what can be attained with the open (infinite-acting) boundaries of the single-well system investigated here.

3. RESULTS AND DISCUSSION – CASES H AND L

3.1. Water production

Figure 9(a) shows the evolution over time of the mass flow rates of water (a) produced at the well Q_{wW} and (b) inflows from the top and bottom boundaries of the HU-B layer, Q_{wT} and Q_{wB}, as well as the cumulative water inflow $Q_{wTB} = Q_{wT} + Q_{wB}$. As it has already been indicated, the simulation results in this and all the cases investigated in this study indicated zero or negligible fluid and/or heat exchanges between (a) the interior of the entire domain and its top horizontal, bottom horizontal and outer radial boundary at r = 800 m and (b) between the hydrate-bearing HU-C and HU-D layers and their adjacent units/boundaries.

The well production rate Q_{wW} includes contribution of (a) formation water that initially coexists with hydrate in the undisturbed HU-B, i.e., corresponding to an initial aqueous phase saturation $S_A = 1\text{-}S_H$, (b) water released from hydrate dissociation, and (c) water inflows from the boundaries. Q_{wW} exceeding Q_{wTB} (especially if this lasts over long periods) is highly desirable because it is an indication of effective depressurization and, consequently, of more intense hydrate dissociation and CH_4 release.

These figures reveal the following:

- In both Cases H and L, Q_{wW} and Q_{wTB} (a) respond almost instantaneously to the P_w drops of the three-step depressurization regimes that are identified by spikes in Q_{wW} and Q_{wTB}, (b) register a significant step increase at the beginning of each depressurization step, (c) increase rapidly with time within each depressurization period (after the initial spikes), and (d) increase consistently with time for the entire duration of production. The long-term behavior of Q_{wW} after the minimum P_w = 2.8 MPa (see **Figure 8**) is reached exhibits a mild and practically linear increase.

- In both Cases H and L, water inflows from the boundaries are significant and influx from the top boundary Q_{wT} consistently exceeds that from the bottom boundary Q_{wB}. The $Q_{wT} > Q_{wB}$ relationship is caused by the application of the constant bottomhole pressure at the top of the production well at a location immediately below the top boundary of the HU-B layer. The higher overburden permeability and the rather uniform k_{eH} in the profile of **Figure 3(a)** in Case H enhance Q_{wT}; the very low k_{eL} in **Figure 3(a)** at the top of the HU-B layer in Case L, coupled with the long distance from the lower boundary and the universally lower k_L and k_{eL} in the entire profile, results in the larger contribution of flow from the upper boundary.

- As expected, Q_{wW} in Case H is consistently and significantly larger than that in Case L because of the substantially larger k_H and k_{eH} in the HU-B layer (**Figure 3(a)**).

- Because of the continuously increasing Q_{wW}, their long term values in Cases H and L (the highest and lowest permeability cases) are expected to define the upper and lower limits of the expected water production at the site. Thus, it appears that Q_{wW} is expected to fall within the range between 8.0 $\times 10^5$ kg/day (about 5,000 BBL/day) and 2.7 $\times 10^5$ kg/day (about 1700 BBL/day) during a field test that is to last $\leq$ 300 days (given the long-term linear behavior of Q_{wW}, extrapolation is possible). Note that a Q_{wW} in excess of 5,000 BBL/d may overwhelm the available water-handling capabilities at the site.

- In a worrying sign, Q_{wTB} represents a large and increasing fraction of Q_{wW} in both Cases H and L, indicating easy replenishment of withdrawn water by water inflows from the boundaries. Actually, a review of **Figure 9(a)** clearly indicates parity of Q_{wW} and Q_{wTB} in

both cases for t > 150 days, which is a clear sign of weakening depressurization and, consequently, dissociation. This is confirmed by the evolution of the replacement ratio $R_{wR} = Q_{wTB}/Q_{wW}$ in **Figure 9(b)**, which is even more revealing because it shows not only long-term equality of Q_{wTB} and Q_{wW} (R_{wR} = 1) but also water inflows exceeding Q_{wW} on multiple occasions. Thus, in the low permeability Case L, R_{wR} > 1 immediately after each P_w drop in the depressurization regime, and even reaches very high levels (almost 1.24 at its peak) that last for a long time (until about t =145 days) immediately after the final P_w = 2.8 MPa is reached. This is also evident in the Q_{wB} (and the consequent Q_{wTB}) curve at the same time in **Figure 9(a)**, indicating that these significant water inflows emanate from the more permeable lower boundary. The reason for this behavior is not clear from the available information, but the most likely explanation is that flow through one or more relatively thin hydrate layers toward the HU-B base—which initially restricted flow and enhanced dissociation by virtue of their low effective permeability and the already intense depressurization resulting from the low k_L and k_{eL}—increased when P_w decreased and the associated S_H decreased significantly. The combination of the resulting higher effective permeability and the large pressure gradient (caused by the low pressure above it) is probably the reason for the higher Q_{wB} that is denoted by the inflow bursts in **Figure 9(b)**.

- The large Q_{wW} and Q_{wTB} in Case H make a hydrate accumulation with these characteristics an undesirable CH_4 site for a production test and, probably, a questionable full production target because the water inflows from the top and bottom boundaries cannot be controlled or mitigated hydraulically by the operation of other vertical wells.

3.2. Gas release, production and accumulation

Figures 10(a) shows the rates of (a) CH_4 release from the dissociation of the hydrate Q_{mR}, (b) CH_4 production in the gas phase Q_{mG}, (c) CH_4 production in the aqueous phase Q_{mA}, as well as (d) total CH_4 production $Q_{mT} = Q_{mG} + Q_{mA}$ in Cases H and L. Note that all these quantities represent cumulative rates that describes the behavior of the entire HU-B system.

The effect of the sharp P_w drops at the two depressurization steps at t = 30 days and t = 60 days in both cases (see **Figure 8**) is obvious in the initial "spikes" in Q_{mR} (and to a lesser extent in the other rates), indicating rapid gas release and enhanced production in the immediate aftermath of the sudden P_w drop. These spikes in all the rates of **Figure 10(a)** reach very high levels, but last for a very short time and are followed by rates always higher than the ones in the previous interval that corresponds to a higher P_w. Review of **Figure 10(a)** reveals the following:

- For t < 30 days (i.e., before the 2nd depressurization step) $Q_{mA} > Q_{mG}$ in the both Cases H and L, indicating that the source of most of the produced CH_4 is exsolution from the produced water. The obvious conclusion is that the degree of depressurization during the 1st step is weak and insufficient to effect significant hydrate dissociation. The result of the very limited gas releases during this initial depressurization step is that $Q_{mT} > Q_{mR}$ for about 20 days in both cases, and this is only barely reversed afterwards (to t = 30 days).
- For 30 days $\leq t \leq$ 60 days, Q_{mR} and Q_{mT} increase (slowly in Case H) after the initial spikes, $Q_{mG} > Q_{mA}$ and Q_{mR} generally exceeds Q_{mT} in both cases, indicating the enhanced effectiveness of depressurization at the lower P_w level. The stronger the dominance of Q_{mG} over Q_{mA} and of Q_{mR} over Q_{mT}, the more desirable a hydrate accumulation is as a

production target because it is associated with a larger contribution of the gas phase in the production stream. In other words, a criterion for the desirability of a hydrate deposit can be the proximity of Q_{mG} and Q_{mT}, provided that they are at a satisfactory level. Because of the very low solubility of CH_4 in water, a large Q_{mA} relative to Q_{mG} is evidence of CH_4 exsolution being the source of the gas, and the need for a large (and highly undesirable) water production for a reasonable level of gas production. Under such conditions, almost inevitably Q_{mT} is close to (and often exceeds) Q_{mR}, which is a serious deterrent to attempts at gas production from hydrates. In Case L, Q_{mG} appears to be almost an order of magnitude larger than Q_{mA}, and Q_{mG} is the dominant contributor to Q_{mT} and $Q_{mR} > Q_{mT}$, indicating accumulation of free gas in the reservoir. The situation is less desirable in Case H because of the larger contribution of Q_{mA} to Q_{mT} and the practical coincidence of $Q_{mR}>Q_{mT}$, indicating minimal free gas accumulation in HU-B (an unwelcome development). These deductions are confirmed by the evolution of V_F in **Figure 10(b)**, which shows rapid CH_4 accumulation in the gas phase in Case L and minimal one in Case H during this depressurization step. Note that V_F is negligible in both cases during the initial depressurization step for the reasons already discussed.

- For $t > 60$ days (i.e., after the third depressurization step to the final $P_w = 2.8$ MPa), the relative behaviors of the Q_{mG}, Q_{mA}, Q_{mT}, and Q_{mR} patterns that were established in the previous depressurization period continue with the same general changes: the Q_{mA} contributions to Q_{mT} increase, indicating an increasing water production (in agreement with the observations in **Figure 9**) and for a long time $Q_{mR} > Q_{mT}$, but there is a tendency toward their long-term convergence. The latter signifies either stagnation or decline in the level of V_F because Q_{mR} cannot do more than simply replace the produced Q_{mT}, and is confirmed by the patterns of evolution of V_F during the last depressurization period (**Figure 10(b)**). A typical general characteristic of this depressurization step is (a) the continuous decline of Q_{mG}, Q_{mT}, and Q_{mR} and (b) the continuous (slight in Case H) increase in Q_{mA} in both cases. The latter is consistent with the observations in **Figure 9**. Of particular interest is the evolution of Q_{mR} and Q_{mG} in Case L: there is a sudden drop in both at about $t = 120$ days, i.e., at a time of a sudden increase in Q_{wB} that was attributed to the enhanced permeability and higher water inflows from the base of HU-B (see **Figure 9** and Section 3.1), and which corresponds to an inflection point in the corresponding V_F curve of **Figure 10(b)**. Past this point, both Q_{mR} and Q_{mG} decrease rapidly to about t =145 days, when V_F is at its maximum in **Figure 10(b)**) and a new/stable flow regime is established, during which practically all the produced water is replaced by boundary water inflows. For $t > 145$ days, Q_{mR} is initially larger than Q_{mG}, but this difference decreases until the rates coincide at about $t = 220$ days. This convergence indicates depletion of the free CH_4 in the reservoir, and is confirmed by the V_F for Case L at that time. In Case L, the slightly increasing Q_{mA} and the slightly decreasing Q_{mG} are the reason for the slight (and continuous) decrease in V_F during this depressurization step.

- Q_{mR} and Q_{mT} in Case H are consistently and significantly larger than those in Case L—$Q_{mT} \approx 3{,}080$ m^3/day $\approx 109{,}000$ ft^3/day at $t = 250$ days in Case H, i.e. more than double of $Q_{mT} \approx 1{,}400 \approx 50{,}000$ ft^3/day at $t = 300$ days in Case L—because of the substantially larger k_H and k_{eH} in the HU-B layer—but this does not render a hydrate deposit with the

characteristics of Case H more desirable because (a) these rates are relatively modest, (b) the water production is large and potentially excessive (see Section 3.1 and **Figure 9**) and (c) the free gas accumulation V_F is limited (**Figure 10(b)**).

- The relatively low (and converging) Q_{mR} and Q_{mT} in Case H, coupled with the low and declining V_F, make a hydrate accumulation with these characteristics an undesirable site for a production test and a challenging full production target because of limited production potential due to the low permeability of the formation. However, it is possible that this limitation can be addressed by a tighter well spacing. Note that the low V_F associated with case H is a further indication of its unsuitability for production testing and/or full production operations.

3.3. Water-related parameters

Directly related to the relative magnitudes of Q_{mA} and Q_{mG}, and to the contribution of Q_{mA} to Q_{mT}, is the aqueous production fraction $R_{mAT} = Q_{mA}/Q_{mT}$ that is shown in **Figure 11(a)**. The results confirm earlier observations about the large contribution of exsolved CH_4 to the overall gas production Q_{mT}. Thus, R_{mAT} is at a maximum during the first depressurization step, during which is reaches about $R_{mAT} = 0.78$ and 0.72 in Cases H and L, respectively, in line with the Q_{mA} vs. Q_{mG} comparison and observations in Section 3.2 and **Figure 10(a)**. The more effective depressurization and hydrate dissociation/ gas release in the less permeable Case L during the second depressurization step is reflected in the lower averaged $R_{mAT} \approx 0.10$; during the same time, $R_{mAT} \approx 0.36$ in the more permeable Case H. During the 3rd and final depressurization step, R_{mAT} begins at about 0.18 at $t = 30$ days and then increases continuously and almost linearly for $t > 120$ days, reaching an unacceptable $R_{mAT} \approx 0.30$ at $t = 250$ days, with a continuing upward trend past that time. During the same period, R_{mAT} begins very low at about 0.03 at $t = 60$ days but is marred with a sudden jump to a $R_{mAT} \approx 0.20$ at t = 150 days—i.e., at the time when Q_{mR} and Q_{mG} experience a quantum decrease (**Figure 10(b)**) and practically all the produced water is replaced by boundary inflows—and a (slight) upward trend afterwards. The high (and rising) R_{mAT} level is an indication of the undesirability of a hydrate deposit with the characteristics of Cases H or L for a production test (and possibly as production targets). This negative impression is enhanced by the upward long-term trend in R_{mAT}, which is strong (and possibly clear) evidence of water inflows from the boundaries.

As indicated earlier (and as has been pointed out by Moridis et al.[11,51]), production from hydrates from any given accumulation is evaluated using two criteria: (a) the absolute criterion, involving either (i) maximization of Q_{mT} and of the overall CH_4 production potential for a given water production, or (ii) minimization of Q_{wW} and Q_{wTB} for a given gas production, depending on where the focus of the study is, and (b) the relative criterion, describing the instantaneous or cumulative water-to-gas ratios (R_{Qwm} or R_{Mwm}, respectively) that describe the amount of (unwanted) water associated with the CH_4 production. Obviously, after satisfying the absolute criterion, a promising production target is associated with the minimization of the relative criterion. Earlier studies[52] have indicated that the long-term values of R_{Qwm} or R_{Mwm} trend asymptotically toward 4 when the produced system is bounded by impermeable boundaries.

Figure 11(b) shows the evolution of R_{Qwm} and R_{Mwm} of the relative criterion in Cases H and L. They both decline initially from very high levels (>400) to ≈ 290 and ≈ 260 kg of H_2O per ST m^3 of CH_4 in Cases H and L, respectively, at the end of the first depressurization step, when

water is the only produced fluid and the only source of CH_4 from exsolution (**Figure 10(a)**). R_{Qwm} also declines at the beginning of every subsequent depressurization step, but continuously increases during it. The long-term trend of both R_{Qwm} and R_{Mwm} in both cases is increasing. R_{Qwm} reaches ≈ 200 kg of H_2O per ST m^3 of CH_4 at t = 360 days in Case H, and R_{Qwm} ≈ 260 kg of H_2O per ST m^3 of CH_4 at t = 300 days in Case L. These unsustainably (and possibly prohibitively) high levels constitute failure of the relative criterion: they indicate increasing contribution of water inflows from the boundaries in agreement with earlier observations (Section 3.1, **Figure 9**), and provide additional evidence of the unsuitability of hydrate deposits of the characteristics of Cases H and L as targets for production tests.

3.4. Response at the observation wells

Observation wells are very important because they can provide direct observations and measurements of the system behavior during the production test and evidence (direct and indirect) of hydrate dissociation. Here we investigate the response at the two observation wells at the site of the field test—at distances of r = 30 m and r = 50 m from the production well, referred to as W30 and W50 wells, respectively—in an effort to determine if they are appropriately located to perform their intended function, i.e., to monitor the relevant reservoir properties and their changes during production.

Figure 12 shows the evolution of P, T, and of the pore-volume averaged gas saturation $\acute{S}_G$ in the two observation wells in Cases H and L. As expected, the changes in the P_w regimes at the beginning of each depressurization step are accurately captured by the evolution of P in both wells in Case H (**Figure 12(a)**), as evidenced by the unmistakable inflection points at the known times of change. This is the result of the low compressibility of water and the high permeabilities, which enable the fast travel of the pressure wave in continuous aqueous phases in porous media and the simultaneous registering of P_w-induced P-changes in wells that are 20 m apart, making them suitable pressure observation wells. The larger permeabilities in this case and the associated large water production Q_{wW} are the reason for the continuous long-term mild pressure drop at the wells during the last depressurization step.

The situation is quite different in Case L, in which the lower permeabilities attenuate the P-response at the wells. The inflection points in the response of the W30 well are clear but much more attenuated (smooth) than those in Case H, and practically indiscernible in the P-response of W50 (which renders it ineffective as an observation well). However, the lower permeabilities result in much lower P-observations than those in Case H. The rising P at both wells for t > 120 days is attributed to the water inflows that have been previously indicated by other variables and discussed in Sections 3.1 and 3.3 (see **Figures 9 and 11**). Note that effective pressure monitoring is a necessary, but by no means sufficient attribute of an observation well in the study and analysis of depressurization-induced gas production from hydrate deposits.

Given the endothermic nature of the hydrate dissociation and the associated large enthalpy of dissociation, temperature is known to be a much stronger indicator of hydrate behavior.[23] Thus, hydrate dissociation is expected to be associated with lowering of T (or higher T when hydrate forms). The T-response is expected to be very fast if hydrate dissociates or forms in the immediate vicinity of the well, but the response may be affected by water at different temperatures flowing from other parts of the formation through the well, thus complicating and often confusing the interpretation of the observations.

The *T*-response in **Figure 12(b)** shows the complete failure of both observation wells in Case H, as they show practically no *T*-change and, consequently, no direct evidence of hydrate dissociation at these locations. This is attributed to the large water flows (**Figure 9**) from further away from the production well through the two observation wells that overwhelm any *T*-changes caused by hydrate dissociation in their vicinity. The observation wells fare better in Case L, but still not well: there appears practically no response during the first and the second depressurization steps because the low permeabilities (intrinsic and effective) do not allow dissociation to occur at these locations. The depressurization front appears to reach the location of the W30 wells, and to effect a *T*-reducing response, shortly after the beginning of the 3rd depressurization step, i.e., at t = 64 days; the response in the farther W50 well is further delayed, as the depressurization front and the dissociation-related *T*-drop are registered at about t = 85 days. As in the case of the *P* results in **Figure 12(a)**, the increasing *T* at later times (t > 120 days) in Case L is attributed to the already-discussed water inflows from the more permeable (and warmer) parts of the HU-B and from the boundaries.

In evaluating the effectiveness of horizontal wells, the only possible direct indicator of hydrate dissociation is the observation of free gas, the origin of which is inevitably the hydrate in HU-B—there is no free gas in the entire domain under investigation prior to depressurization (**Figure 1**). The results in **Figure 12(c)** are consistent with the observations in **Figure 12(b)**: they fully confirm the unsuitability of both observation wells in Case H, as they provide indications of minimal free CH_4 presence at very late times (W30 well at t >= 200 days) or they fail completely to register any gas evolution (W50 well). Additionally, they fail to register any free gas until after the beginning of the third depressurization step, and they do so with a delay—at t = 64 days in the W30 well, and at t = 85 days in the W50 well and at generally low levels (lower in W50 than in W30, in agreement with diminished dissociation activity indicated by the higher *T* at the same time). Note the disappearance of the free gas phase in W50 at t = 270 days, which is an indicator of either reduction or cessation of dissociation at this location and dissolution of the released CH_4 in the water flowing toward the well, in agreement with the increasing contribution of Q_{mA} to Q_{mT} (**Figures 10 and 11**).

Thus, the W30 and the W50 observation wells are both inappropriately positioned and neither would be able to fulfill their role by capturing the needed behavior of all the key variables (*P, T* and $\acute{S}_G$) during a gas production test in a HU-B layer having the characteristics of Cases H or L.

3.5. Spatial distributions of key variables

The evolution of the spatial distributions of *P* and *T* in Cases H and L are shown in **Figure 13**, and describe the *P*-response of the system beginning 30 days after the third (and last) step of depressurization. In the presence of a depressurizing (producing) well, higher permeabilities are associated with modest pressure decreases ΔP that affect a larger part of a reservoir; lower permeabilities are associated with a larger ΔP that is concentrated near the well, but which affects a smaller reservoir volume. The observations in **Figure 13** are fully consistent with expectations. The high permeability in Case H is reflected in the mild ΔP that is observed over a larger extent of the reservoir, and the ΔP footprint expands slowly over time. Such a mild ΔP is expected to be associated with limited hydrate dissociation and evolution of gas. The low permeability in Case L is the reason for the significant and localized ΔP that is especially pronounced next to the well, but which is less extended in space. The strong localized ΔP in case

L is expected to be associated with significant hydrate dissociation and a significant accumulation of free gas. Note that the footprint of the declining P in Case L expands over time, but the intensity of the ΔP near the well appears to diminish because of the increase in the effective permeability caused by the hydrate dissociation.

The temperature disturbance in **Figure 13** fully supports the insights and expectations gleaned from the P-distributions. The occurrence of hydrate dissociation is marked by a decline in temperature ΔT caused by the endothermic nature of the reaction. In case H, the footprint of lower temperatures is limited in extent and describes a very mild cooling effect (i.e., a low $\Delta T \leq 2$ ºC) is concentrated near the top of the deposit. The situation is very different in Case L, which shows significant cooling (as large as $\Delta T = 7$ ºC) over a much larger reservoir volume that extends deep into the reservoir thickness. Such significant cooling is evidence of strong dissociation and gas release at this location. In both cases, the intensity of the cooling decreases and the ΔT footprint shrinks continuously over time. These observations are indicative of continuously decreasing dissociation activity, and is in agreement with the continuous decline at these times in the CH_4 release rate Q_{mR} of both cases that is evident in **Figure 10(a)**. Another explanation for the warming trend over time evidenced in **Figure 13** is the arrival in the depicted region of warmer water from distant parts of the reservoir—that are unaffected by the depressurization and do not experience hydrate dissociation and the related cooling—or from hydrate-free boundaries.

The P- and T-distribution-based observations in Case H are borne by the evolution of the S_G distributions in Cases H and L that is depicted in **Figure 14**. Thus, Case H is characterized by very low free gas saturations ($\leq 3\%$ in most of the HU-B) and a footprint of S_G occurrence that initially expands (from $t = 90$ days to $t = 180$ days), and shrinks (albeit slightly) for $t > 180$ days. This is consistent with the time behavior of the limited V_F in Case H that is shown in **Figure 10(b)**. In Case L, the S_G footprint is (a) consistent with the significant cooling of this case that is evident in **Figure 13**, (b) is far less uniform in its distribution and smaller in extent/volume than that of Case H, but (c) involves relatively large saturation levels that locally can reach and exceed 30%, and (d) is consistent with the evolution and magnitude (relative to that of Case H) of the corresponding V_F over the same times (**Figure 10(b)**).

The evolution of the S_H distributions in Cases H and L is depicted in **Figure 14** and provides needed explanations for earlier observations. Thus, comparison of the hydrate-free and the reduced-S_H footprints—and keeping in mind that in the cylindrical domain the relationship of the hydrate mass is not a linear function of r but of r^2—clearly shows significantly more hydrate disappearance in Case H than in Case L, indicating more hydrate dissociation in the former than in the latter. This is consistent with the larger Q_{mR} in Case H that is evident in **Figure 10(a)**, and which is more than double that in Case L. The different pictures painted by the T- and S_G-distributions related to Case H (**Figures 13 and 14**) are not necessarily evidence of limited hydrate dissociation that could create a conflict: the significant warming is attributed to flows of warmer water from (a) the deeper and warmer underburden, from which the majority of the water inflows Q_{wB} originate (see **Figure 9**), as well as from (b) distant parts of the reservoir that are undisturbed by dissociation. Additionally, under the conditions of Case H, it appears that hydrate dissolution into the aqueous phase (as opposed to hydrate dissociation and gas release) plays an important role, due to warm, undersaturated water entering the formation and interacting with the hydrate deposit. This is clearly supported by the large contribution Q_{mA} of

exsolved CH_4 to the total gas production Q_{mT} , and the corresponding R_{mAT} and R_{Qwm} results (See **Figures 10 and 11**).

4. RESULTS AND DISCUSSION – CASES w05, w10, w15 and R

4.1. Water production

As previously discussed (see Section 2.6), the flow properties in these and all subsequent studies were those corresponding the more representative C-interpretation of the field data (see Section 2.3)**. Figure 15a** shows the evolution over time of the mass flow rates of water (a) produced at the well Q_{wW} and (b) the cumulative water inflow from the boundaries $Q_{wTB} = Q_{wT} + Q_{wB}$ in Cases w05, w10, w15 and R

Review of the data in this figure reveals the following:

- Similar to the observations in Cases H and L, in all the cases investigated here (a) Q_{wW} and Q_{wTB} respond almost instantaneously to the P_w drops at the beginning of each of the three depressurization steps, at which times short-lived spikes in Q_{wW} and Q_{wTB} occur, and (b) each depressurization step is accompanied by a significant step increase in Q_{wW} and Q_{wTB}. After the initial spikes, Q_{wW} and Q_{wTB} increase continuously with time during the first two depressurization periods. Q_{wW} and Q_{wTB} also increase initially (and for a long time) during the third depressurization period, but later they appear to stabilize and even decline in all cases except in Case w05—unlike Cases H and L.
- In all cases, total water inflows Q_{wTB} from the boundaries are significant, but they appear lower than Q_{wW}. The only exception is related to the w10 case, and is only temporary in duration. This is a positive development, as it indicates a more effective depressurization when the more representative flow properties of the system are used.
- At early times, water production and replenishment appear directly related to the well length W_L for the wells located at the top of the deposit. Thus, the relative magnitudes of Q_{wW} and Q_{wTB} during the first two depressurization periods increase with W_L, and the order of magnitude is w15 > w10 > w05. This relationship is attributed to the fact that early production from longer wells accesses more of the formation prior to dissociation, so water production is expected to be accordingly larger. However, the length of the well appears unrelated to water production in the long run (i.e., during the last depressurization step) because different parts of the formation with different flow properties and different S_H (and different dissociation behavior) are now accessed. Thus, for t > 285 days, Case w05 with the shortest W_L is associated with the largest Q_{wW} and Q_{wTB}, and Case w15 with the longest W_L with the smallest Q_{wW} and Q_{wTB}. This was unexpected because, in addition to the reason for the larger early Q_{wW} and Q_{wTB} expectation in longer wells that has already been discussed, such a longer well can access the deeper parts of HU-B where S_H is lower and the effective permeability higher. Between at t = 60 days and t = 285 days, there is transition of the Q_{wW} and Q_{wTB} relative magnitudes from the early regime to the final regime.
- The location of the well in relation to the top of the aquifer plays a key role. Thus, placing the top of the well 3 m below the top of HU-B in Case R results in Q_{wW} and Q_{wTB} that are

substantially larger at all times than those in all other cases (w05, w10 and w15) in this component of the study. Additionally, $Q_{wW} > Q_{wTB}$ at all times in Case R.

- As expected (or hoped for), the Q_{wW} in all cases in this part of the study do fall significantly below the upper limit of the expected water production at the site that was determined in Case H. Thus, the maximum Q_{wW} attained in Cases w05, w10 and w15 at t = 360 days range between 2.2×10^5 kg/day and 2.7×10^5 kg/day ($\approx$ 1,400 and 1,700 BBL/day), and $\max\{Q_{wW}\} \approx 3.7\times10^5$ kg/day ($\approx$ 2,350 BBL/day) in the more prolific Case R. These are not excessive Q_{wW} rates in hydrocarbon production operations, and they are all easily manageable with the facilities planned for the test.
- In a worrying sign, Q_{wTB} in all cases represents a large and increasing fraction of Q_{wW}, although smaller than those in Cases H and L, indicating relatively easy replenishment of withdrawn water by water inflows from the boundaries. An encouraging observation is that Q_{wW} consistently exceeds Q_{wTB} in all cases, except during a short interval in Case w10. This is confirmed by the evolution of the replacement ratio $R_{wR} = Q_{wTB}/Q_{wW}$ in **Figure 15(b)**, which shows R_{wR} reaching and exceeding 0.8 at the end of the first two depressurization steps, and then tending asymptotically toward a seemingly stable, long-term level of R_{wR} = 0.96 (temporary and short-term excursions to larger R_{wR} notwithstanding). A remarkable observation is that, despite different Q_{wW} and Q_{wTB} magnitudes in the four cases of this component of the study, they all appear to converge to the same long-term R_{wR} values, indicating similar water replacements. However, Case R appears to have an advantage, as the corresponding is R_{wR} generally lower (and for most of the investigated time) than that of all other cases.
- In all cases, water influx from the bottom boundary Q_{wB} consistently exceeds that from the top boundary Q_{wT} (**Figure 16**) because of (a) the permeability regime that is different than those in Cases H and L (see Section 3.1 and **Figure 9**), as well as of (b) the significantly higher S_H in the upper parts of HU-B and the correspondingly lower effective permeability at these locations (**Figure 4**). Additionally, Case R is associated with Q_{wB} and Q_{wT} that are consistently (and substantially) higher than those in all other cases in the component of the study because of the lower position of the well and its proximity to the more permeable bottom of the HU-B unit and its underlying boundary. Thus, upon first reading of the data and applying only the absolute criterion, a well placement consistent with Case R is not a desirable option, but Q_{wW} alone (i.e., the absolute production criterion) cannot be the sole criterion for the selection of the most appropriate well configuration.

4.2. Gas release, production and accumulation

Figure 17 shows the early rates (for t <= 70 days) of (a) CH_4 release from the dissociation of the hydrate Q_{mR} and (b) the total CH_4 production $Q_{mT} = Q_{mG} + Q_{mA}$ in Cases w05,w10,w15 and R. **Figure 18(a)** shows the evolution of the same rates over the t = 360 days simulation period. As in Cases H and L, the effect of the sharp P_w drops at the two depressurization steps at t = 30 days and t = 60 days in all the cases (see **Figure 8**) is obvious in the initial (and short-lived) "spikes" in Q_{mR} and Q_{mT} in **Figures 17 and 18(a)**, which denote rapid gas release and enhanced production in the immediate aftermath of the sudden P_w drop and can reach as high as 3.75×10^4 m^3/day (= 1.41×10^6 ft^3/day). Note that the fluctuations and spikes in Q_{mR} late in time (after the

last pressure drop) in **Figure 18(a)**, as well as in all other cases, are a practically inevitable occurrence in computations of hydrate dissociation: they are caused by the very dynamic coupled processes associated with dissociation and the effect of discretization. Following dissociation, the cooling and rise in pressure resulting from the release of CH_4 decelerate dissociation in the same element, causing a subsequent abrupt drop in Q_{mR}; conversely, when the dissociation front advances into a previously unaffected element, there is an initial spike in Q_{mR}. Both are very short-term responses of the system—often lasting no longer than a few seconds—and are fully captured and recorded by the timestep-based monitoring process, but the associated magnitude of $Q_{mR}\ \Delta t$ is almost insignificant in magnitude to register in the evolution of cumulative mass of released CH_4 $\int Q_{mR}\, dt$ over time—which is smooth and free of any such oscillations.

Review of **Figures 17 and 18(a)** leads to the following observations:

- For $t < 30$ days (i.e., during the first depressurization period), $Q_{mT} > Q_{mR}$ and they both increase continuously in all cases (**Figure 17**), indicating that the source of most of the produced CH_4 is exsolution from the produced water. This is an indication of weak and insufficient depressurization that cannot effect significant hydrate dissociation and cannot lead to free gas accumulation V_F in the reservoir (**Figure 18(b)**).
- For 30 days $\leq t \leq$ 60 days (i.e., during the second depressurization period), the Q_{mR} vs Q_{mT} relationship is reversed and Q_{mR} exceeds consistently Q_{mT} in all cases (**Figure 17**), indicating enhanced effectiveness of depressurization at this lower P_w level and the beginning of accumulation of free gas in the reservoir (see **Figure 18(b)**). During this period, the relative magnitudes of Q_{mR} and Q_{mT} indicate the diminishing contribution of exsolved gas to overall gas production, with Q_{mG} being the main source of Q_{mT}.
- For $t > 60$ days (i.e., during the third depressurization period at the final P_w = 2.8 MPa), the evolution of the Q_{mT} and Q_{mR} follows a pattern that involves (a) an initial phase during which Q_{mR} significantly exceeds Q_{mT} and leads to rapid and substantial V_F accumulation (**Figure 17(b)**); (b) a phase of near-parity (equality) of Q_{mT} and Q_{mR}, during which V_F either stagnates or rises slowly, (c) a phase during which Q_{mR} substantially lags Q_{mT}, necessitating CH_4 withdrawals from V_F in order to sustain production and a corresponding decline in V_F, and (d) a final phase of rough equality Q_{mT} and Q_{mR}. Such an equality can be associated with a roughly constant V_F, as production is fully supported by dissociation. These phases are evident in all four cases (with exception of Case w05, which lacks phase (c)), and the corresponding Q_{mT} and Q_{mR} patterns are all clearly reflected in **Figures 18(a) and 18(b)**. A general observation applicable to all cases is that both Q_{mT} and Q_{mR} decline substantially between the beginning of this step and the end of the simulation study at t = 360 days because of the progressive (and unavoidable) dwindling of the effectiveness of depressurization as dissociation advances deeper into HU-B.
- Q_{mR} and Q_{mT} in Case R are consistently and significantly larger than those in all other cases. Q_{mT} ranges from 11,300 m^3/day $\approx$ 400,000 ft^3/day at the beginning of the third depressurization step to $Q_{mT} \approx$ 4,550 m^3/day $\approx$ 160,000 ft^3/day at t = 360 days, at which time it is more than 50% larger than the Q_{mT} $\approx$ 2,970 m^3/day $\approx$ 105,000 m^3/day for the next best Case w05, and almost 2.5 larger than $Q_{mT} \approx$ 1,850 m^3/day $\approx$ 65,300 ft^3/day in the worst-performing Case w10. The reason for the superior performance is attributed to the location of the well below the top of the HU-B layer, i.e., below the highest S_H

occurrences that do not allow easy dissociation (thus reducing the effectiveness of the other well options), but enhance the depressurization at the deeper location of the well, the configuration of which also profits from the lower S_H (= higher effective permeability and easier dissociation) at the deeper within HU-B. The superiority of Case R is obvious and this well configuration is associated with the best overall performance because it combines the largest gas production (Q_{mT}) with the largest gas accumulation (V_F) with a reasonable water production (Q_{wW}). These results provide significant evidence in support of satisfying the relative criterion, but a final verdict can be reached after examining additional related parameters.

4.3. Water-related parameters

The aqueous production fractions $R_{mAT} = Q_{mA}/Q_{mT}$ for all cases are shown in **Figure 19(a)** provide a measure of the relative magnitudes of Q_{mA} and Q_{mG}, and of the contribution of Q_{mA} to Q_{mT}. The results confirm the observations from **Figure 17** about the large contribution of exsolved CH_4 to production Q_{mT} during the first depressurization step, as denoted by a R_{mAT} that is at a maximum during this period; R_{mAT} for the four cases ranges between 0.56 and 0.67, substantially lower than those in Cases H and L at the same time. R_{mAT} = 0.6 in the most promising (according to the earlier discussion) Case R, but this first depressurization period is of limited importance, as is the second depressurization period during which R_{mAT} in Case R drops to the best-performing (among the four cases) level of 0.25. The superiority of Case R_{mAT} becomes evident in the long-term performance during the third depressurization step, when it has consistently the lowest value among the four cases, rising to the low level of only R_{mAT} = 0.1 at t = 360 years. Such a low level indicates that the dominant contributor to the overall gas production is free gas from hydrate dissociation, indicating strong end effective depressurization that limits exsolved gas contribution to only 10% (at worst) of the total. The mild upward long-term trend in R_{mAT} in all cases is an indication of continuing water inflows from the boundaries.

Figure 19(b) shows the evolution of the instantaneous or cumulative water-to-gas ratios (R_{Qwm} or R_{Mwm}, respectively) in the four cases, and in combination with the results in **Figure 19(a)**, provide evidence in support of satisfying the relative production criterion in the evaluation of a hydrate deposit as a production target. They all decline initially from very high levels (>400) to between ≈ 250 and ≈ 210 kg of H_2O per ST m^3 of CH_4 at the end of the first depressurization step, when water is the only produced fluid and the only source of CH_4 from exsolution (**Figure 17**). Beginning with the second depressurization period, and clearly in the all-important long-term third depressurization period, Case R has the best R_{Qwm} and R_{Mwm} performance, dropping to R_{Qwm} = 15 at t = 60 days, rising slowly (because of continuing water inflows from the boundaries) to R_{Qwm} = 80 kg of H_2O per ST m^3 of CH_4 at t = 360, and being consistently lower (= better) than the R_{Qwm} and R_{Mwm} of all other cases. Thus Case R may have the largest (but still easily manageable) water production Q_{wW}, but has the best R_w, Q_{mT}, Q_{mR}, V_F, R_{mAT} and R_{Qwm}/R_{Mwm} performance, satisfies the relative production criterion for an acceptable absolute water production criterion, and is, thus, the best well configuration—among the four well options investigated in this component of the effort—for application to the field test.

4.4. Response at the observation wells

Figures 20(a), **20(b)** and **20(c)** show the evolution of P, T, and of the pore-volume averaged gas saturation $\acute{S}_G$, respectively, in the two observation wells in Cases w05, w10, w15 and R. While all the well configurations perform well in the response registered in the observation wells, Case R appears far superior than the rest and confirm that both the W30 and W50 well are well positioned to fulfill their role by capturing and monitoring effectively the system changes and the corresponding behavior of all the key variables (P, T and $\acute{S}_G$) during a test of production from the HU-B layer.

The P-responses at the W30 and W50 wells (**Figure 20(a)**) are not a direct function of the well length: w10 and w15 have very similar response initially, but the two deviate later with the w15 case appearing less responsive; the response in Case w05 is the slowest and most attenuated. In Case R, the position of the well deeper within HU-B allows stronger depressurization over a longer distance for reasons already explained: the result is that both the W30 and W50 wells capture easier, more vividly, and more accurately the system response to all the P_w drops at the beginning of each depressurization step, as marked by the strongest inflection points and the steepest drops in P (over 1 MPa at some points in time) that reach the lowest P-levels among the four cases. P-increases for t > 180 days are attributed to water inflows from the boundaries.

The superiority of Case R, as related to the performance of the observation wells in the hydrate production test, is even more evident in the more relevant T-response (an indirect indicator of hydrate dissociation) and the most importance S_G response (= the only indisputable evidence of hydrate dissociation in HU-B). As in the case of P-monitoring, the T- and S_G-responses at the W30 and W50 wells (**Figure 20(b)**) follow the same pattern discussed in the P-response. The responses in Case R are the earliest, fastest and strongest: the onset of the depressurization steps are clearly identified in the T-responses, which register temperature declines ΔTs at least 1 ºC larger than in the next best case; free gas evolves in the W30 and W50 wells as early as t =35 days and 50 days, respectively—in both wells 10 days earlier than in the next best case—and reach higher $\acute{S}_G$ levels than all the other cases. Note the warming trend in the observation wells in **Figure 20(b)**, which begins at the time of the increase in the P-response (**Figure 20(a)**) and is also attributed to warm water inflows from the boundaries. The declining $\acute{S}_G$ after a peak is reached (common to all cases in this study) is attributed to the weakening of depressurization and dissociation as time advances, as well as to dissolution into the invading water for t > 180 days.

4.5. Spatial distributions of key variables

The spatial distributions of P over time in Cases w05, w10, w15 and R are shown in **Figure 21**, and describe the P-response of the system beginning at t = 90 days, i.e., 30 days after the third (and last) step of depressurization. Case w05 is associated with the lowest depressurization in terms of magnitude and volumetric extent, with most of the depressurization effect concentrating in a small region at the top of HU-B. The depressurization patterns in Cases w10 and w15 are quite similar in terms of footprint; as expected, the strongest ΔP is concentrated at the top of the hydrate deposits. The depressurization front appears to reach earlier and further into the HU-B in Case w15, but appears to affect a larger volume in Case w10. The superiority of depressurization in Case R is obvious, as evidenced by the largest footprint of reduced pressure and the largest pressure drop. Note that the upper part of the HU-B, which has the highest S_H and is the most resistant to depressurization and hydrate dissociation, shows a limited pressure drop

but contains depressurization and directs/focuses it in the more permeable (and easier dissociated) hydrate body lower in the deposit.

The *T*-distributions in **Figure 22** are consistent with the information gleaned from the *P*-distributions of **Figure 21** and provide indirect evidence of hydrate dissociation, which is not sufficiently quantitative to relate consistently to the observations from **Figure 18(a)**. Case w05 is associated with the most localized ΔT with the smallest footprint, which is concentrated in the upper part of HU-B, leaving the lower part practically undisturbed. The ΔT and the low-*T* footprint in Case w10 are clearly larger than in Case w15 until t = 180 days, and this is consistent with the corresponding relative magnitudes of Q_{mR} and Q_{mT} in **Figure 18(a)** at these time; not much can be gleaned from the *T*-distributions in the two cases. Case R exhibits clearly the largest ΔT over the largest reservoir volume, and this qualitatively consistent with the largest Q_{mR} and Q_{mT} at all times. Note that the *T*-distribution in this case indicates cooling all the way to the top of HU-B, at a place where the pressure regime denoted rather limited dissociation activity.

Of particular interest are the S_G spatial distributions in **Figure 23**. One clear observation is that the amount of free gas is the largest in Case R at all times, and this is supported by the V_F results in **Figure 18(b)**. Visual inspection of **Figure 23** confirms that the S_G distributions are in agreement with the observations (a) of the lowest V_F occurring in Case w05 at t = 90 days and (b) of very similar V_F levels in Cases w10 and w15 at the same time. The heterogeneity in the distributions (and the fact that some color variations may be indiscernible to the naked eye) do not allow any more correlations of the S_G distributions to the results of **Figure 18(a)**. The S_G spatial distributions in this and the other cases are highly heterogeneous, with free gas occurring in "stringers" that correspond to layers that are conducive to easy hydrate dissociation some of which extend deep into the formation. In cases w05, w10 and 15, the longest such stringers occur at the top of the formation, where the top of the well is located. In case R, no free gas evident in near the top of the formation and the longest such stringer appears to coincide with the top of the well. These top stringers appear to weaken (faintly) over time, and this is attributed to exhaustion of the free gas there because of continuing production.

Beginning with an initial highly heterogeneous hydrate distribution (**Figure 4**), the evolution of the S_H distributions during the production test in **Figure 24** exhibits patterns of even stronger heterogeneity which can provides some insight in the pattern of hydrate dissociation that develop in the four well configuration cases. Locating the well at the top of HU-B and limiting W_L to 5 m limits hydrate dissociation to the upper (less permeable, because of a larger S_H) part of the deposit, leaving the lower reaches of the hydrate accumulation practically unaffected. The longer well in Case w15 accesses a considerable fraction of the HU-B profile and dissociates a significant fraction of the hydrates lower in the deposit, but this does not appear to lead to larger Q_{mR} and Q_{mT}, as the results in **Figure 18(a)** clearly indicate. Actually, the Q_{mR} and Q_{mT} in Case w15 are the lowest among all cases for a long time, and clearly at the end of the simulation at t = 360 days. This is attributed to a weakening of the depressurization effect over the larger volume related to the longer W_L and the easy access to the lower S_H (and less CH_4-releasing) layers deeper in HU-B. This appears to be consistent with the dissociation patterns in Case w10, which does not seem to access the deeper parts of HU-B but yields higher Q_{mR} and Q_{mT}.

The superior performance of Case R is obvious in the largest disappearance of hydrate among all the cases in **Figure 24**; the depressurization concentration in a smaller volume is the reason for the highest Q_{mR} and Q_{mT}, even after accessing the low-yielding, low-S_H lower parts of

HU-B. The patterns of hydrate dissociation in all cases are consistent with the stringers in the S_G distributions noticed in **Figure 23**. Note that there is significant evidence of secondary hydrate formation in practically all cases, as indicated by the color variations in the layers that are adjacent to hydrate-free (and bearing free gaseous CH_4) occurrences. This is inevitable, given the coexistence of H_2O and free CH_4 (**Figure 23**) in a low-T environment (**Figure 22**) at these locations.

5. RESULTS AND DISCUSSION – CASES R, L2m, L6m and D15

5.1. Water production

Having determined the advantages of the well length W_L = 10 m and of the well placement 3 m below the top of HU-B, the next set of simulations aimed to determine whether production operation practices using this well configuration could further optimize production by (a) minimizing water production without adversely affecting the gas production estimates in Case R or (b) by enhancing and maximizing gas production for a reasonable and easily manageable water production. As previously discussed (see Section 2.6), the flow properties in this component of the study were those corresponding the more representative C-interpretation of the field data (see Section 2.3). **Figure 25a** shows the evolution over time of the mass flow rates of water (a) produced at the well Q_{wW} and (b) the total water inflow from the boundaries Q_{wTB} in Cases L2m, L6m and D15. In this and all subsequent figures, the results for Case R are included for comparison.

Review of the results in this figure reveals the following:

- Case D15 exhibits the same behavior observed in similar cases involving the same well configuration and a step-wise depressurization process (i.e., Cases w05, w10, w15 and R): (a) Q_{wW} and Q_{wTB} respond almost instantaneously to the P_w drops at the beginning of each of the three depressurization steps, at which times short-lived spikes in Q_{wW} and Q_{wTB} occur, (b) each depressurization step is accompanied by a significant step increase in Q_{wW} and Q_{wTB}, (c) after the initial spikes, Q_{wW} and Q_{wTB} increase continuously, and (d) they also increase initially (and for a long time) during the third depressurization period, but later they appear to stabilize and even decline.
- As expected, in Cases L2m and L6m, the linearly-declining P_w (see **Figure 8**) results in smooth linear increases in Q_{wW} and Q_{wTB} that are free of spikes. The end of depressurization at t = 60 days (Case L2m) and t = 180 days (Case L6m) at the final P_w = 2.8 MPa is marked by a change (a reduction) in Q_{wW} and Q_{wTB}, which, however, continue to increase. As in Cases R and D15, Q_{wW} and Q_{wTB} in cases L2m and L6m appear to stabilize or even decline at late times.
- In all cases, total water inflows Q_{wTB} from the boundaries are significant, but consistently lower than Q_{wW}. This is attributed to the more effective depressurization under these conditions for reasons previously discussed in Section 4.1.
- For a given rate of depressurization (linear vs. step-wise), Q_{wW} and Q_{wTB} appear directly related to the rate of depressurization. The faster the depressurization, the larger the Q_{wW} and Q_{wTB}. For depressurization to the final P_w = 2.8 MPa within the same time frame (i.e., cases R and L2m), linear depressurization is shown to enhance Q_{wW} and Q_{wTB}. This was

expected because the slow depressurization delays significantly hydrate dissociation and the emergence of gaseous CH_4, allowing more time for the flow of water that is uninhibited by relative permeability restrictions imposed by the evolution of gas. The lowest Q_{wW} and Q_{wTB} are associated with the lengthy (6 month-long) linear depressurization in Case L6m.

- As expected (or hoped for), the Q_{wW} in all cases in this component of the study do fall substantially below the upper limit determined in Case H. Thus, the maximum Q_{wW} in Cases L2m and L6m during the 360 days of the study are about 4.0×10^5 kg/day and 3.7×10^5 kg/day (≈ 2,500 and 2,300 BBL/day), respectively, and $\max\{Q_{wW}\} \approx 4.1\times10^5$ kg/day (≈ 2,580 BBL/day) in the more prolific Case D15. These Q_{wW} rates (a) do not differ significantly from each other and from Case R (in which $\max\{Q_{wW}\} \approx 3.7\times10^5$ kg/day ≈ 2,350 BBL/day), and (b) are not excessive and are all easily manageable with the facilities planned for the test.
- As in the previous cases (Section 4.1), Q_{wTB} in all the cases here represents a large and increasing fraction of Q_{wW}, indicating relatively easy replenishment of withdrawn water by water inflows from the boundaries. This is a consistent feature of the hydrate deposit in HU-B. A positive issue is that Q_{wW} consistently exceeds Q_{wTB} in all cases, as is confirmed by the evolution of the replacement ratio $R_{wR} = Q_{wTB}/Q_{wW}$ in **Figure 25(b)**, which shows R_{wR} in all cases tending asymptotically toward a seemingly stable, long-term level of R_{wR} = 0.96 (temporary and short-term excursions to larger R_{wR} notwithstanding), indicating similar water replacements. The early R_{wR} performance indicates the superiority of Case D15 over that in Case R, as evidenced with the lower R_{wR} associated with these cases that provides further evidence of the benefits of early/fast depressurization. The situation is more complicated in the linearly declining cases: R_{wR} is indeed lower (indicating less water inflows) in Case L2m, but the situation is later reversed.
- As in all previous cases, water influx from the bottom boundary Q_{wB} consistently exceeds that from the top boundary Q_{wT} (**Figure 26**) in all the cases investigated here for the same reasons discussed previously—namely because of the significantly higher S_H in the upper parts of HU-B and the correspondingly lower effective permeability at these locations (**Figure 4**). This common feature appears to be another characteristic of the deposit at the HU-B. Additionally, Case D15 is associated with Q_{wB} and Q_{wT} that are consistently (and substantially) higher than those in all other cases in the component of the study. Thus, upon first reading of the data and applying only the absolute criterion, the well configuration and the P_w schedule of Case D15 is not a desirable option, but Q_{wW} alone (i.e., the absolute production criterion) cannot be the sole criterion for the selection of the most appropriate production system.

5.2. Gas release, production and accumulation

Figure 27(a) shows the evolution of (a) CH_4 release from the dissociation of the hydrate Q_{mR} and (b) the total CH_4 production $Q_{mT} = Q_{mG} + Q_{mA}$ in Cases L2m, L6m and D15 over the t = 360 days simulation period. The results for Case R are also included for comparison. As in Case R, the effect of the sharp P_w drops at the two depressurization steps at t = 30 days and t = 60 days in Case D15 (see **Figure 8**) is obvious in the initial (and short-lived) "spikes" in Q_{mR} and Q_{mT} in

Figure 27(a). The linear Pw decline does not allow such spikes in Cases L2m and L6m. Review of **Figure 27(a)** leads to the following observations:

- Case D15: For reasons already explained (Section 4.2), for $t < 15$ days (i.e., during the first depressurization period), $Q_{mT} > Q_{mR}$ and they both increase continuously because the source of most of the produced CH_4 is exsolution from the produced water. The Q_{mR} vs Q_{mT} relationship is reversed during the second depressurization period (15 days $\leq t \leq 30$ days), during which the enhanced effectiveness of depressurization at the lower P_w level generates accumulating free gas in the reservoir (see **Figure 27(b)**), with Q_{mG} becoming the main source of Q_{mT}. The Q_{mT} and Q_{mR} follow the pattern identified in Case R (Section 4.2). In the third depressurization period ($t > 30$ days), initially and for a long time (to $t \approx$ 250 days) Q_{mR} significantly exceeds Q_{mT} and is the reason for the rapid, substantial and continuous V_F accumulation seen in **Figure 27(b)**. This is followed by a phase of near-parity of Q_{mT} and Q_{mR}, during which V_F rises slowly, and a final phase during which $Q_{mT} > Q_{mR}$, necessitating CH_4 withdrawals from a declining V_F in order to sustain production. Note that, as in all previous cases, both Q_{mT} and Q_{mR} decline significantly between the beginning and the end of the final depressurization step, indicating that depressization becomes weaker and less effective as the dissociation front moves away from the well and deeper into the hydrate-bearing formation.
- Cases L2m and L6m: Q_{mR} and Q_{mT} increase continuously and monotonically during the periods of linear depressurization (**Figure 8**), during which time $Q_{mR} > Q_{mT}$ and the difference Q_{mR}-Q_{mT} also continues to increase. After the $\min\{P_w\} = 2.8$ MPa is reached, the same phases identified in Cases R and D15 are evident, with the correspondingly similar behavior in the evolution of the related V_F (**Figure 27(b)**).
- In Case D15, Q_{mT} ranges from about $Q_{mT} \approx 15{,}000$ m^3/day $\approx 530{,}000$ ft^3/day at the beginning of the third depressurization step to $Q_{mT} \approx 4{,}950$ m^3/day $\approx 175{,}000$ ft^3/day at $t = 360$ days, i.e., about 9% larger than $Q_{mT} \approx 4{,}550$ m^3/day $\approx 160{,}000$ ft^3/day for the reference Case R at the same time. However, single point comparisons at the end of the study period are insufficient to capture the overall system performance and to serve as the basis of comparison and evaluation. Unlike the results in the previous section of this study (Section 4.2, **Figure 17**), the complexity and significant variability of the Q_{mR} and Q_{mT} in **Figure 27(a)** does not allow easy and clear identification of the best performing option. The comparison of the cumulative volumes of released and produced CH_4 in **Figure 28** offers a much more robust measure of the relative performance of the various options investigated here and provides convincing evidence of the superiority of Case D15, which is associated consistently with the largest V_{mT}, V_{mG} and V_{mA} in all cases and is far superior to Case R (22+% larger V_{mT}). The largest V_{mG} is Case D15 indicates that this option (a combination of a 10 m-well located 3 m below the top of the HU-B and rapidly depressurized in a step-wise manner) maximizes hydrate dissociation and gas production without any increase to the contribution V_{mT} of the exsolved gas, which is is limited roughly the same in all cases (**Figure 28**). The rapidly depressurized linear Case L2m has the next best performance, and Case L6m has the worst. The superiority of Case D15 is obvious, as attested to by the largest gas production (V_{mT}) and the largest gas accumulation (V_F) that are associated with a water production rate (Q_{wW}) that is not excessive but easily

manageable and only slightly larger than the that in the previous best Case R, which case D15 significantly outperforms. These results suggest that case D15 may be the most promising option that satisfies the relative production criterion, but a final determination will be made after examining additional related parameters.

5.3. Water-related parameters

In terms of both patterns and values, the aqueous production fraction $R_{mAT} = Q_{mA}/Q_{mT}$ in **Figure 29(a)** in Case D15 show the same contributions of exsolved CH_4 to production Q_{mT} that were observed in Case R during all three depressurization steps: the R_{mAT} values in the two cases practically coincide, but this happens earlier in Case D15, further confirming its advantage. Actually, all the R_{mAT} curves in **Figure 29(a)** appear to practically converge for t > 150 days, exhibiting the same slight upward trend observed in **Figure 19(a)**. The discussion and observations related to the earlier **Figure 19(a)** apply here and will not be repeated. The R_{mAT} evolution of the linearly depressurized Cases L2m and L6m initially follow a different pattern, which is characterized by a gradual (as opposed to step-wise) decline until they meet they converge with the common R_{mAT} curves at about t = 60 days (Case L2m) and t = 160 days (Case L6m), respectively. Clearly, Case L6m has the worst overall R_{mAT} performance, but Case L2m has a R_{mAT} performance that is closer (but still inferior to) that in case D15 which is the clear winner.

The instantaneous water-to-gas ratios R_{Qwm} in **Figure 29(b)** follows the same pattern with those of R_{mAT} in **Figure 29(a)**: in Case D15, the pattern of evolution is identical with that in the reference Case R shows and R_{Qwm} have the same values during each depressurization step, and this provides an advantage to Case D15 because of the shorter duration of the first two steps. Because of the similarity, the discussion in Section 4.3 applies and will not be repeated here.

R_{Qwm} in Cases L2m and L6m decline continuously and smoothly, but they are at much higher levels until all R_{Qwm} converge at the same times that this happens in the R_{mAT} curves of **Figure 29(a)**. The evolution of the R_{mAT} and R_{Qwm} provide the final evidence of superiority of Case D15 by satisfying the relative production criterion in the evaluation of a hydrate deposit as a production target. Thus, Case D15 emerges as a clear winner: it may have the largest (but not excessive and still easily manageable) water production Q_{wW}, but has the best performance of the relative production criterion by virtue of its highest R_w, Q_{mT}, Q_{mR}, V_F, R_{mAT} and R_{Qwm} values, and is the most promising production system—among the seven cases, i.e., w05, w10, w15, R, L2m, L6m and D15, investigated in this study—for application to the field test.

5.4. Response at the observation wells

The importance of the observation wells and their function in the monitoring and analysis of the processes occurring in a hydrate deposit under production during depressurization-induced dissociation have been previously discussed in detail (Sections 3.4 and 4.4) and will not be further elaborated here. **Figures 30(a)**, **30(b)** and **30(c)** show the evolution of P, T, and $\acute{S}_G$, respectively, in the two observation wells W30 and W50 in Cases L2m, L6m and D15. The results for Case R are included for comparison. Inspection of these figures indicates the clear superiority of Case D15: it is invariably associated with the fastest and strongest response of all three monitored parameters in both wells. Actually, the response of the three monitored variables

at the W50 well in Case D15 are shown to register earlier than that at the W30 well in Case R, despite the latter being 20 meters closer to the production well.

Case L2m is shown to have the 2nd best response in all three monitored parameters at both observation wells, exceeding the performance of the reference Case R. The common thread in this (and the previous) very satisfactory performance of Case L2m compared to that in Case D15 (see **Figures 25 to 29**) is the fast rate of depressurization, which appears to produce the best overall results. The slow and generally unsatisfactory well response (and overall performance) in Case L6m is ascribed to the slow rate of depressurization, probably eliminating it for further consideration in the design and execution of the field test.

5.5. Spatial distributions of key variables

The evolution of the spatial distributions of P, T, S_G and S_H in the best-performing Case D15 is shown in **Figure 31**. Although the contour plots in this figure cannot be quantitatively related to the various production variables depicted in **Figures 25 to 29**, they are useful to identify the HU-B regions and locales where dissociation is focused and where gas accumulates and in the qualitative analysis of the overall system response during the production test. Comparison of the distributions in **Figure 31** to those corresponding to Case R, especially in **Figures 21 to 24,** provides qualitative confirmation of the superior performance of Case D15.

Thus, the P-distributions in **Figure 31** show an unmistakably larger depressurized volume than that in Case R in **Figure 21**. The same is the case with the T-distribution in **Figure 31**, which shows more severe cooling over a larger reservoir volume than that in **Figure 21**, and it even shows significant cooling deep in the HU-B at t = 360 days when dissociation in case R is diminished for reasons already described. Comparison of the S_G distributions in the two cases cannot lead to any authoritative conclusions at t = 90 and 180 days, but the significantly larger accumulation of free gas in terms of footprint and S_G level is more than obvious and in qualitative agreement with the V_F results in **Figure 27**. Comparison of the S_H distributions in the two cases shows significant more hydrate dissociation in Case D15, evidenced by longer hydrate-free layers that coincide with the occurrences of free gas at high S_G at all times, and which are bracketed by layers that show evidence of secondary hydrate formation; hydrate dissociation at the deeper reaches of HU-B appear to be similar in both cases. The spatial distributions of the key conditions and variables in **Figure 31** are consistent with, and provide qualitative confirmation of, the superiority of Case D15 as the most promising design for the production test.

6. SUMMARY AND CONCLUSIONS

The main objective of this study was to estimate the fluid production rates (with emphasis on the water production) under a variety of conditions and production scenarios, and to gain insights that can lead to an optimization of the design and management of the field test. The effort did not focus solely on strategies to minimize water production in absolute terms, but to determine the test design that best serves the totality of objectives and expectations of this test: a) a modest and easily managed water production rate that is b) associated with the highest gas production rate and the strongest system response during the field test. The results of this study can be used to guide decisions about production strategies not only in the this and possibly other long-term tests, but also in future commercial-scale operations. Although the field test is expected to last

about 180 days, our simulation extended to 360 days in an effort to glean a better understanding of the longer-term behavior of the system.

We compared key performance metrics for the various production scenarios, and their evolution over the duration of the test. Based on the results of this study, the following conclusions can be reached:

(1) The first part of the study that was conducted using two limiting sets of flow properties —Cases H and L, corresponding to maximum and minimum permeabilities, respectively —involved a three-step depressurization regime at 30-day intervals. These initial simulations indicated the futility of attempts at gas production from the hydrates at that site *if the actual flow properties turned out to be close to those in either Case H or L*: Case H would be hampered by prohibitively high water production despite a reasonable (but not spectacular) gas production rate Q_{mT}, and Case L would have a minimal Q_{wW} but an unacceptably Q_{mT}. Additionally, observation wells located at r = 30 m and r = 50 m from the production well would not be able to provide much useful information in Case H and none in Case L.

(2) The Cases wX—with X representing the length of the production interval (X = 5, 10, and 15 m—involved the same three-step depressurization regime as Cases H and L, but were based on the more representative set of flow properties. The well length in additional Case R was also 10 m long, but the top of the production interval was placed 3 m below the top of the targeted HU-B layer. Despite having the largest Q_{wW}, Case R was determined to be the best performing option *in this part of the study* because (a) Q_{wW} was still relatively modest and manageable, it had (b) the largest Q_{mT} relative to Q_{wW} and (c) to all other related parameters, and (d) was associated with best response in both observation wells.

(3) In the third part of the study we investigated the effect of depressurization mode and rate for well with the configuration of that in Case R. The cases investigated here included depressurizations (a) in a three-step regime at 15-day intervals (Case D15) and (b) linearly in 60 and 180 days (Cases L2m and L6m, respectively). Despite having the largest Q_{wW}, Case D15 was determined to be the best performing option *in this entire study* because (a) Q_{wW} was still relatively modest and manageable, it had (b) the largest Q_{mT} relative to Q_{wW} and (c) to all other related parameters, and (d) was associated with best response in both observation wells, all significantly better than the equivalent in Case R.

(4) For the reasons listed above, Case D15 is the most desirable option for well design and management of production from the HU-B system.

(5) It appears that the overall production performance (and the corresponding response at the observation wells) is a direct function of the rate of depressurization. Thus, the two fastest-depressurizing Cases, D15 and L2m, have the best performance, and the slowly-depressurizing Case L6m has the worst.

(6) The range within which Q_{wW} varies when the more representative set of properties is used is rather limited; the expected magnitudes are all relatively modest and easily manageable. Nome of the tested variations in well configuration and depressurization management managed to significantly reduce Q_{wW} without simultaneously affecting adversely (and severely) the corresponding gas production.

(7) In all seven cases investigated in this study, a large fraction of the produced water was

replenished by inflows from the top and bottom boundaries of the targeted HU-B system. Inflows from the bottom boundary are consistently the main source of the replenishing water. The long-term replenishment fraction R_{wTB} in all cases converged to about 96%, was consistent across the spectrum of the investigated cases, and in some cases reached and exceeded 100%. None of the investigated cases/options managed to reduce the long-term R_{wTB} below the 96% level, and this was true even in cases of low gas production. These substantial boundary water inflows are an unavoidable feature of the particular HU-B formation and cannot be easily mitigated by means of hydraulic control.

(8) Continuing inflows from the boundaries and progressively weakening depressurization as time advances are the reason for increasing long-term contributions of CH_4 from exsolution and diminishing responses at the observation wells.

ACKNOWLEDGMENT

This work was supported by the Assistant Secretary for Fossil Energy, Office of Natural Gas and Petroleum Technology, through the National Energy Technology Laboratory, under the U.S. Department of Energy, Contract No. DE-AC02-05CH11231. This research used the Lawrencium computational cluster resource provided by the IT Division at the Lawrence Berkeley National Laboratory, supported by the Director, Office of Science, Office of Basic Energy Sciences, of the U.S. Department of Energy under Contract No. DE-AC02-05CH11231.

Alaska gas hydrate research is being conducted as a collaboration between Japan MH21-S and the U.S. DOE-NETL Gas Hydrate R&D program. The authors would like to express their sincere appreciation to the U.S. DOE-NETL, and the Japan Ministry of Economy, Trade, and Industry for providing the permission to disclose this research. Any use of trade, product, or firm names is for descriptive purposes only and does not imply endorsement by the U.S. Government or the Japanese Government.

REFERENCES

(1) Boswell, R. and Collett, T.S., 2011. Current perspectives on gas hydrate resources. *Energy & Environmental Science*, **4** (4): 1206-1215.

(2) Boswell, R., Schoderbek, D., Collett, T.S., Ohtsuki, S., White, M. and Anderson, B.J., 2017. The Iġnik Sikumi Field Experiment, Alaska North Slope: Design, Operations, and Implications for CO2–CH4 Exchange in Gas Hydrate Reservoirs. *Energy & Fuels* **31**(1): 140-153.

(3) Dallimore, S.R., Yamamoto, K., Wright, J.F. and Bellefleur, G., 2012. Proof of concept for gas hydrate production using the depressurization technique, as established by the JOGMEC/NRCan/Aurora Mallik 2007–2008 Gas Hydrate Production Research Well Program. *Geological Survey of Canada, Bulletin* **601**: 1-15.

(4) Kurihara, M., Sato, A., Funatsu, K., Ouchi, H., Masuda, Y., Narita, H. and Collett, T.S., 2011. Analysis of formation pressure test results in the Mount Elbert methane hydrate reservoir through numerical simulation. *Marine and Petroleum Geology* **28**: 502-516.

(5) Konno, Y., Kato, A., Yoneda, J., Oshima, M., Kida, M., Jin, Y., Nagao, J. and Tenma, N.,

2019. Numerical analysis of gas production potential from a gas-hydrate reservoir at Site NGHP-02-16, the Krishna–Godavari Basin, offshore India–Feasibility of depressurization method for ultra-deepwater environment. *Marine and Petroleum Geology* **108**: 731-740.

(6) Yamamoto, K., Suzuki, K., Wang, X., Matsunaga, T., Nishioka, I., Nakatsuka, Y. and Yoneda, J., 2019. The second offshore production test of methane hydrates in the Eastern Nankai Trough and site characterization efforts. Fire in the Ice: Department of Energy, Office of Fossil Energy, National Energy Technology Laboratory, *Methane Hydrate News Letter* **19** (1): 9-15.

(7) Dallimore, S.R., Wright, J.F., Yamamoto, K. and Bellefleur, G., 2012. Proof of concept for gas hydrate production using the depressurization technique, as established by the JOGMEC/NRCan/Aurora Mallik 2007-2008 Gas Hydrate Production Research Well Program. *Bulletin of the Geological Survey of Canada* **601**: 1-15.

(8) Ashford, D.I., Numasawa, M., Martin, C.K., Yamamoto, K., Dallimore, S.R., Wright, J.F., Nixon, F.M., Applejohn, A. and Taylor, A.E., 2012. Overview of engineering and operations activities conducted as part of the JOGMEC/NRCan/Aurora Mallik 2007–2008 Gas Hydrate Production Research Well Program, Part A: 2007 field program. Scientific results from the JOGMEC/NRCan/Aurora Mallik 2007-2008 gas hydrate production research well program, pp.35-51.

(9) Yamamoto, K., Boswell, R., Collett, T., Dallimore, S., Lu, H., 2022. Review of past gas production attempts from subsurface gas hydrate deposits and necessity of long-term production testing. *Energy & Fuels*. https://pubs.acs.org/doi/10.1021/acs.energyfuels.1c04119

(10) Li, J.-F., Ye, J.-L., Qin, X.-W., Qiu, H.-J., Wu, N.-Y., Lu, H.-L., Xie, W.-W., Lu, J., Peng, F., Xua, Z.-Q., Lu, C., Kuang, Z.-G., Wei, J.-G., Liang, Q.-Y., Lu, H.-F. and Kou, B.-B., 2018, The first offshore natural gas hydrate production test in South China Sea. *China Geology* **1**: 5–16.

(11) Moridis, G. J., Collett, T. S., Boswell R., Kurihara M., Reagan M. T., Koh C., and Sloan E. D. 2009. Toward Production From Gas Hydrates: Current Status, Assessment of Resources, and Simulation-Based Evaluation of Technology and Potential, *SPE Res Eval & Eng* **12** (5): 745-771. SPE-114163-PA.

(12) Boswell, R., Hancock, S., Yamamoto, K., Collett, T., Pratap, M., Lee, S.-R., 2020. Natural gas hydrates: status of potential as an energy resource, In: T.M. Letcher (Editor), Future Energy (Third Edition). Elsevier, Boston, pp. 111-131.

(13) Moridis, G.J., Collett, T.S., Pooladi-Darwish, M., Hancock, S., Santamarina, C., Boswell, R., Kneafsey, T., Rutqvist, J., Kowalsky, M.J., Reagan, M.T., Sloan, E.D., Sum, A.K., and Koh, C., 2011, Challenges, Uncertainties and Issues Facing Gas Production From Hydrate Deposits in Geologic Systems. *SPE Res. Eval. & Eng* **14** (1): 76-112.

(14) Boswell, R., Myshakin, E., Moridis, G.J., Konno, Y., Collett, T.S., Reagan, M.T., Ajayi, T., Seol, Y., 2018, India National Gas Hydrate Program Expedition 02 summary of scientific results: Numerical simulation of reservoir response to depressurization, J. *Marine and Petroleum Geology* **108**: 154-166.

(15) Moridis, G., M.T. Reagan and A.F. Queiruga, 2019. Gas Hydrate Production Testing: Design Process and Modeling Results, OTC-29432-MS, paper presented at the 2019 Offshore Technology Conference, 6 – 9 May 2019, Houston, Texas.

(16) Boswell, R., Collett, T., Okinaka, N., Hunter, R., Suzuki, K., Tamaki, M., Yoneda, J., Haines, S., Myshakin, E., Moridis, G., 2022. Alaska North Slope Hydrate-01 Stratigraphic Test

Well Program: Technical Results. *Energy & Fuels* (to be submitted – pending PBU approval)

(17) Collett, T., Zyrianova, M., Okinaka, N., Wakatsuki, M., Boswell, R., Marsteller, S., Minge, D., Crumley, S., Itter, D., Hunter, R., Garcia-Ceballos, A., Jin, G., 2022. Design and operations of the Hydrate-01 stratigraphic test well, Alaska North Slope. *Energy & Fuels* https://pubs.acs.org/doi/10.1021/acs.energyfuels.1c04087

(18) Haines, S. S., Collett, T., Yoneda, J., Shimoda, N., Boswell, R., Okinaka, 2022, Gas Hydrate Saturation Estimates, Gas Hydrate Occurrence, and Reservoir Characteristics Based on Well Log Data from the Hydrate-01 Stratigraphic Test Well, Alaska North Slope, *Energy & Fuels* https://pubs.acs.org/doi/10.1021/acs.energyfuels.1c04100

(19) Tamaki, M., Fujimoto, A., Boswell, R., Collett, T., 2022. Geological reservoir characterization of a gas hydrate prospect associate with the Hydrate-01 stratigraphic test well, Alaska North Slope. *Energy & Fuels* https://pubs.acs.org/doi/10.1021/acs.energyfuels.2c00336

(20) Uchida, S., Seol, Y., Yamamoto, K.,2022. Sand migration simulation during gas production from gas hydrate reservoir at Kuparuk State 7-11-12 site in the Prudhoe Bay Unit, Alaska. *Energy & Fuels* https://pubs.acs.org/doi/10.1021/acs.energyfuels.2c00046

(21) Nakajima, C., Ouchi, H., Tamaki, M., Akamine, K., Sato, M., Otsuki, S., Naiki, M., 2022. Sensitivity and uncertainty analysis for natural gas hydrate production testing in Alaska. *Energy & Fuels* https://pubs.acs.org/doi/10.1021/acs.energyfuels.2c00335

(22) Myshakin, E., Garapati, N., Seol, Y., Gai, X., Boswell, R., Ohtsuki, S., Kumagai, K., Sato, M., Suzuki, K., Okinaka, N., 2022. Numerical simulations of depressurization-induced gas hydrate reservoir (B1 sand) response at the Prudhoe Bay Unit Kuparuk 7-11-12 pad on Alaska North Slope. *Energy & Fuels* https://pubs.acs.org/doi/10.1021/acs.energyfuels.1c04099.

(23) Moridis, G.J., Reagan, M.T., Liu, Y. 2022. Numerical Simulations in Support of a Long-Term Test of Gas Production from Hydrate Accumulations on the Alaska North Slope: Reservoir Response to Interruptions of Production (Shut-Ins). *Energy & Fuels*, 36(7): 3496-3525.

(24) Zhang, J., Development of a Parallel Geomechanics Code Based on the Message-Passing-Interface (MPI) Approach and Iterative Coupling With a Parallelized Flow and Thermal Simulator for the Analysis of System Behavior in Hydrate-Bearing Geologic Media, PhD Dissertation, Petroleum Engineering Dept., Texas A&M University, College Station, Texas, August 2021.

(25) Zhang, J., G.J. Moridis and T. Blasingame, Message Passing Interface (MPI) Parallelization of Iteratively Coupled Fluid Flow and Geomechanics Codes for the Simulation of System Behavior in Hydrate-Bearing Geologic Media. Part 1: Methodology and Validation, *SPE Res Eval & Eng*., 25(3), 600-620, 2022 https://doi.org/10.2118/206161-PA.

(26) Zhang, J., G.J. Moridis and T. Blasingame, Message Passing Interface (MPI) Parallelization of Iteratively Coupled Fluid Flow and Geomechanics Codes for the Simulation of System Behavior in Hydrate-Bearing Geologic Media. Part 2: Parallel Performance and Application, *SPE Res Eval & Eng*., 25(3), 621-640, 2022 https://doi.org/10.2118/209621-PA.

(27) Zhang, J., G.J. Moridis and T. Blasingame, Effect of geomechanics and of grid discretization on the predictions of production from natural hydrate deposits and of the associated geomechanical system response, *Journal of Gas Science and Engineering*, 112, Paper 204942, 2023 https://doi.org/10.1016/j.jgsce.2023.204942

(28) Moridis, G. J. and Pruess K. 2014. User's Manual for the TOUGH+ Core Code v1.5: A General-Purpose Simulator of Non-Isothermal Flow and Transport Through Porous and Fractured Media. Lawrence Berkeley National Laboratory, Berkeley, California, USA.

(29) Moridis, G. J. 2014. User's Manual for the Hydrate V1.5 Option of TOUGH+ v1.5: A Code for the Simulation of System Behavior in Hydrate-Bearing Geologic Media. Lawrence Berkeley National Laboratory, Berkeley, California, USA.

(30) Moridis, G.J., Reagan, M.T., Queiruga, A.F., Collett, T.S., Boswell, R., 2019. Evaluation of the Performance of the Oceanic Hydrate Accumulation at the NGHP-02-9 Site of the Krishna-Godawari Basin During a Production Test and During Single and Multi-Well Production Scenarios. *Marine and Petroleum Geology* **108**: 660-696.

(31) Moridis, G. J., Kowalsky, M. B., and Pruess, K. 2007. Depressurization-Induced Gas Production from Class 1 Hydrate Deposits. *SPE Reservoir Evaluation and Engineering* **10** (5): 458-481. SPE-97266-PA.

(32) Moridis, G. J. and Reagan, M. T. 2011. Estimating the Upper Limit of Gas Production from Class 2 Hydrate Accumulations in the Permafrost, 1: Concepts, System Description and the Production Base Case. *Journal of Petroleum Science and Engineering* **76**: 194-201.

(33) Moridis, G. J. and Reagan, M. T. 2011. Estimating the Upper Limit of Gas Production from Class 2 Hydrate Accumulations in the Permafrost, 2: Alternative Well Designs and Sensitivity Analysis. *Journal of Petroleum Science and Engineering* **76**: 124-137.

(34) Li, G., Moridis, G. J., Zhang, K., and Li, X.-S. 2010. Evaluation of Gas Production Potential from Marine Gas Hydrate Deposits in Shenhu Area of the South China Sea. *Energy & Fuels* **24**: 6018-6033.

(35) Moridis, G. J., Reagan M. T., Boyle, K. L., and Zhang, K. 2011c. Evaluation of the Gas Production Potential of Some Particularly Challenging Hydrate Deposits. *Transport in Porous Media* **90**: 269-299.

(36) Karypis, G. and Kumar, V. 1998. Multilevel k-way Partitioning Scheme for Irregular Graphs. *Journal of Parallel and Distributed Computing* **48** (1): 96-129.

(37) Karypis, G. and Kumar, V. 1999. Parallel Multilevel Series k-way Partitioning Scheme for Irregular Graphs. *SIAM Review* **41** (2): 278-300.

(38) Balay, S., Abhyankar, S., Adams, M. F., Brown, J., Brune, P., Buschelman, K., and Kaushik, D. 2014. PETSc User's Manual. Argonne National Laboratory, Lemont, Illinois, USA.

(39) Yoneda, J., Suzuki, K., Jin, Y., Otsuki, S., Collett, T., Boswell, R., Okinaka, N., 2022. Permeability measurement and prediction with nuclear magnetic resonance analysis of gas hydrate-bearing sediments recovered from Alaska North Slope 2018 Hydrate-01 stratigraphic test well. *Energy & Fuels* https://pubs.acs.org/doi/10.1021/acs.energyfuels.1c03810

(40) Suzuki, K.; Collett, T.; Boswell, R.; Tamaki, M.; Okinaka, N.; Sato, D. Interpretation of logging data from the Hydrate-01 Stratigraphic Test Well drilled in the Prudhoe Bay Unit, Alaska North Slope. AGU Fall Meeting, San Francisco, CA, December 10, 2019; agu.confex.com/agu/fm19/meetingapp.cgi/Paper/526858

(41) Rutqvist, J., G.J. Moridis, T. Grover, and T. Collett, 2009. Geomechanical response of permafrost-associated hydrate deposits to depressurization-induced gas production. *Journal of Petroleum Science and Engineering* **67**:1-12.

(42) Moridis, G.J., S. Silpngarmlert, M.T. Reagan, T.S. Collett, and K. Zhang, 2011. Gas Production from a Cold, Stratigraphically Bounded Hydrate Deposit at the Mount Elbert Site, North Slope, Alaska. *Marine Petrol. Geol.* **28**: 517-534.

(43) Leverett, M.C. 1941. Capillary Behavior in Porous Solids, *Trans. Soc. Pet. Eng. AIME*, 142: 152-169.

(44) van Genuchten, M.Th., 1980. A Closed-Form Equation for Predicting the Hydraulic Conductivity of Unsaturated Soils. *Soil Sci.* **44**: 892 - 898.

(45) Shi, H., Holmes, J. A., Durlofsky, L. J., Aziz, K., Diaz, L. R., Alkaya, B., and G. Oddie. 2005. Drift-Flux Modeling of Two-Phase Flow in Wellbores." *SPE J.* 10: 24–33. https://doi.org/10.2118/84228-PA

(46) Moridis, G.J., A.F. Queiruga and M.T. Reagan, 2019. Simulation of Gas Production from Multilayered Hydrate Bearing Media with Fully Coupled Flow, Thermal, Chemical, and Geomechanical Processes Using TOUGH+Millstone: Part 1: Numerical Modeling of Hydrates. *Transport in Porous Media* **128** (2): 405-430.

(47) Moridis, G. J. 2016. User's Manual of the Meshmaker v1.5 Code: A Mesh Generator for Domain Discretization in Simulations of the TOUGH+ and TOUGH2 Families of Codes. Lawrence Berkeley National Laboratory, Berkeley, California, USA.

(48) Moridis, G.J. and N. Keen, MeshMaker V2.0S and V2.0P, 2015. New Grid Generators for Complex Heterogeneous Domains in TOUGH2/TOUGH+ Simulations, Proceedings of the 2015 TOUGH Symposium, Berkeley, California, September 28-30.

(49) Kowalsky, M.B. and G.J. Moridis, 2007. Comparison of kinetic and equilibrium reactions in simulating the behavior of gas hydrates. *Energy Conversion and Management* 48(6), 1850:1863. https://doi.org/10.1016/j.enconman.2007.01.017

(50) Moridis G., M.T. Reagan and A.F. Queiruga. 2019. Gas Hydrate Production Testing: Design Process and Modeling Results, OTC-29432-MS, 2019 Offshore Technology Conference, 6 – 9 May, Houston, Texas. https://doi.org/10.4043/29432-MS

(51) Moridis, G.J., J. Kim, M.T. Reagan and S.J. Kim. 2023. Analysis of Short- and Long-Term System Response During Gas Production From a Gas Hydrate Deposit at the UBGH2-6 Site of the Ulleung Basin In the Korean East Sea, *Canadian Journal of Chem. Eng.*, 101(2):735-763 https://doi.org/10.1002/cjce.24626

(52) Moridis, G. J. and M.T. Reagan. 2007. Strategies for Gas Production from Oceanic Class 3 Hydrate Accumulations. Paper Presented at the Offshore Technology Conference, Houston, Texas, USA, 30 April - 3 May. OTC-18865-MS.

(53) Kneafsey, T.J., Y. Seol, G.J. Moridis, L. Tomutsa, and B.M. Freifeld. 2009. Laboratory Measurements on Core-Scale Sediment and Hydrate Samples to Predict Reservoir Behavior, in T. Collett, A. Johnson, C. Knapp, and R. Boswell, eds., Natural gas hydrates—Energy resource potential and associated geologic hazards: AAPG Memoir 89, p. 705–713 https://doi.org/10.1306/13201133M893364

Table 1 – Flow and thermal properties

Parameter	Value
Initial pressure P_0	Hydrostatic
Geothermal gradient dT/dz	0.037 °C/m
T at the top and bottom of the domain	4.68 °C and 13.88 °C, respectively
Initial S_H	Figures 2, 3 and 4
Gas composition	100% CH_4
Intrinsic permeability k, all units	Figures 2, 3 and 4
Porosity ϕ, all units	Figures 2, 3 and 4
Grain density ρ_R (all formations)	2700 kg/m^3 (all media)
Specific heat	835 J/kg/K (Units B,C,D), 1000 J/kg/k elsewhere
Wet thermal conductivity ($k_{\Theta RW}$)	3.8 W/m/K (all formations)
Wet thermal conductivity ($k_{\Theta RD}$) (all formations)	(1-ϕ) $k_{\Theta RW}$ (all formations)
Composite thermal conductivity model[29,53]	$k_{\Theta C} = k_{\Theta RD} + (S_A^{1/2} + S_H^{1/2})\,(k_{\Theta RW} - k_{\Theta RD}) + \phi\, S_I\, k_{\Theta I}$
Capillary pressure model[44]	$P_{cap} = -P_0\left[\left(S^{*}\right)^{-1/\lambda} - 1\right]^{-\lambda}$ $\quad S^{*} = \frac{(S_A - S_{irA})}{(S_{mxA} - S_{irA})}$
λ	0.45 (Units B,C,D); 0.15 (all other media)
P_0	10^4 Pa (Units B,C,D); 10^5 Pa (all other media)
Relative permeability model – EPM[28]	$k_{rA} = (S_A^*)^n$ $k_{rG} = (S_G^*)^m$ $S_A^* = (S_A - S_{irA})/(1 - S_{irA})$ $S_G^* = (S_G - S_{irG})/(1 - S_{irA})$
n; $m = n\text{-}0.5*Max(0.0,n\text{-}2)$	Figures 3, 4 and 5 Analogs for interlayers and underburden
S_{irG}	0.01 (all units)
S_{irA}	Figures 3 and 4

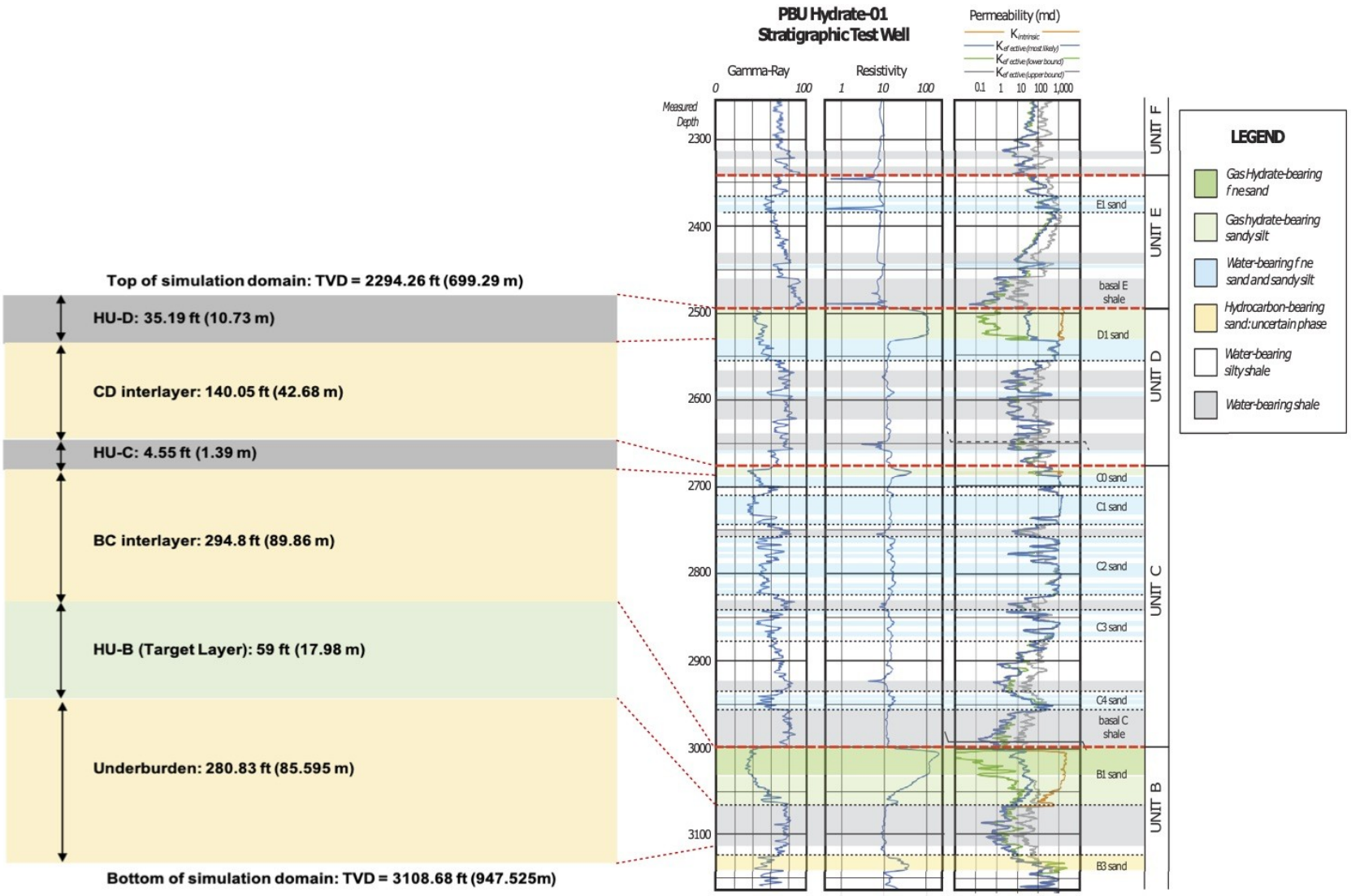

Figure 1. Description of the domain (not to scale) used in the simulation of the long-term field test gas production from the hydrate accumulations on the North Slope of Alaska geology, and of its relationship to the geology, minerology and stratigraphy at the site. The hydrate-bearing layers of the B1 Sand (Unit B), C0 Sand (Unit C) and D1 Sand (Units D) are referred to as HU-B, HU-C and HU-D,

respectively

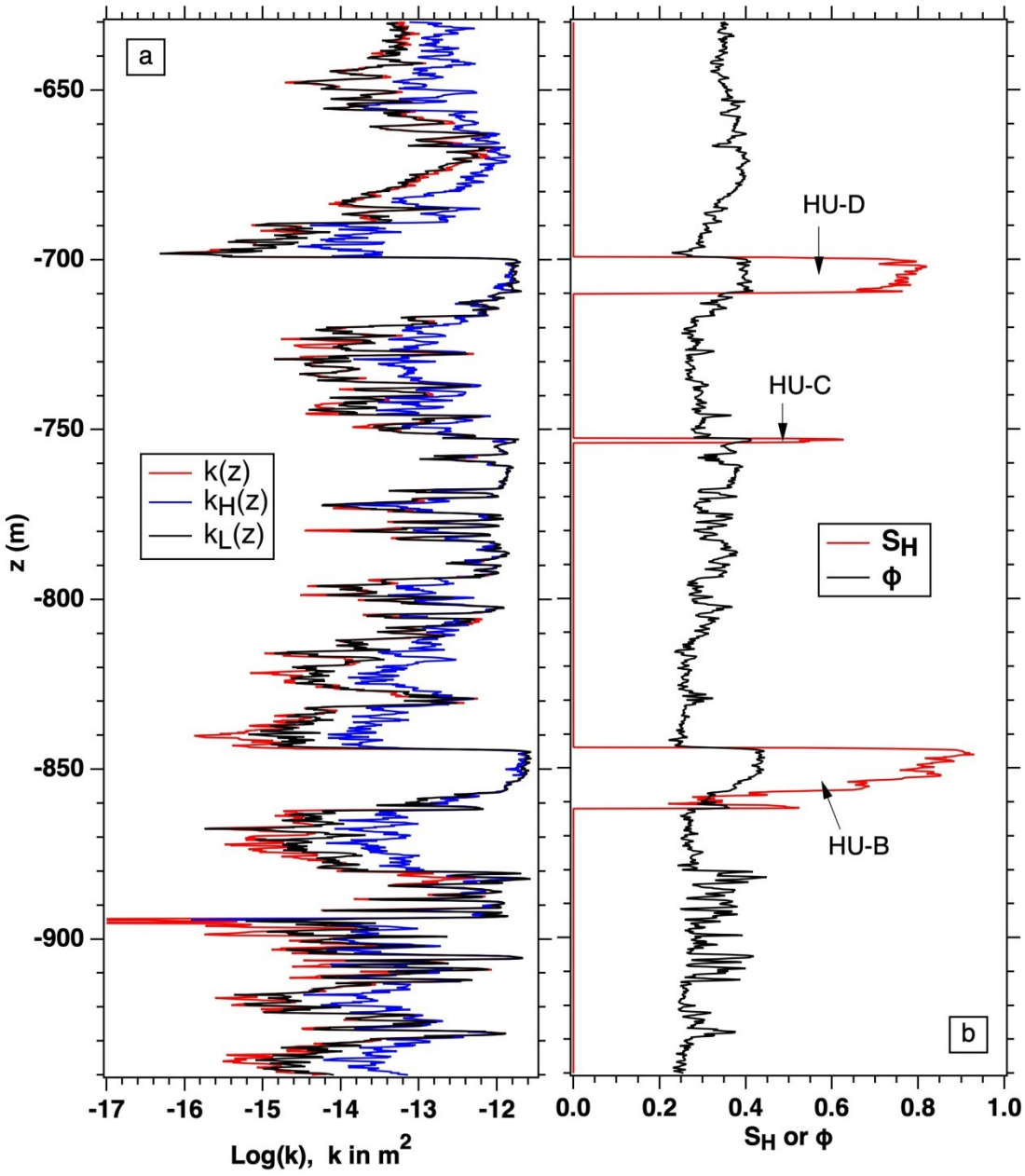

Figure 2. Spatial distribution of key properties and conditions in the profile of the test site: (a) the three estimates $k_H(z)$, $k_L(z)$ and $k(z)$ of the intrinsic permeability variations with the elevation z based on the different interpretations (A, B and C, respectively) of the available data; (b) the corresponding variations of porosity $\phi(z)$ and hydrate saturation $S_H(z)$ in the subsurface profile. The three hydrate-bearing units are clearly identified by the occurrence of $S_H > 0$.

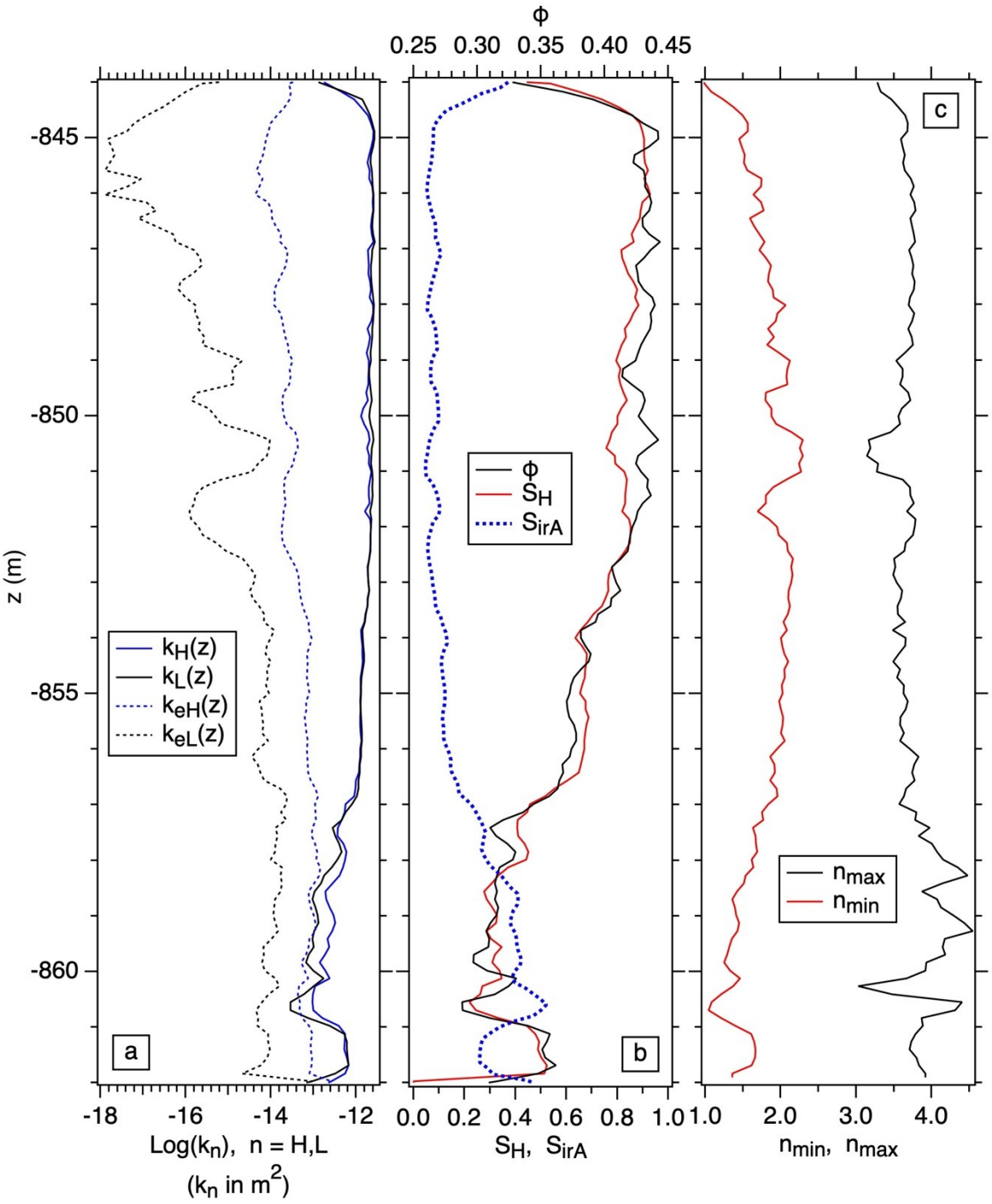

Figure 3. Data interpretation A and B in HU-B: variability with z (a) in the intrinsic permeabilities $k_H(z)$ and $k_L(z)$ and the corresponding effective permeabilities $k_{eH}(z)$ and $k_{eL}(z)$; (b) in the key flow properties ϕ and S_{irA} and in the initial S_H; and (c) in the relative permeability exponents n_{max} and n_{min} (corresponding to $k_{eL}(z)$ and $k_{eH}(z)$, respectively).

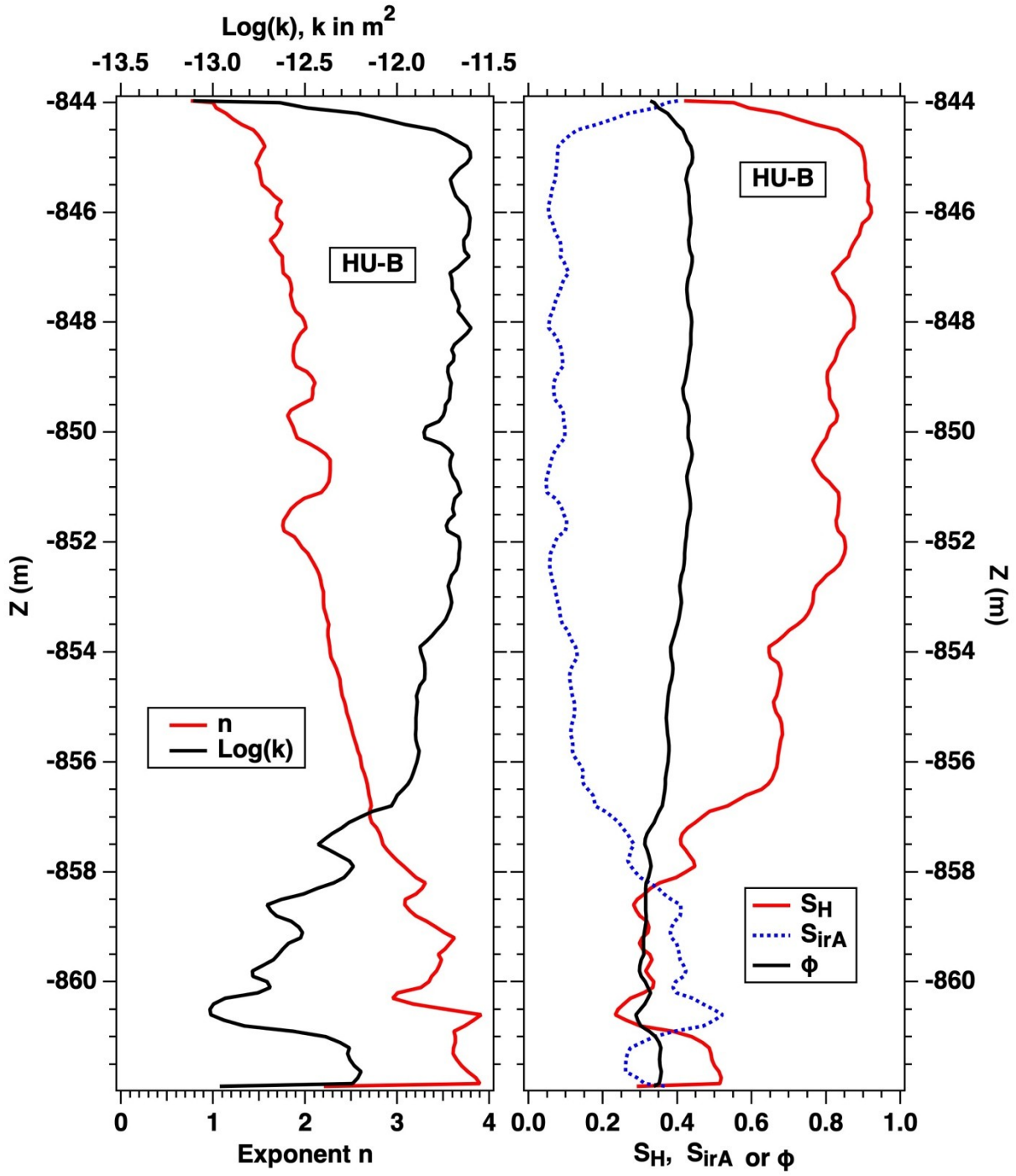

Figure 4. Data interpretation C in HU-B: variability with z in the relative permeability exponent n and in the intrinsic permeability k, and in ϕ, S_{irA} and S_H.

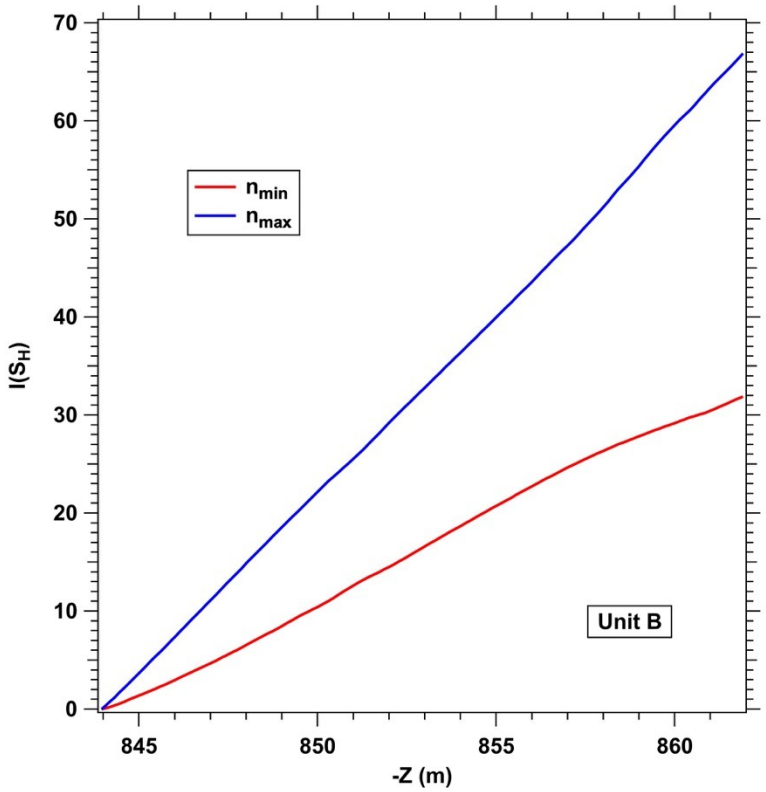

Figure 5. Numerical integration of n_{max} and n_{min} (corresponding to the data interpretations A and B) used for accurate assignment of the relative permeability exponents to the elements of the discretized domain in HU-B. Similar integrations were used for assignments to the elements of HU-C and HU-D.

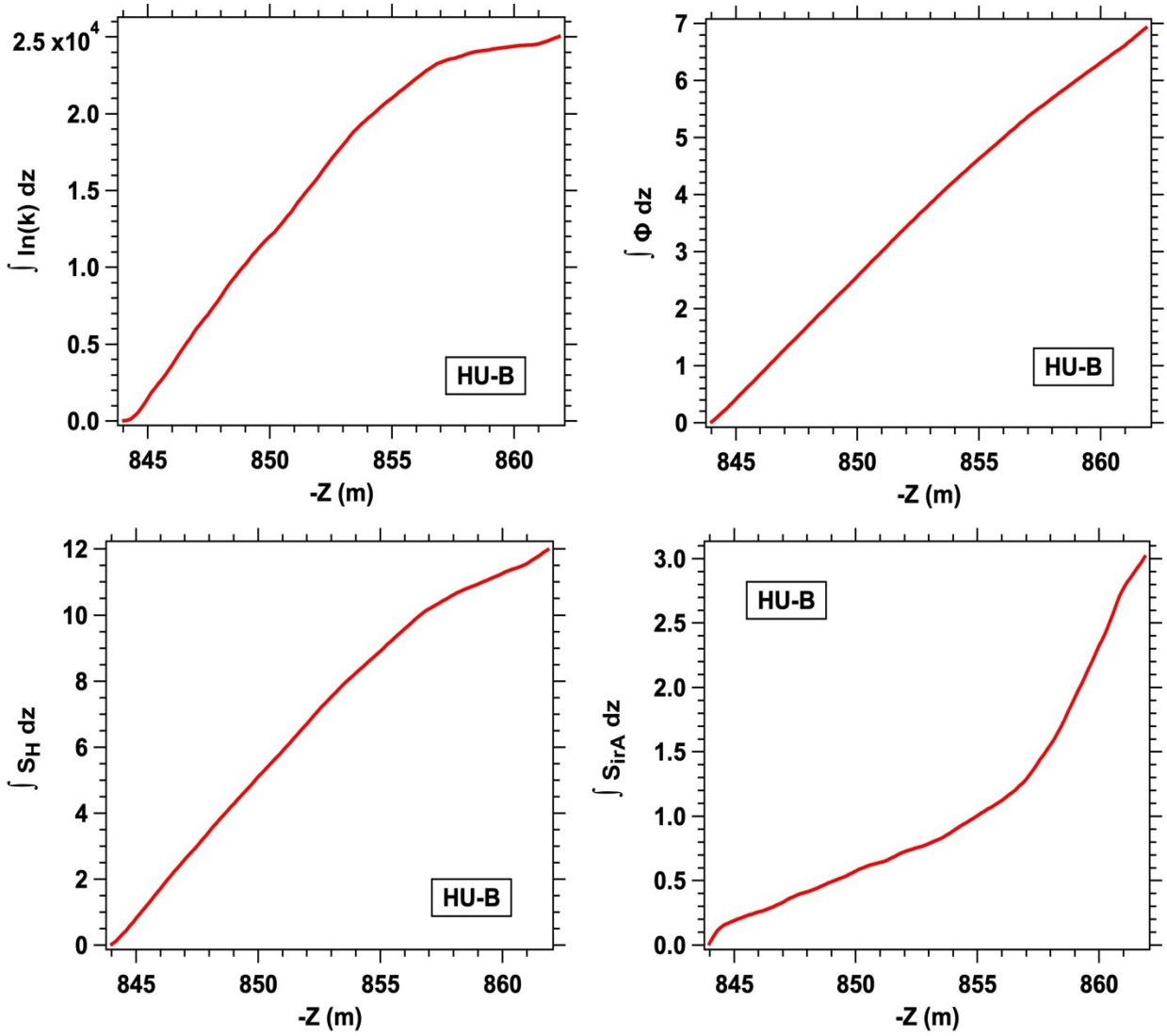

Figure 6. Numerical integration of key properties and conditions, used for accurate assignment to the elements of the discretized domain in HU-B. The exponent *n* was also integrated in the same way. Similar integrations were used for assignments to the elements of HU-C and HU-D.

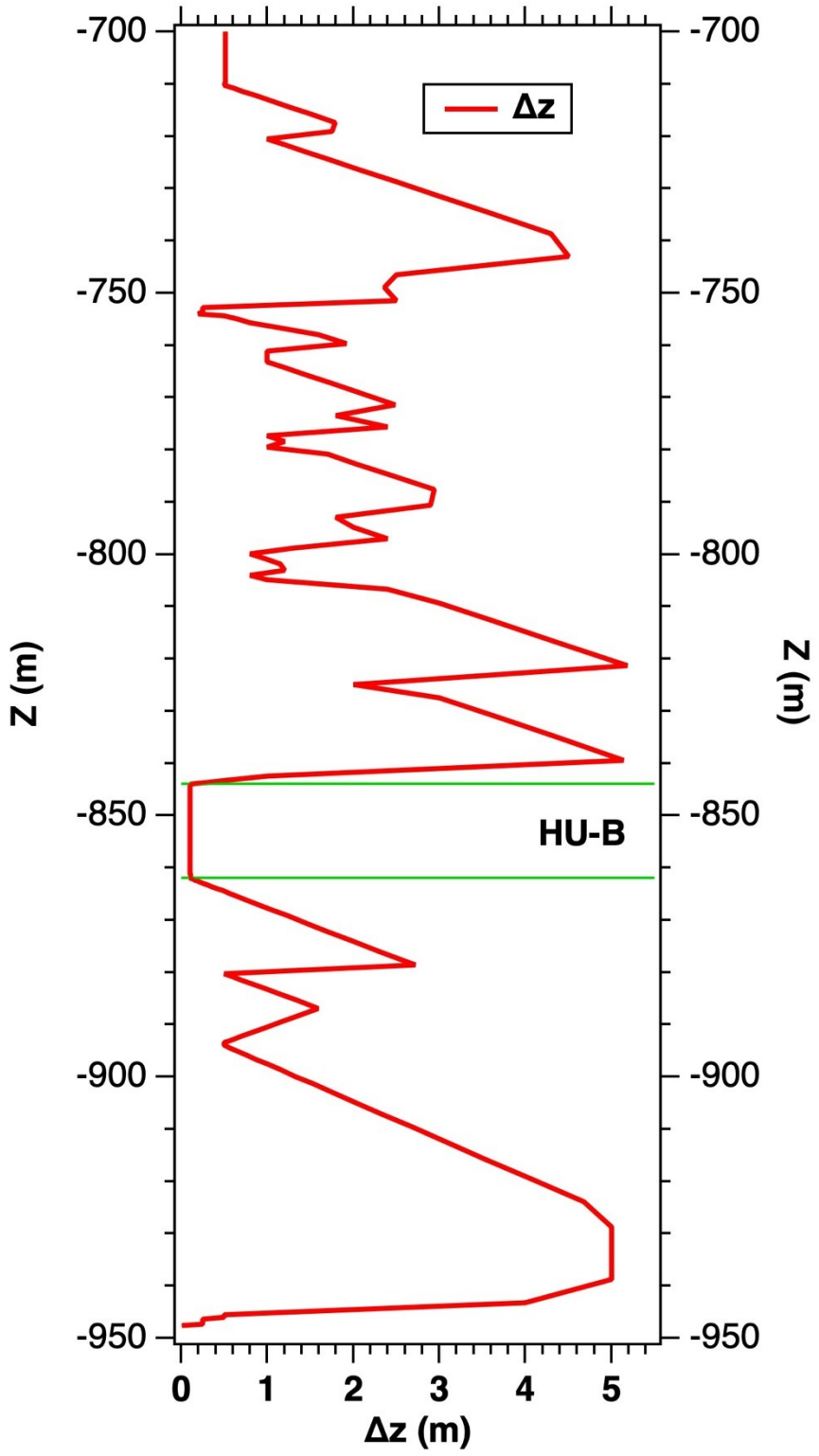

Figure 7. Non-uniform discretization $\Delta z(z)$ of the vertical dimension of the simulation domain. T he all-important dissociation target HU-B has the highest vertical resolution.

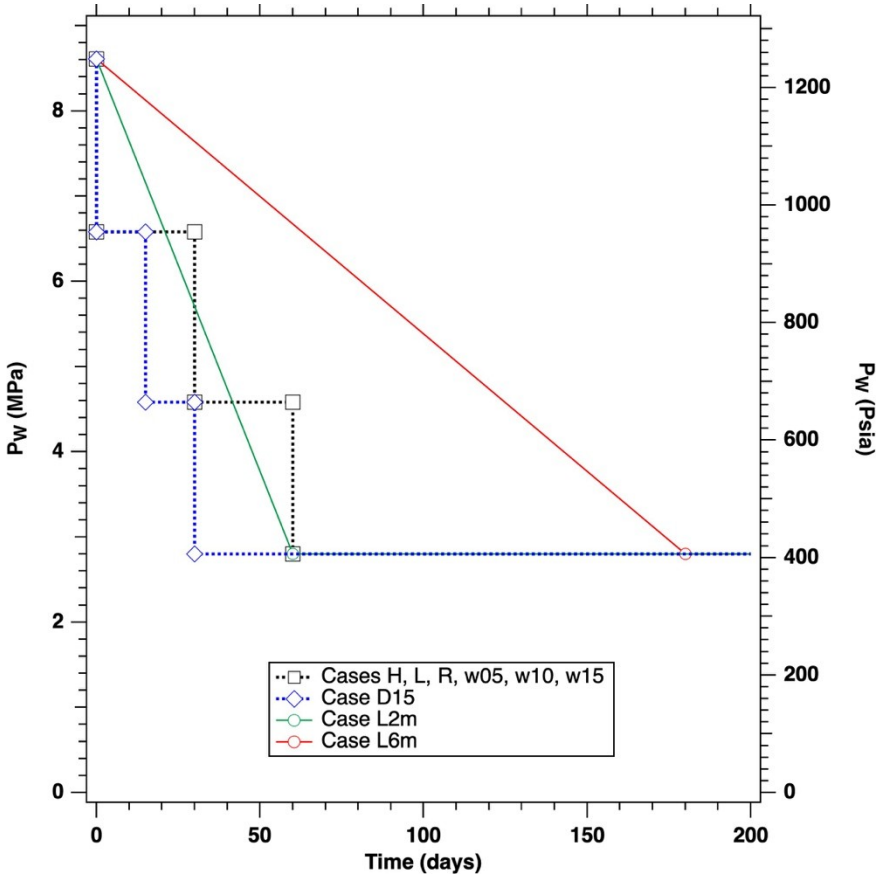

Figure 8. P_W schedules and shut-ins in all the investigated cases: Cases H, L, R, w05, w10, w15, L2m, L6m and D15. Note that Pw = 2.8 MPa remains constant in all these cases for t > 200 days.

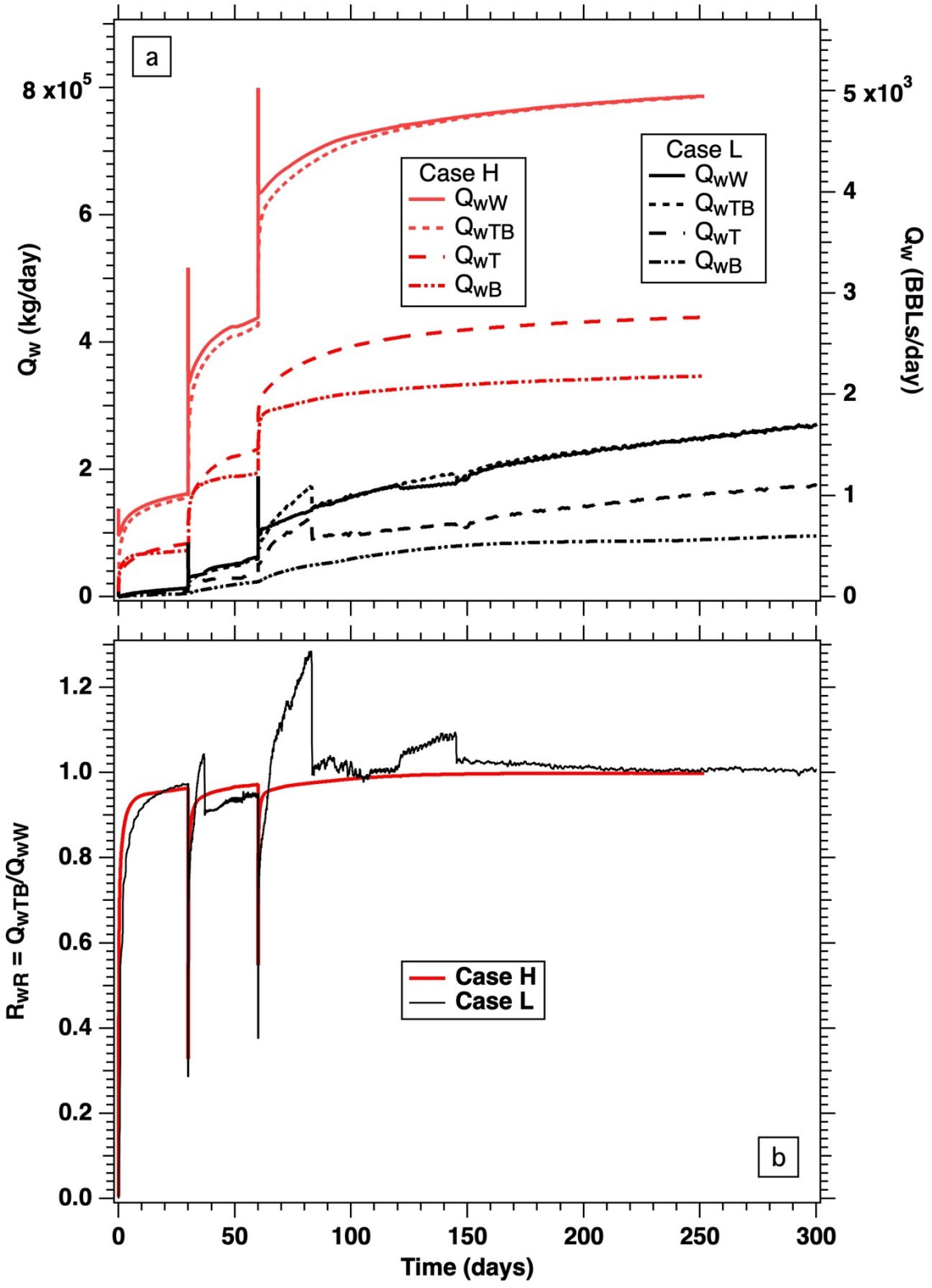

Figure 9. Cases H and L: Evolution of the (a) rate of water production at the well Q_{wW} and of its replenishment by water inflows through the top and bottom boundaries (Q_{wT} and Q_{wB},

respectively, and $Q_{wTB} = Q_{wTB} + Q_{wTB}$), and (b) the corresponding water replenishment ratio R_{wR}.

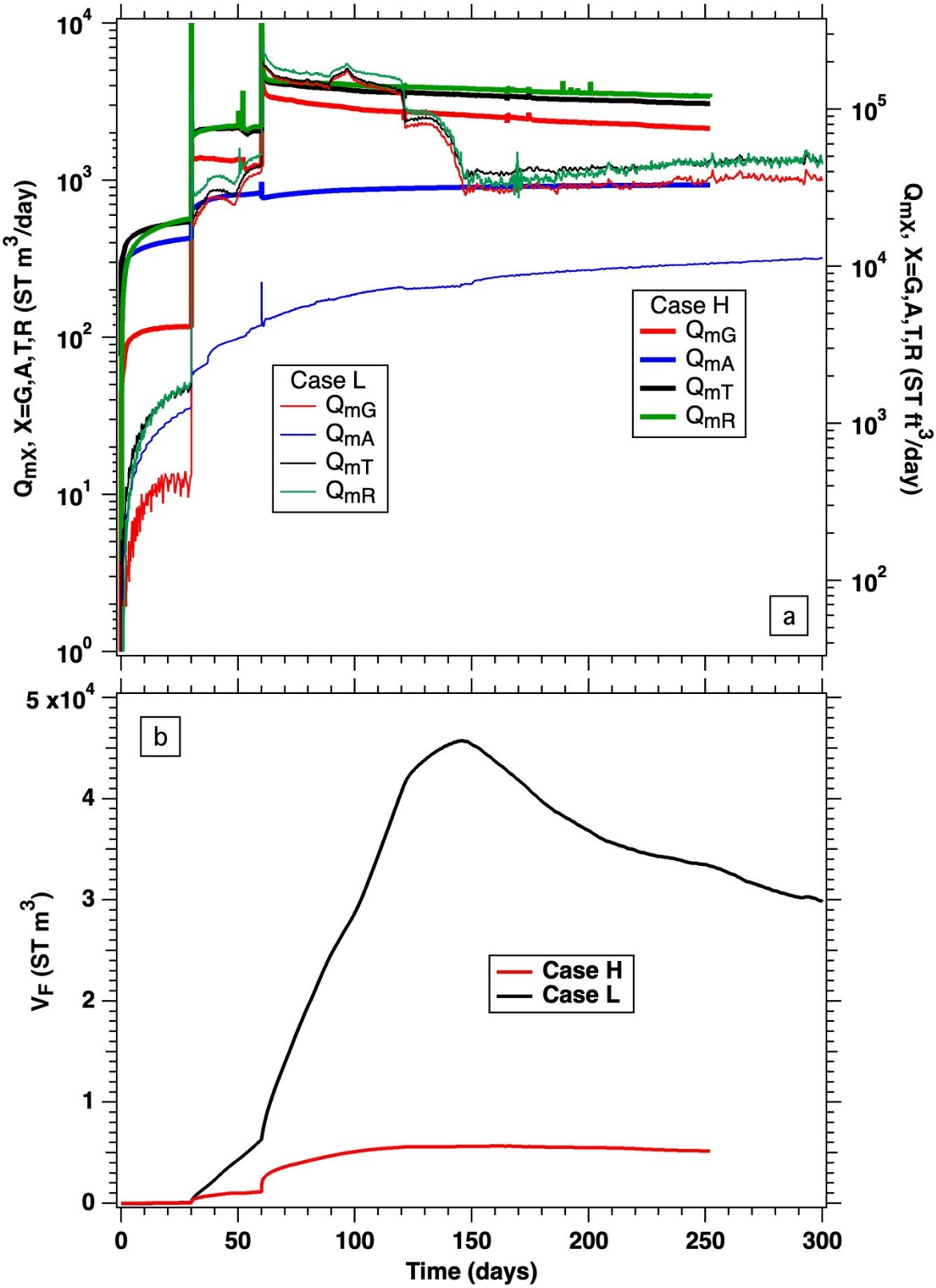

Figure 10. Cases H and L: Evolution of the (a) the volumetric rates Q_{mR}, Q_{mG}, Q_{mA} and Q_{mT}, and

(b) the corresponding volumes V_F of free CH_4 in the HU-B system.

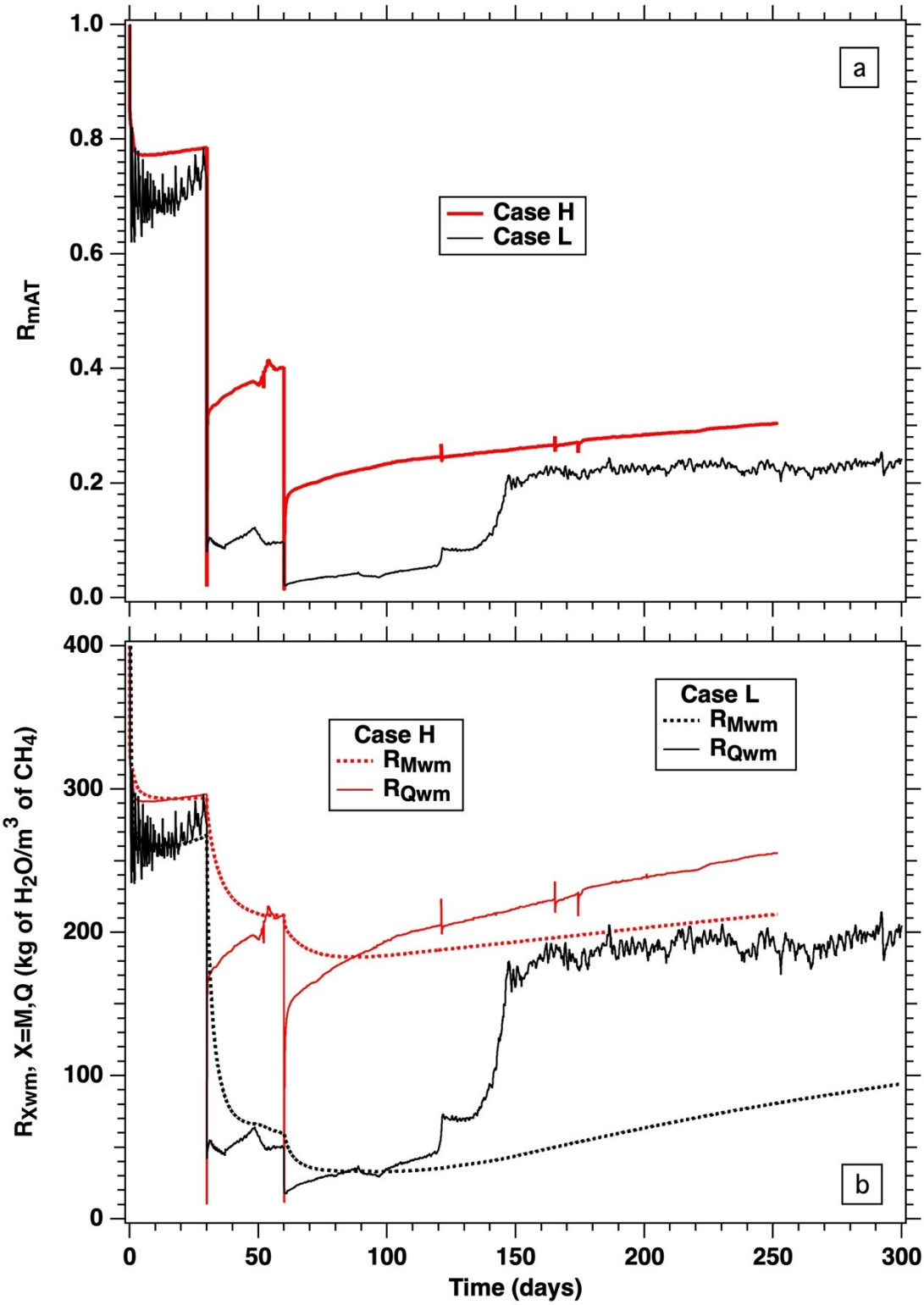

Figure 11. Cases H and L: Evolution of the (a) the aqueous CH_4 production fraction $R_{mAT} = Q_{mA}/Q_{mT}$, and (b) the corresponding instantaneous and cumulative water-to-gas ratio ($R_{Qwm} = Q_{wW}/Q_{gT}$

and $R_{Mwm} = M_{wW}/V_{mT}$, respectively).

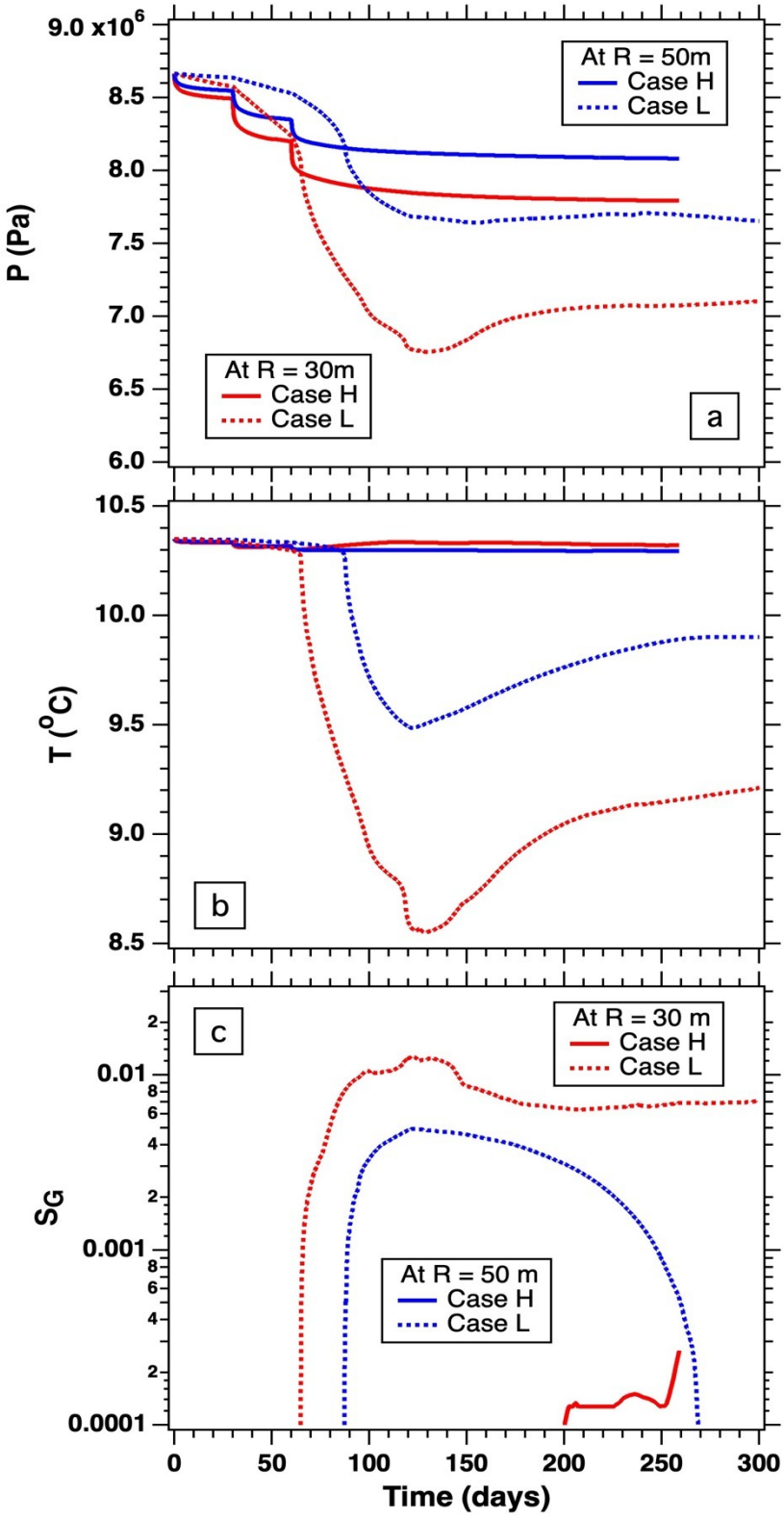

Figure 12. Cases H and L: Evolution of the (a) the pressure P , (b) the temperature T and (c) the pore volume-averaged gas saturation $\acute{S}_G$ at the observation wells during the production test. Note the minimal to negligible responses in Case H.

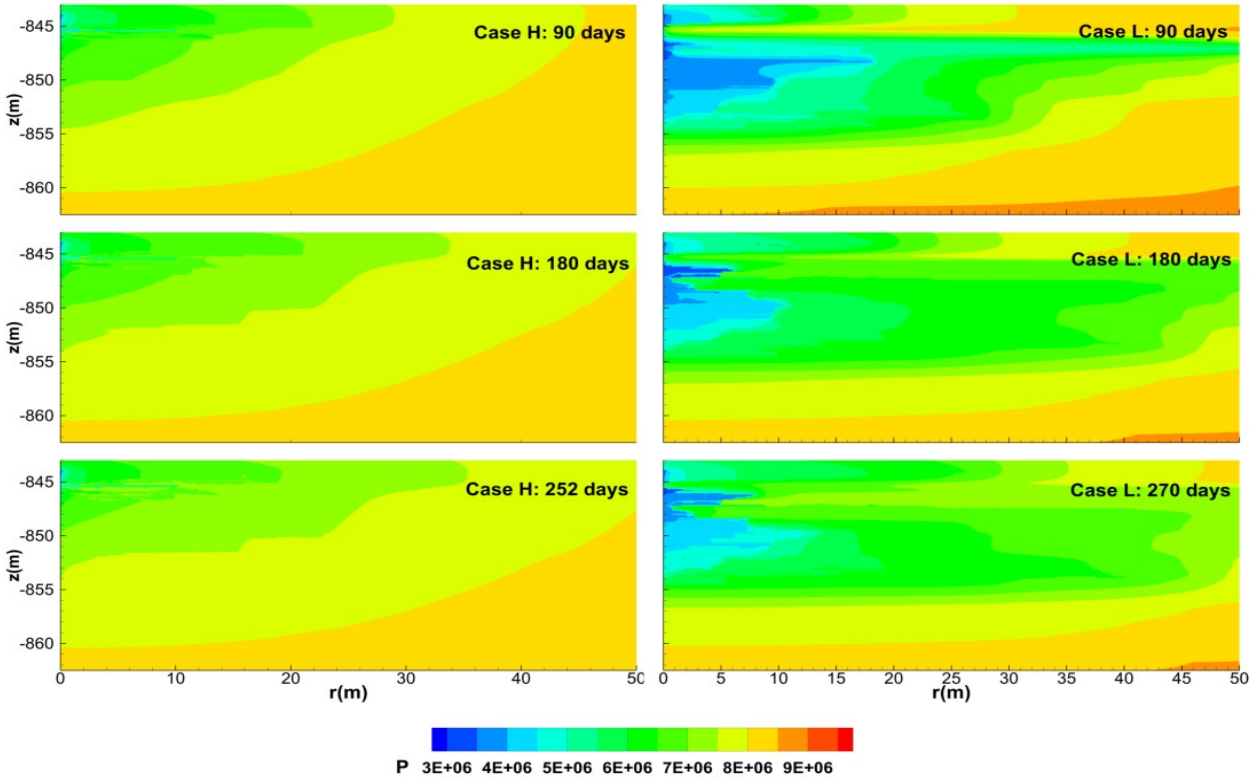

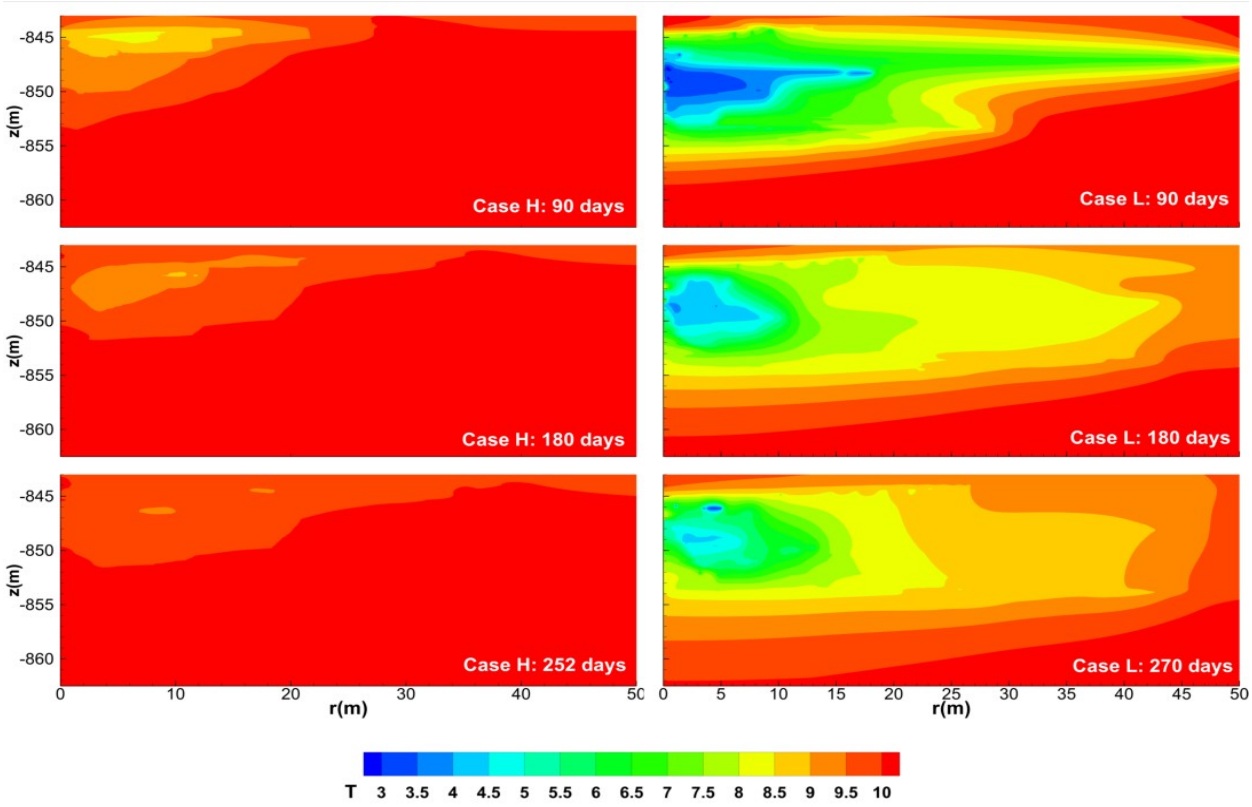

Figure 13. Evolution of the pressure P (top) and temperature T (bottom) distributions in the reservoir in the vicinity of the production well in Cases H (left) and L (right).

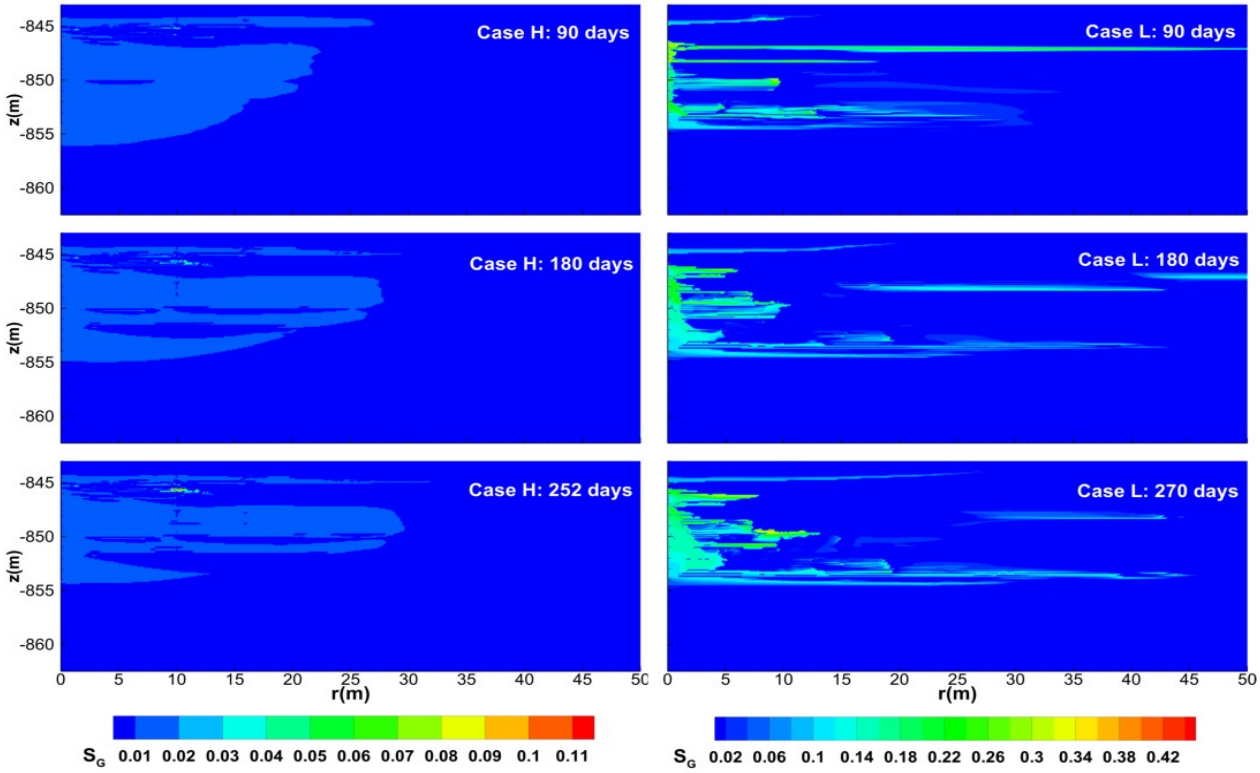

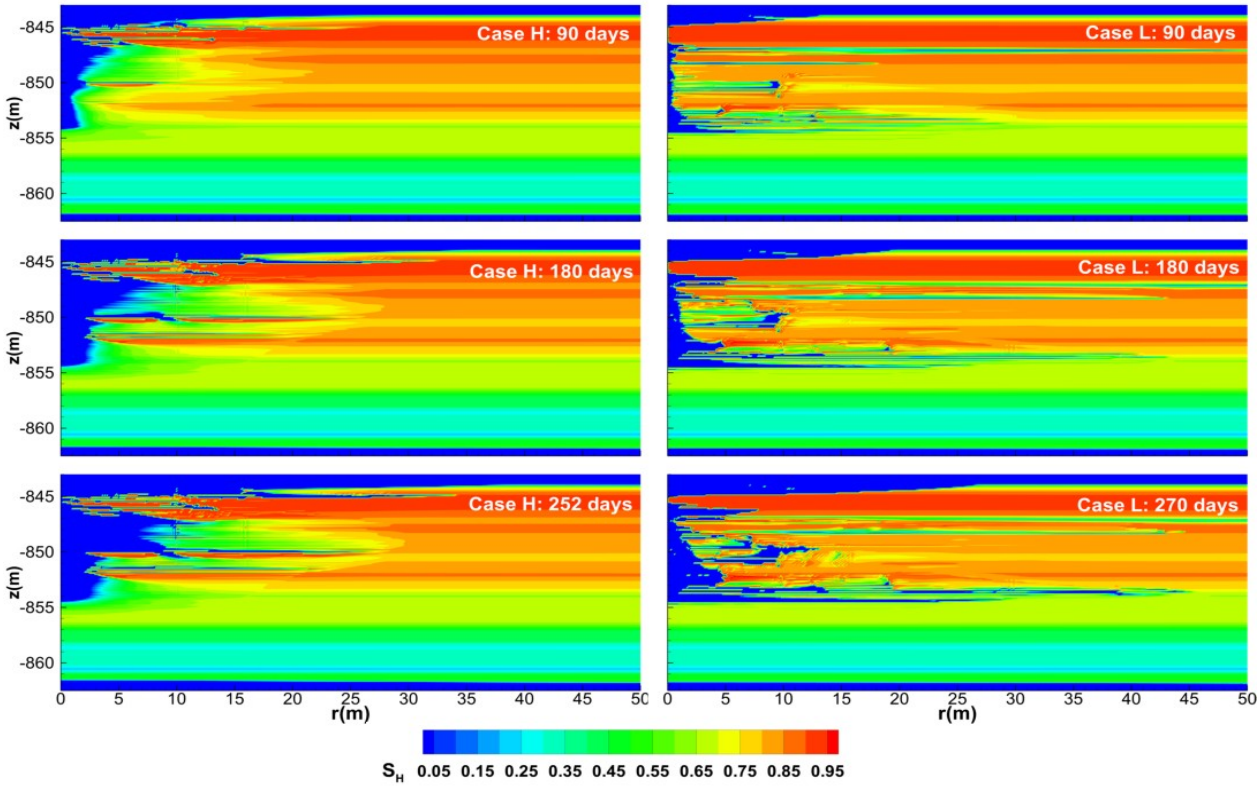

Figure 14. Evolution of the gas and hydrate saturation (S_G and S_H, top and bottom respectively) distributions near of the production well in Cases H (left) and L (right). Note the difference in the S_G scales in the two cases.

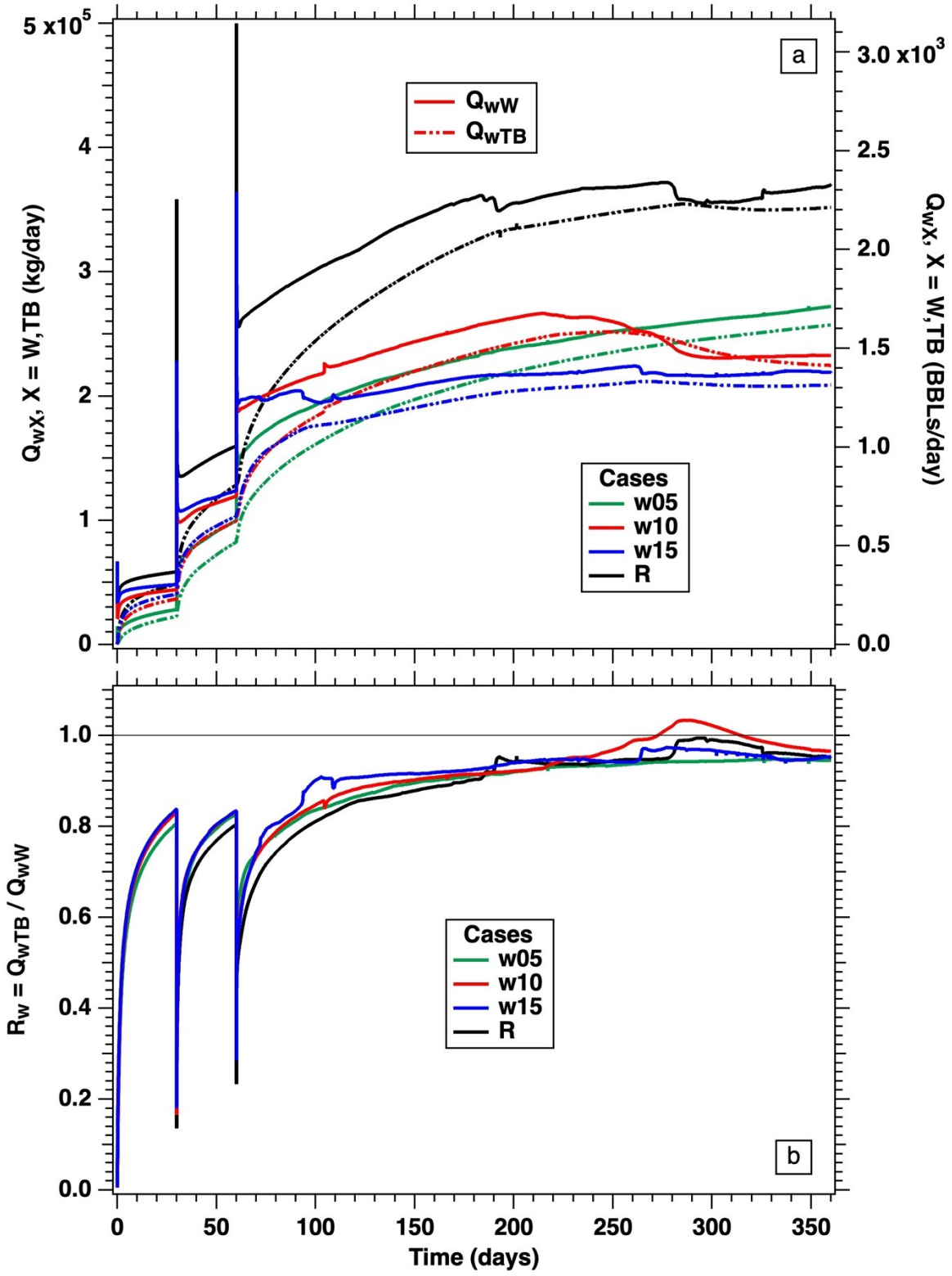

Figure 15. Cases w05, w10, w15 and R: Evolution of the (a) rate of water production at the well Q_{wW} and of its replenishment by water inflows through the boundaries Q_{wTB}, and (b) the corresponding water replenishment ratio R_{wR}.

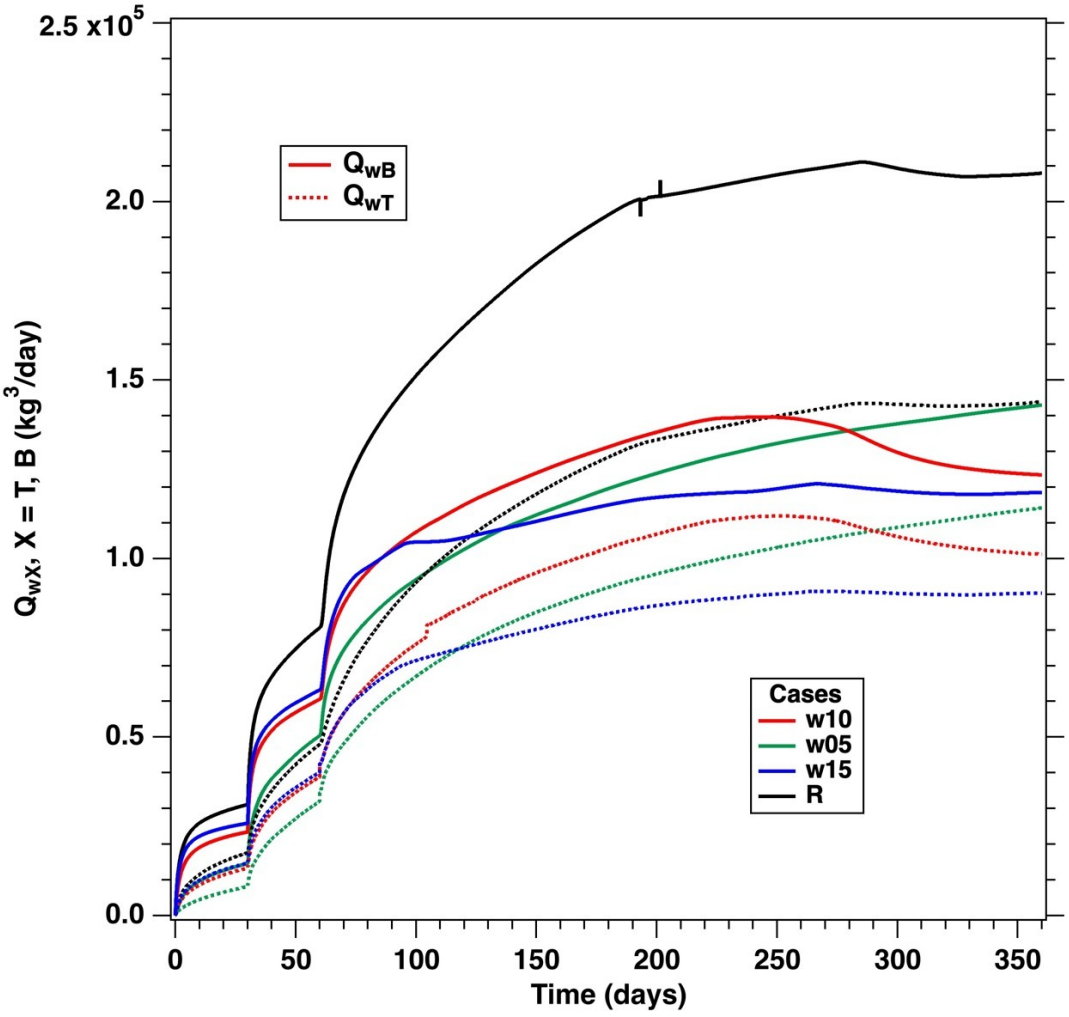

Figure 16. Provenance of the water inflows from the bottom and top boundaries (Q_{wB} and Q_{wT}, respectively) in Cases w05, w10, w15 and R. The Q_{wB} inflows are consistently dominant.

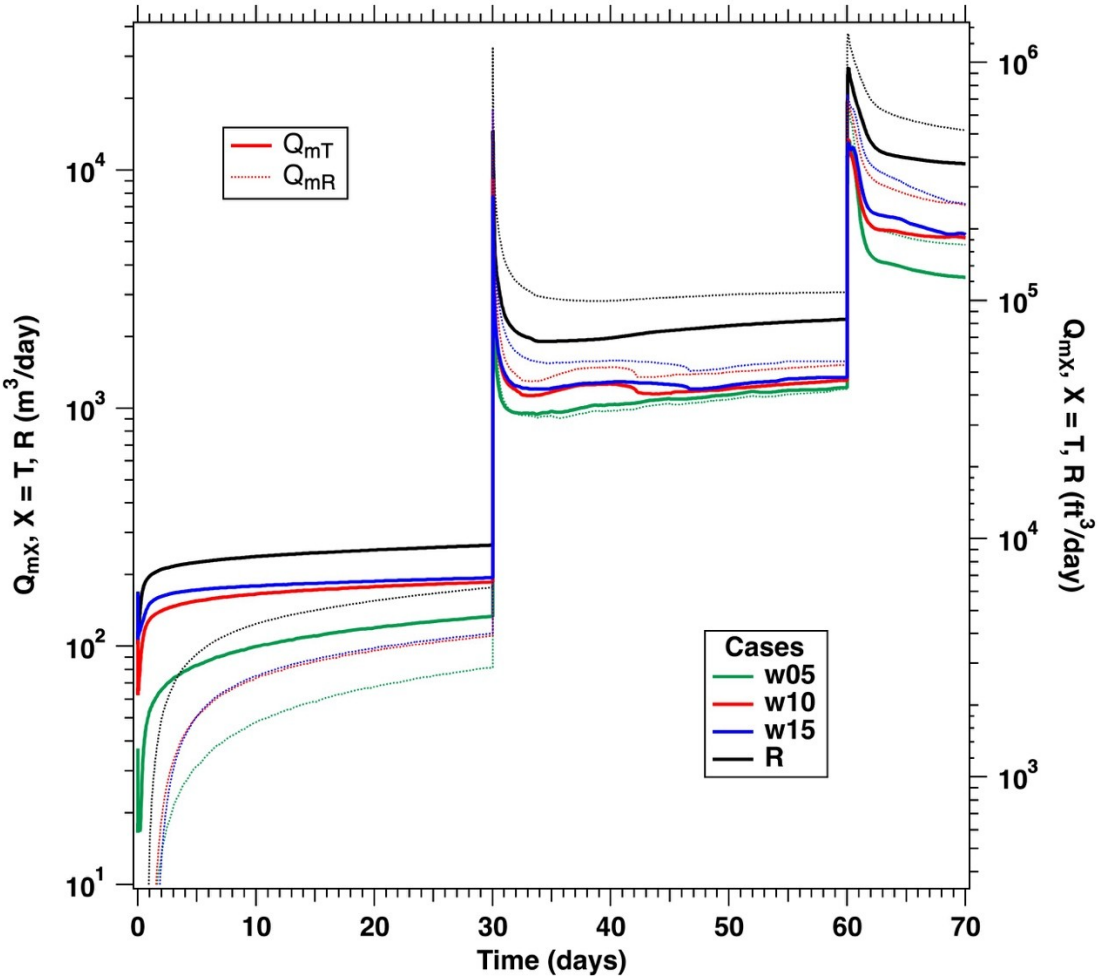

Figure 17. Evolution of the early rates of gas release from hydrate dissociation Q_{mR} and of total CH_4 production Q_{mT} in Cases w05, w10, w15 and R. The superiority of Case R is obvious.

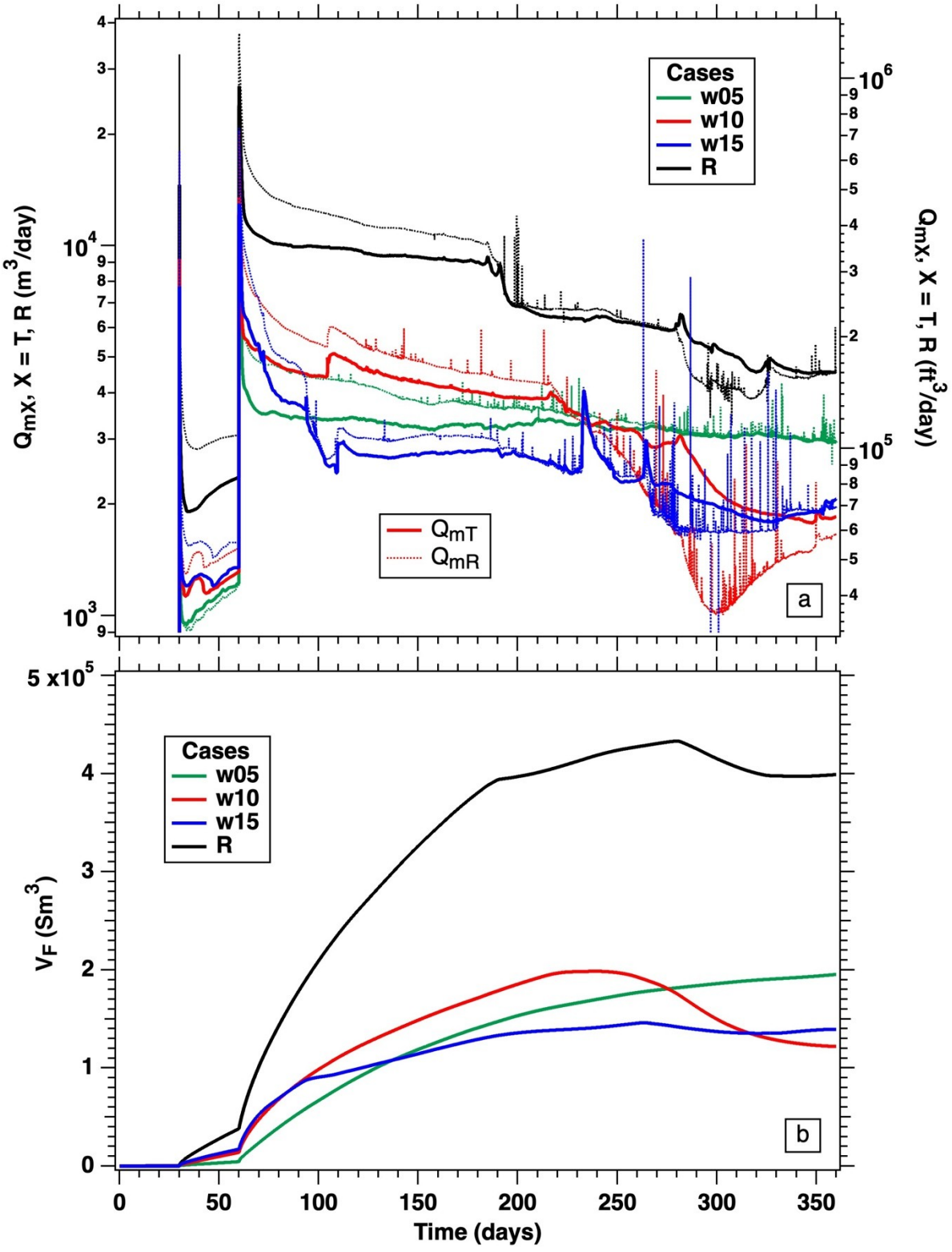

Figure 18. Cases w05, w10, w15 and R: Evolution of the (a) the volumetric rates Q_{mR} and Q_{mT}, and (b) the corresponding volumes V_F of free CH_4 in the HU-B system.

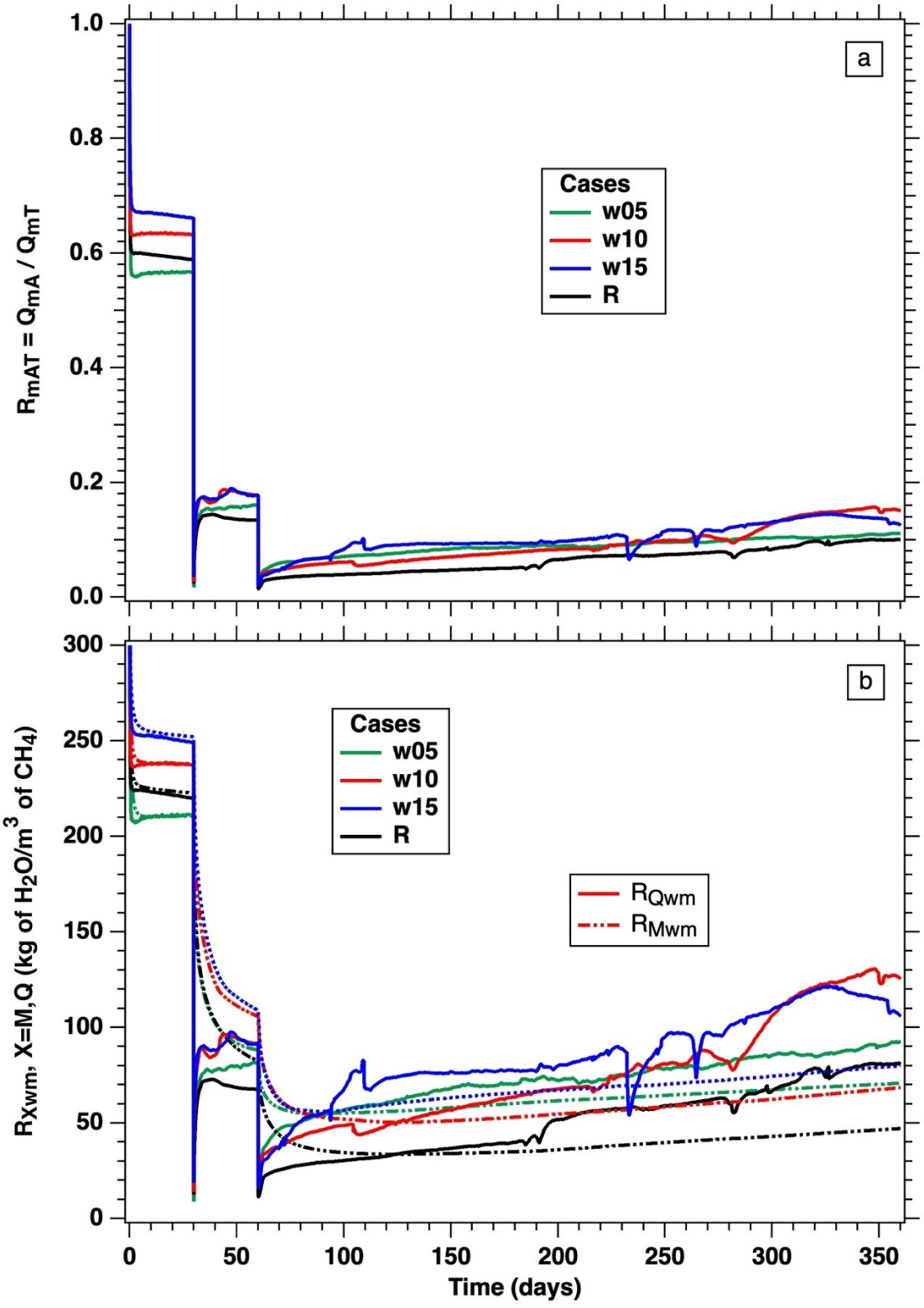

Figure 19. Cases w05, w10, w15 and R:: Evolution of the (a) the aqueous CH_4 production fraction $R_{mAT} = Q_{mA}/Q_{mT}$, and (b) the corresponding instantaneous and cumulative water-to-gas ratio ($R_{Qwm} = Q_{wW}/Q_{gT}$ and $R_{Mwm} = M_{wW}/V_{mT}$, respectively).

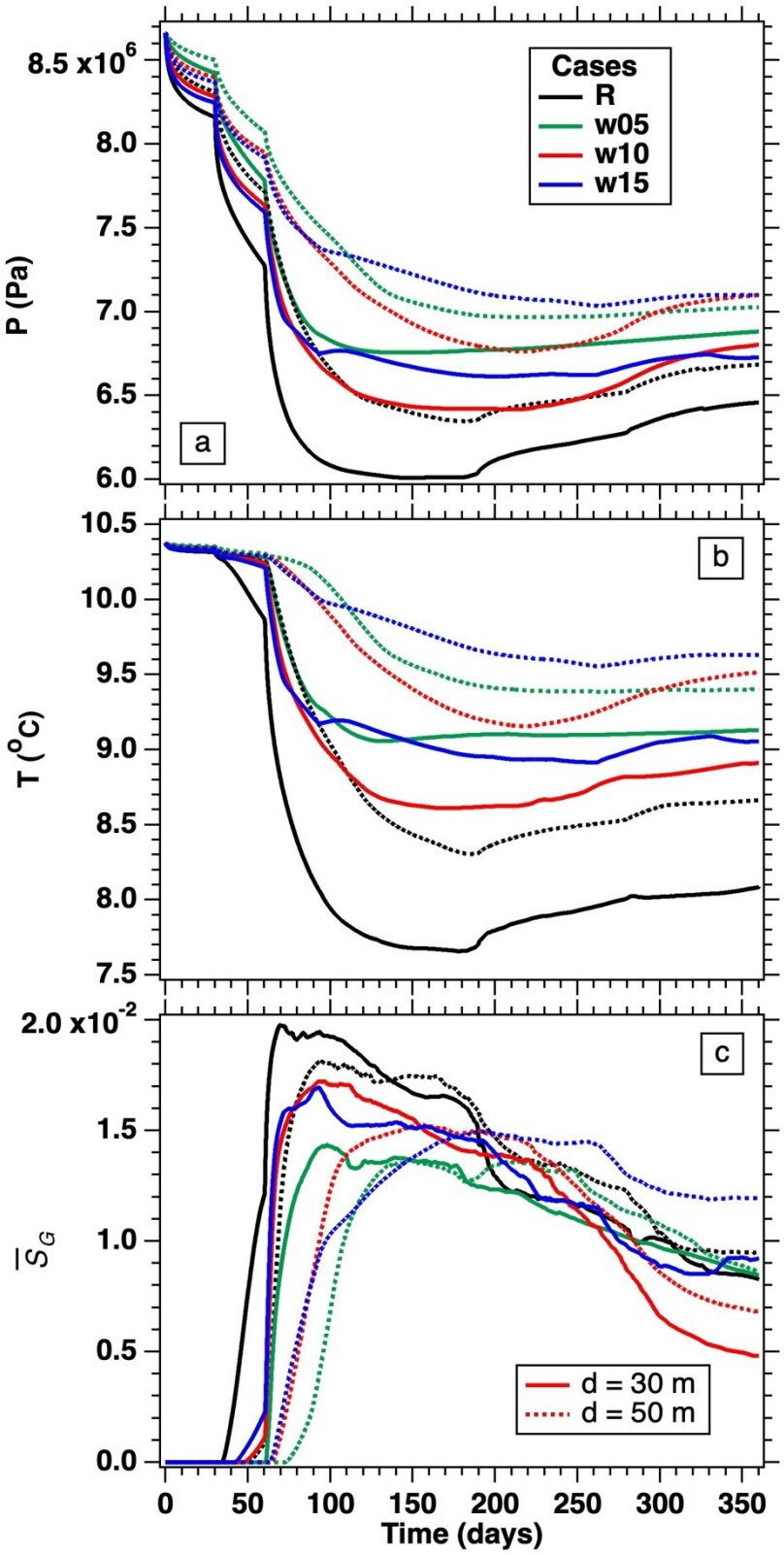

Figure 20. Evolution of (a) P, (b) T and (c) of the average gas saturation $\acute{S}_G$ at the observation wells during the production test in in Cases w05, w10, w15 and R.

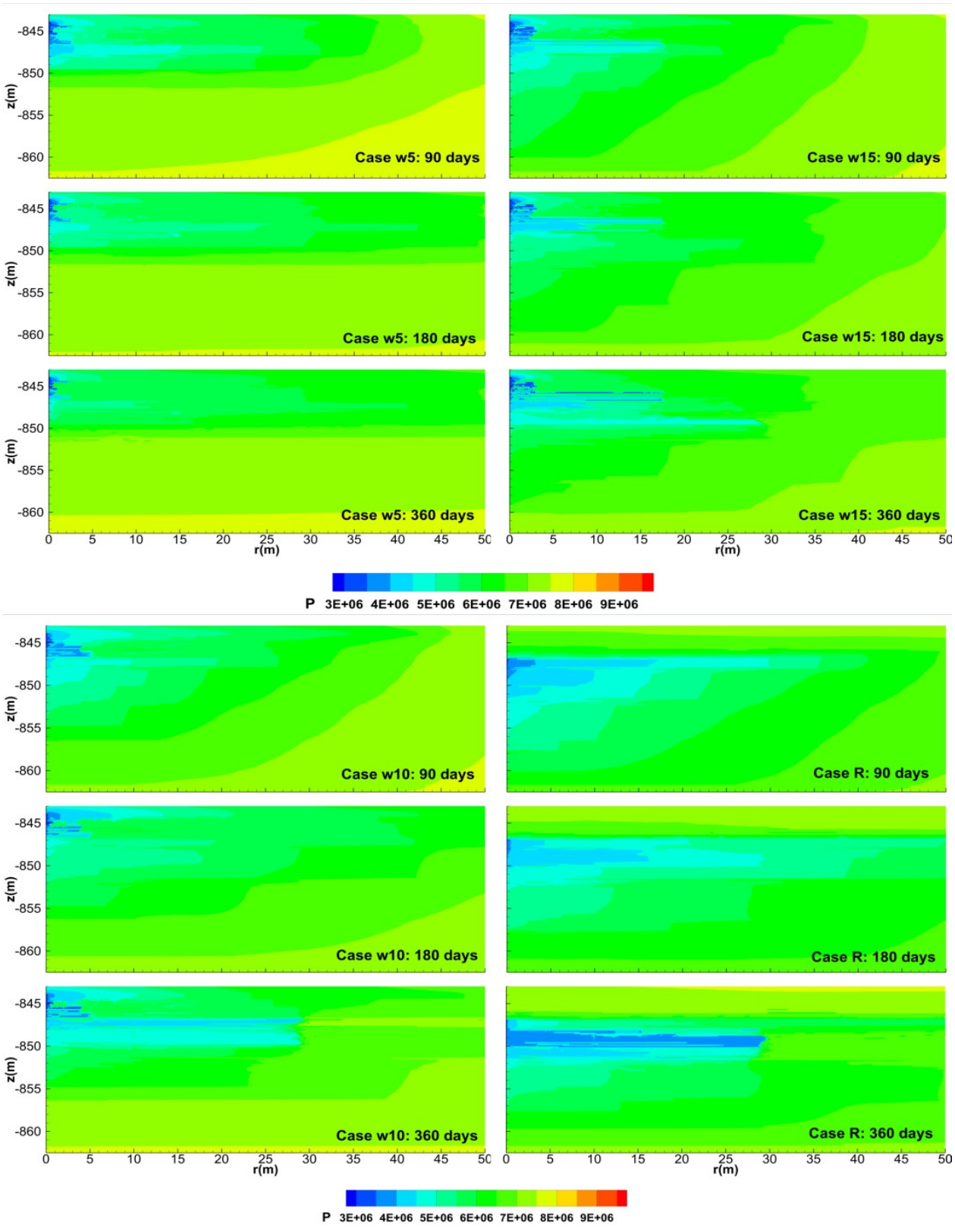

Figure 21. Evolution of the *P*-distributions in the reservoir in the vicinity of the production well

in Cases w05 and w15 (top) and Cases w10 and R (bottom).

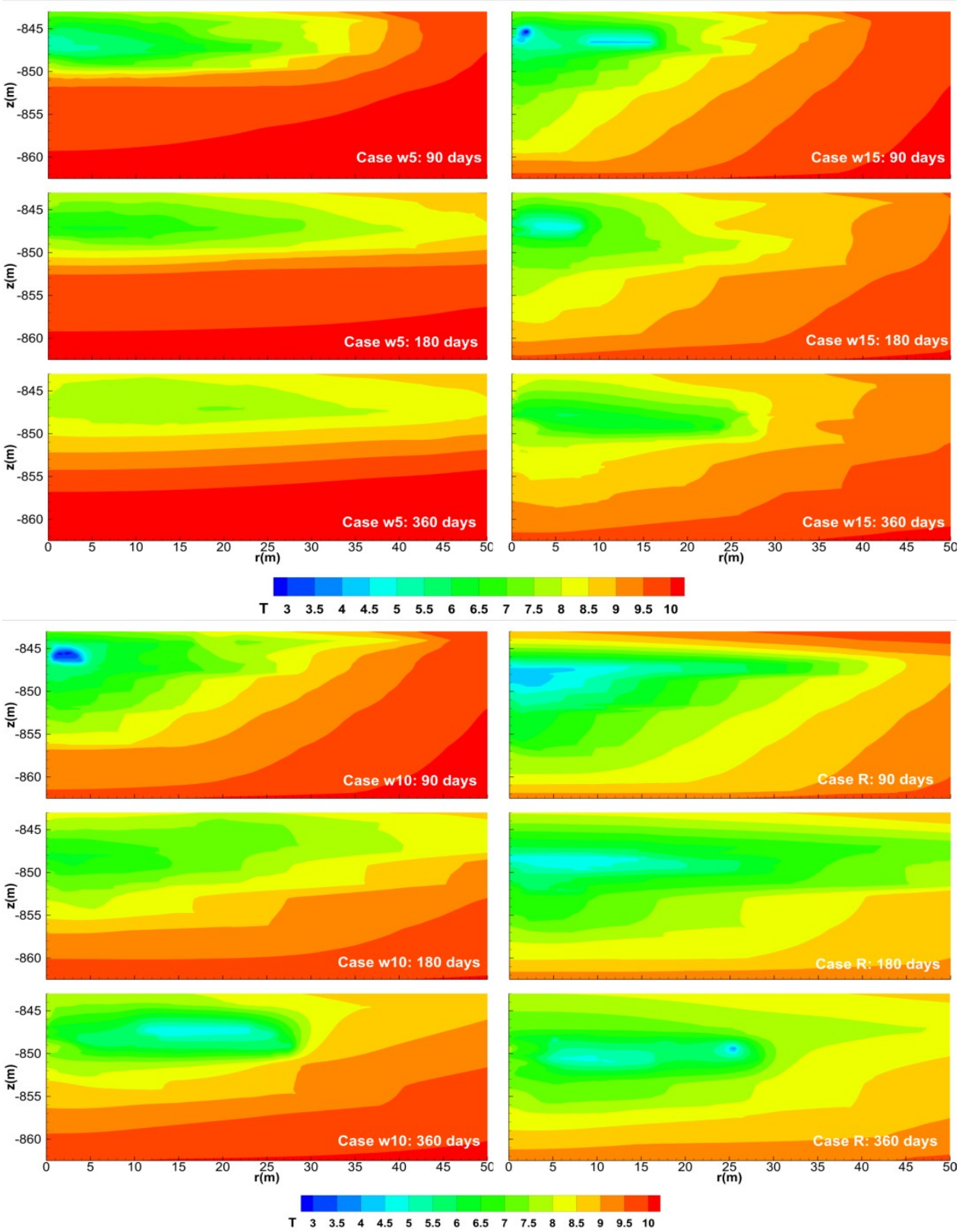

Figure 22. Evolution of the *T*-distributions in the reservoir in the vicinity of the production well

in Cases w05 and w15 (top) and Cases w10 and R (bottom).

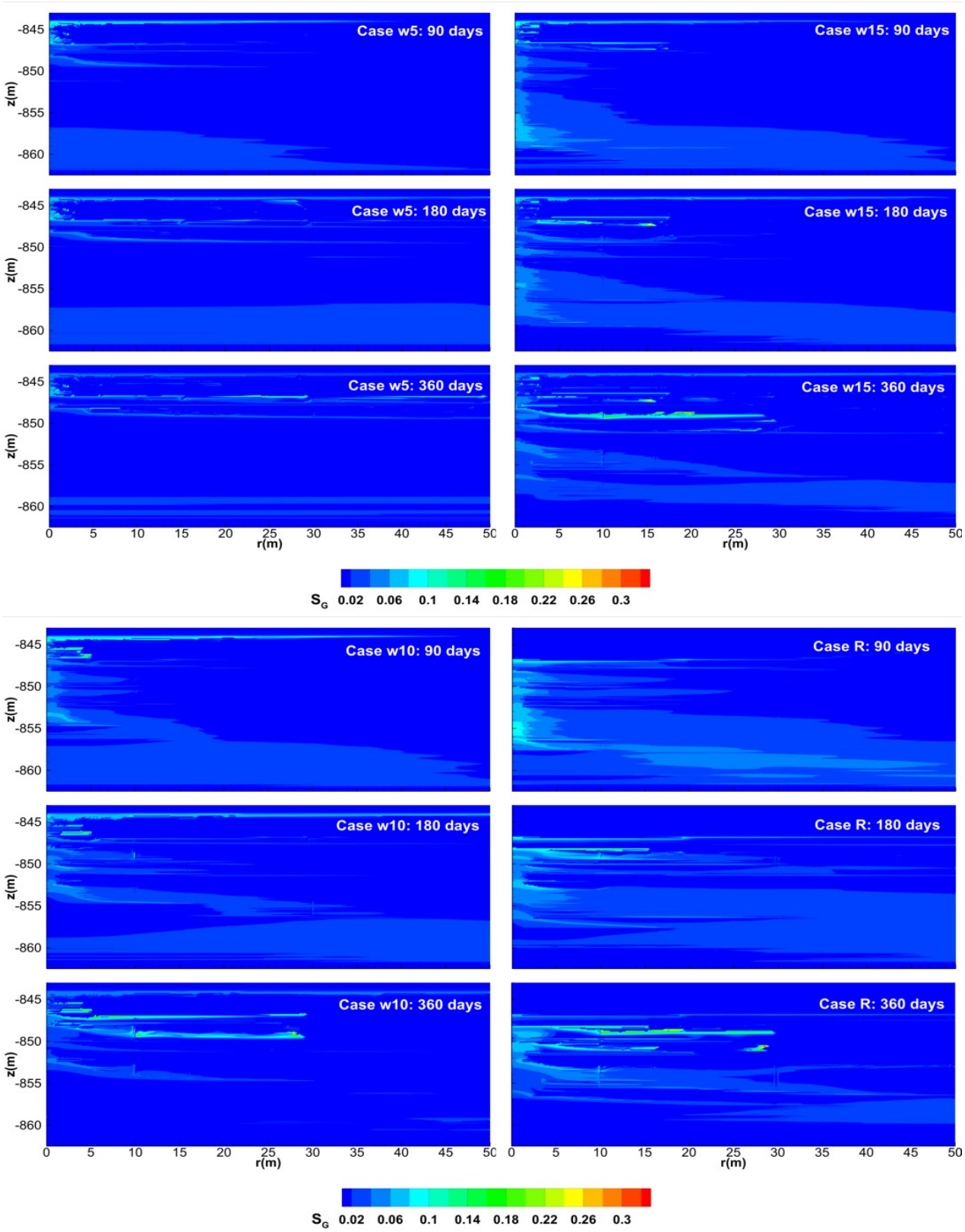

Figure 23. Evolution of the S_G-distributions in the reservoir in the vicinity of the production well

in Cases w05 and w15 (top) and Cases w10 and R (bottom).

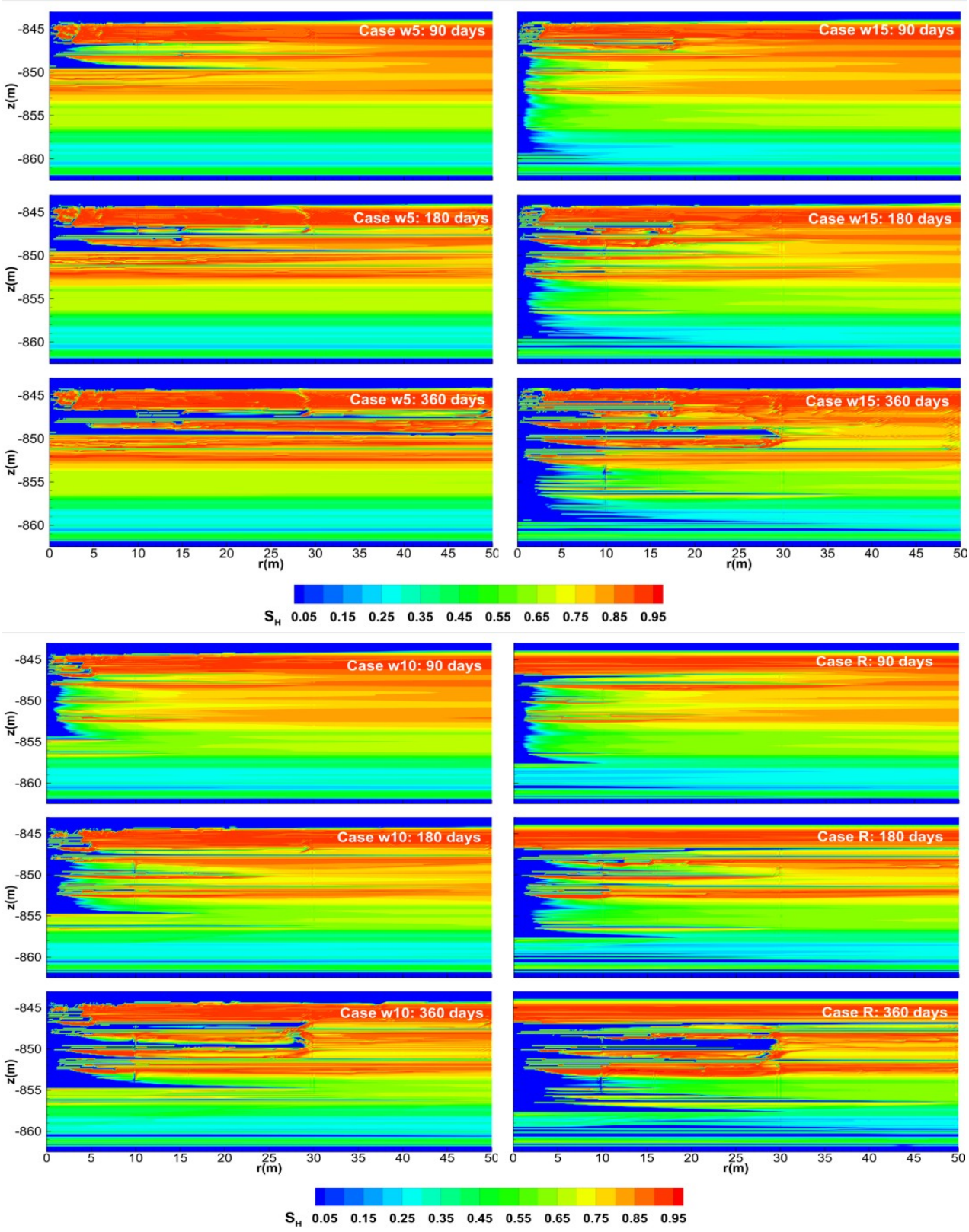

Figure 24. Evolution of the S_H-distributions in the reservoir near the production well in Cases

w05 and w15 (top) and Cases w10 and R (bottom).

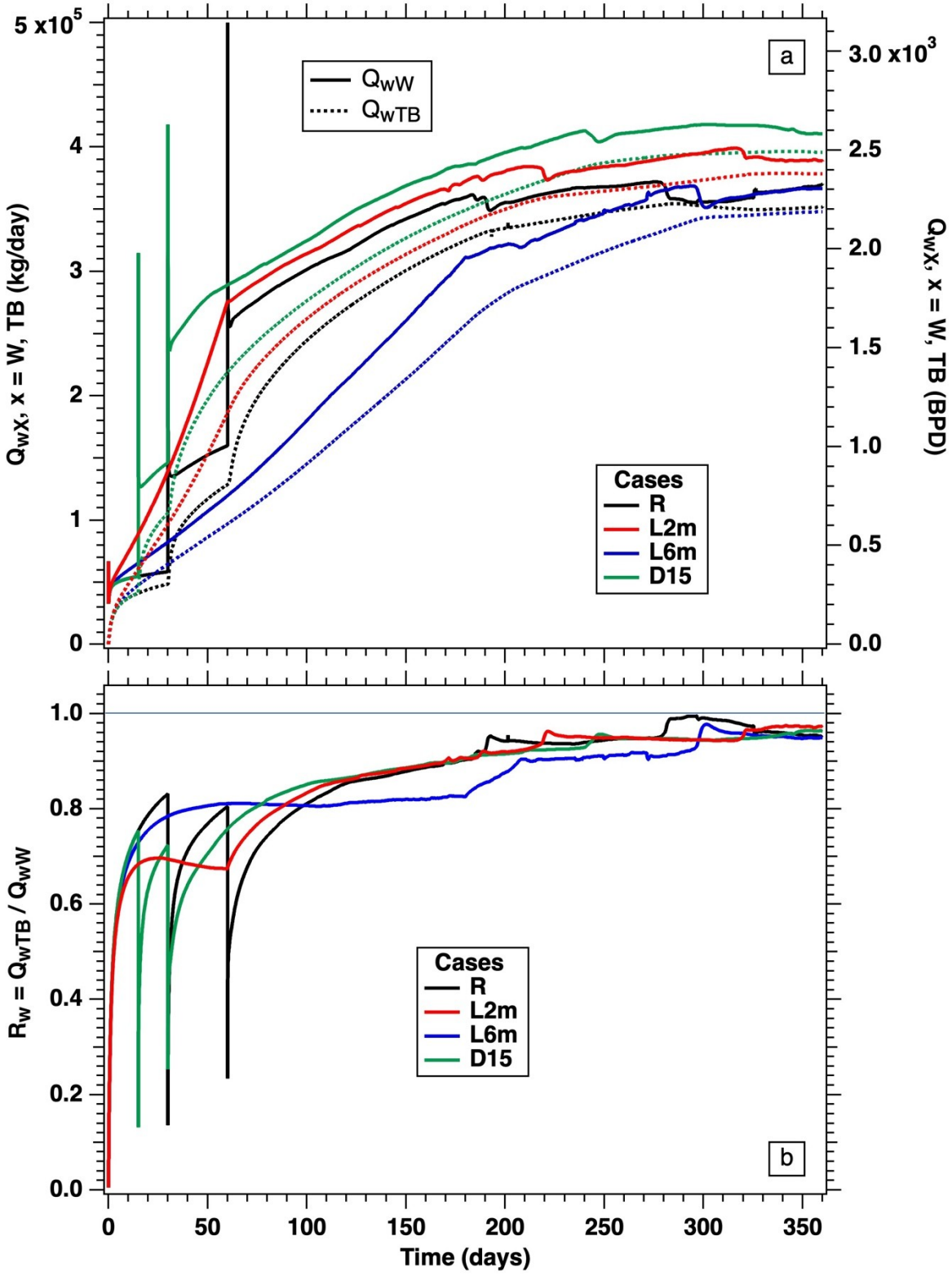

Figure 25. Cases R, L2m, L6m and D15: Evolution of the (a) rate of water production at the well Q_{wW} and of its replenishment by water inflows through the boundaries Q_{wTB}, and (b) the

corresponding water replenishment ratio R_{wR}.

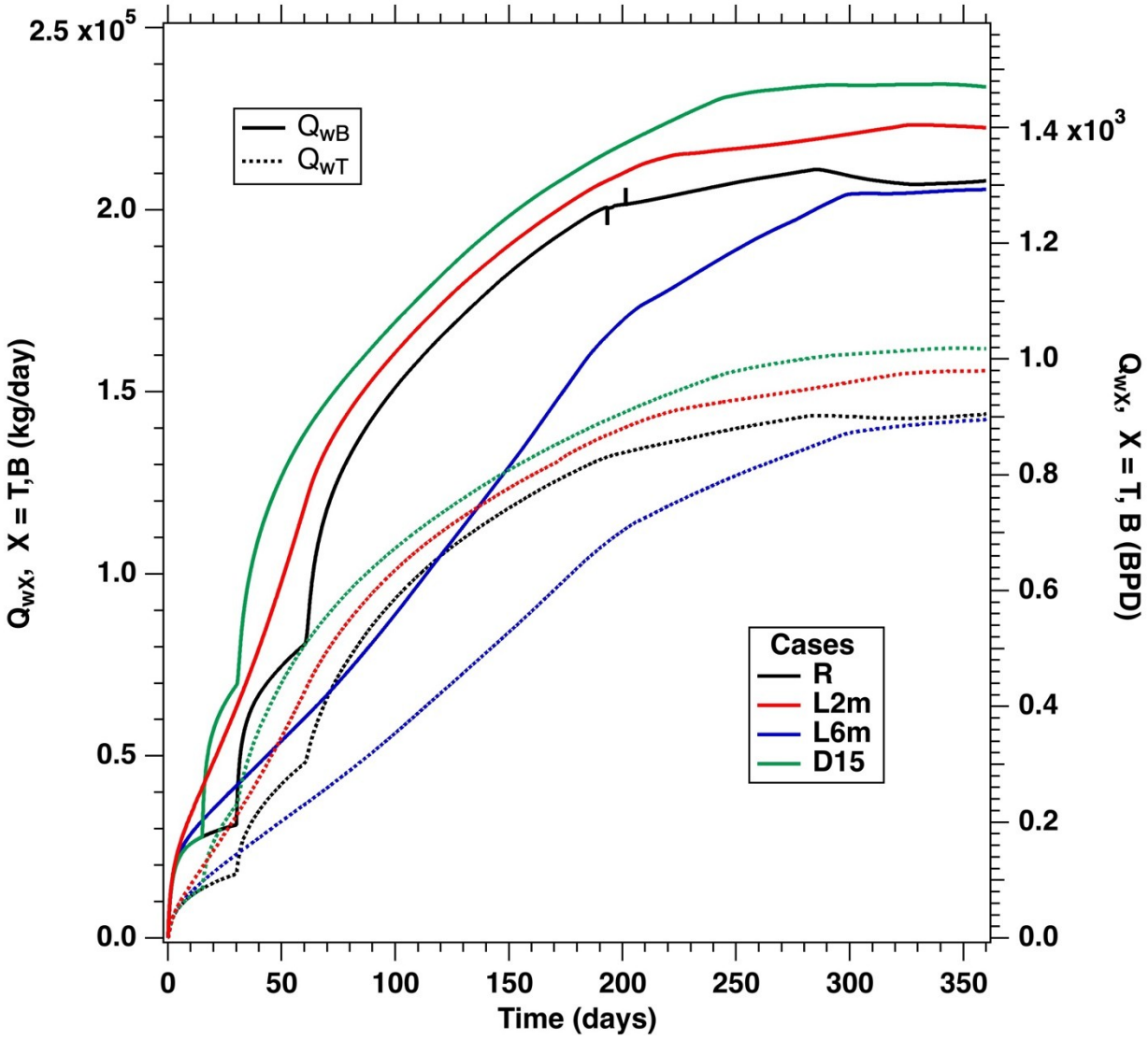

Figure 26. Provenance of the water inflows from the bottom and top boundaries (Q_{wB} and Q_{wT}, respectively) in Cases R, L2m, L6m and D15. The Q_{wB} inflows are consistently dominant.

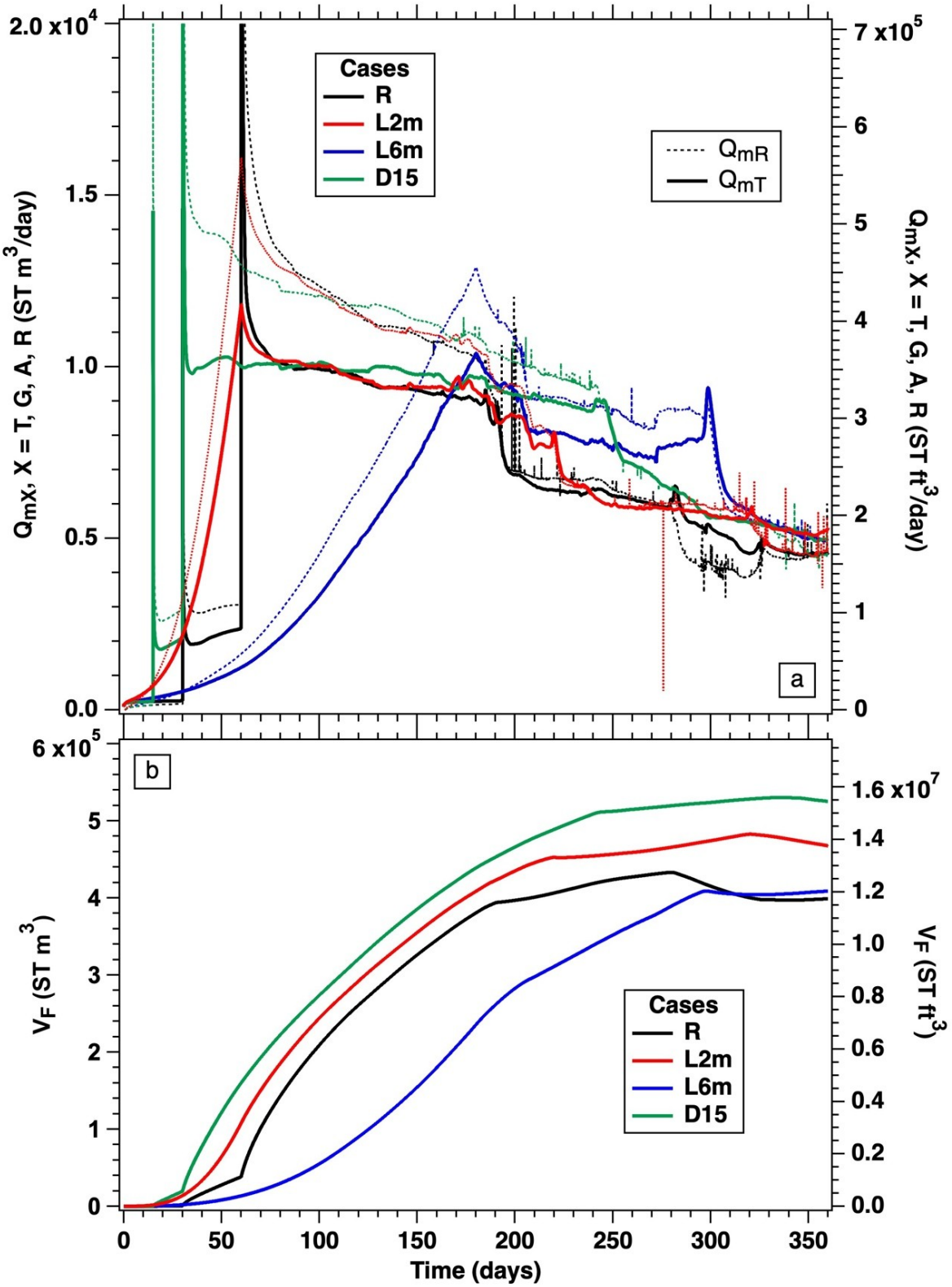

Figure 27. Cases R, L2m, L6m and D15: Evolution of the (a) the volumetric rates Q_{mR} and Q_{mT}, and (b) the corresponding volumes V_F of free CH_4 in the HU-B system.

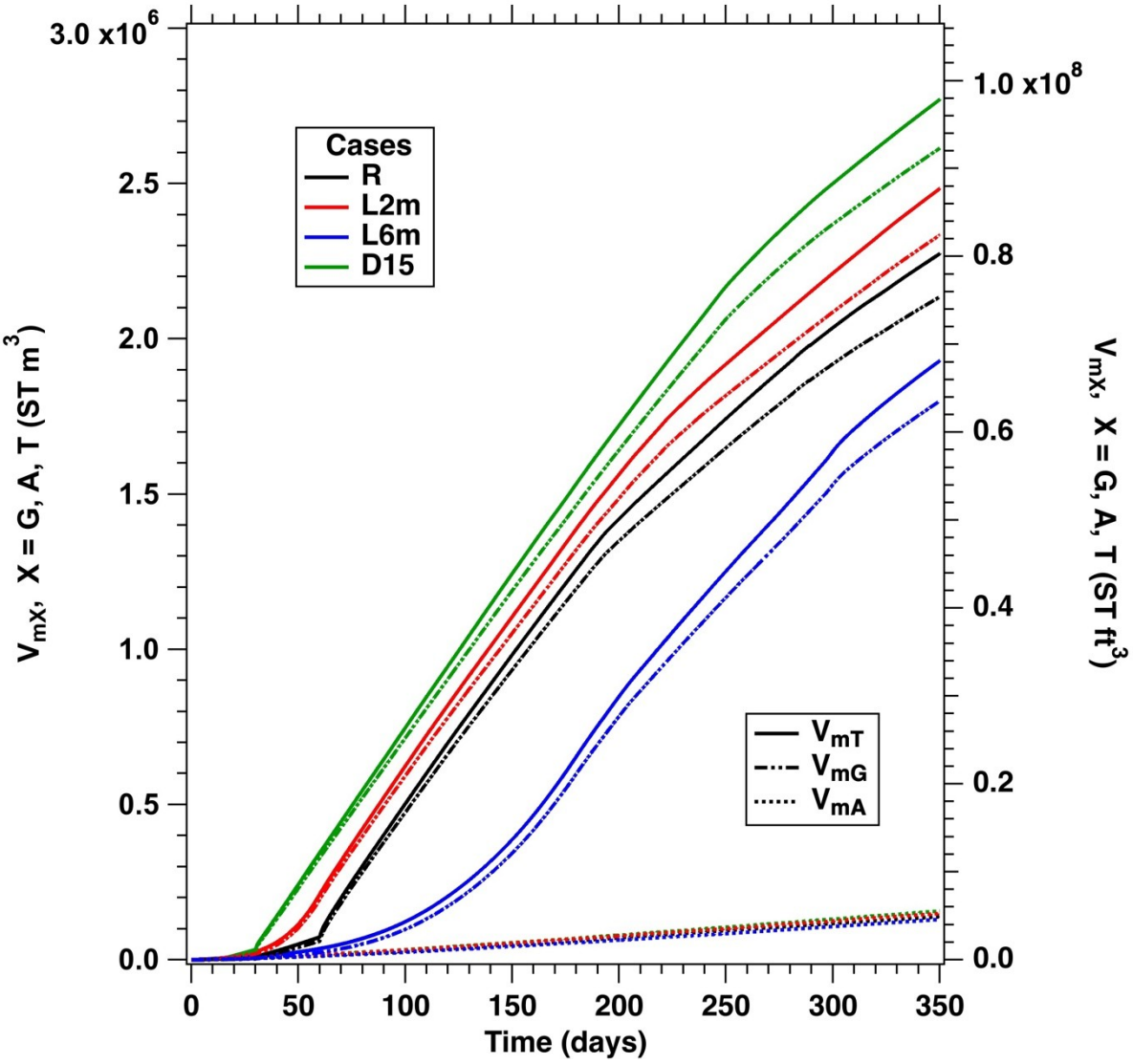

Figure 28. Cumulative volumes V_{mT} of the produced CH_4 in Cases R, L2m, L6m and D15, and the corresponding contribution of free gas and dissolved gas to production (V_{mG} and V_{mA}, respectively). The consistent dominance of V_{mG} in V_{mT} and the superiority of Case D15 are evident.

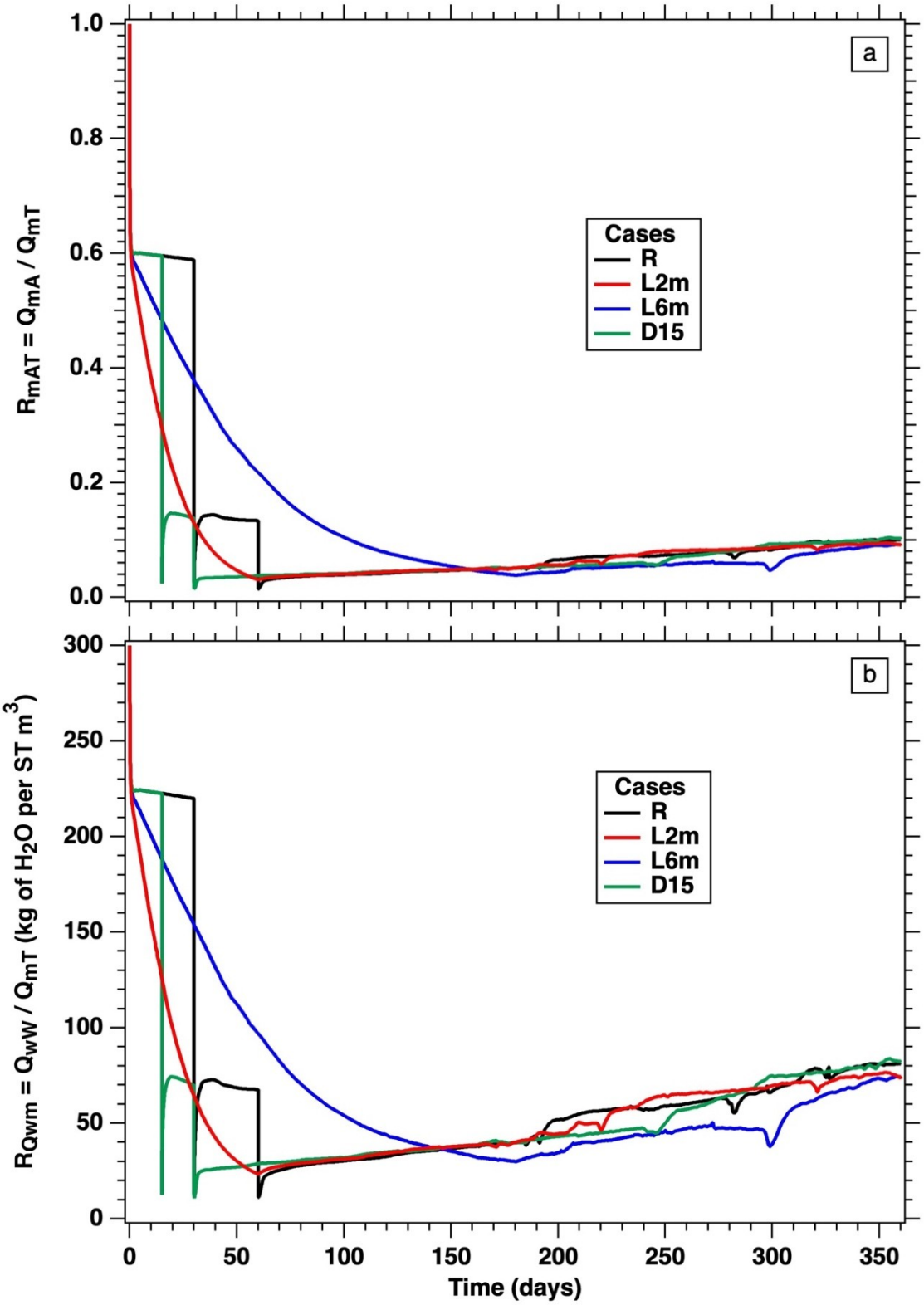

Figure 29. Cases R, L2m, L6m and D15:: Evolution of the (a) the aqueous CH_4 production fraction R_{mAT}, and (b) the corresponding instantaneous and cumulative water-to-gas ratio R_{Qwm} and R_{Mwm}, respectively.

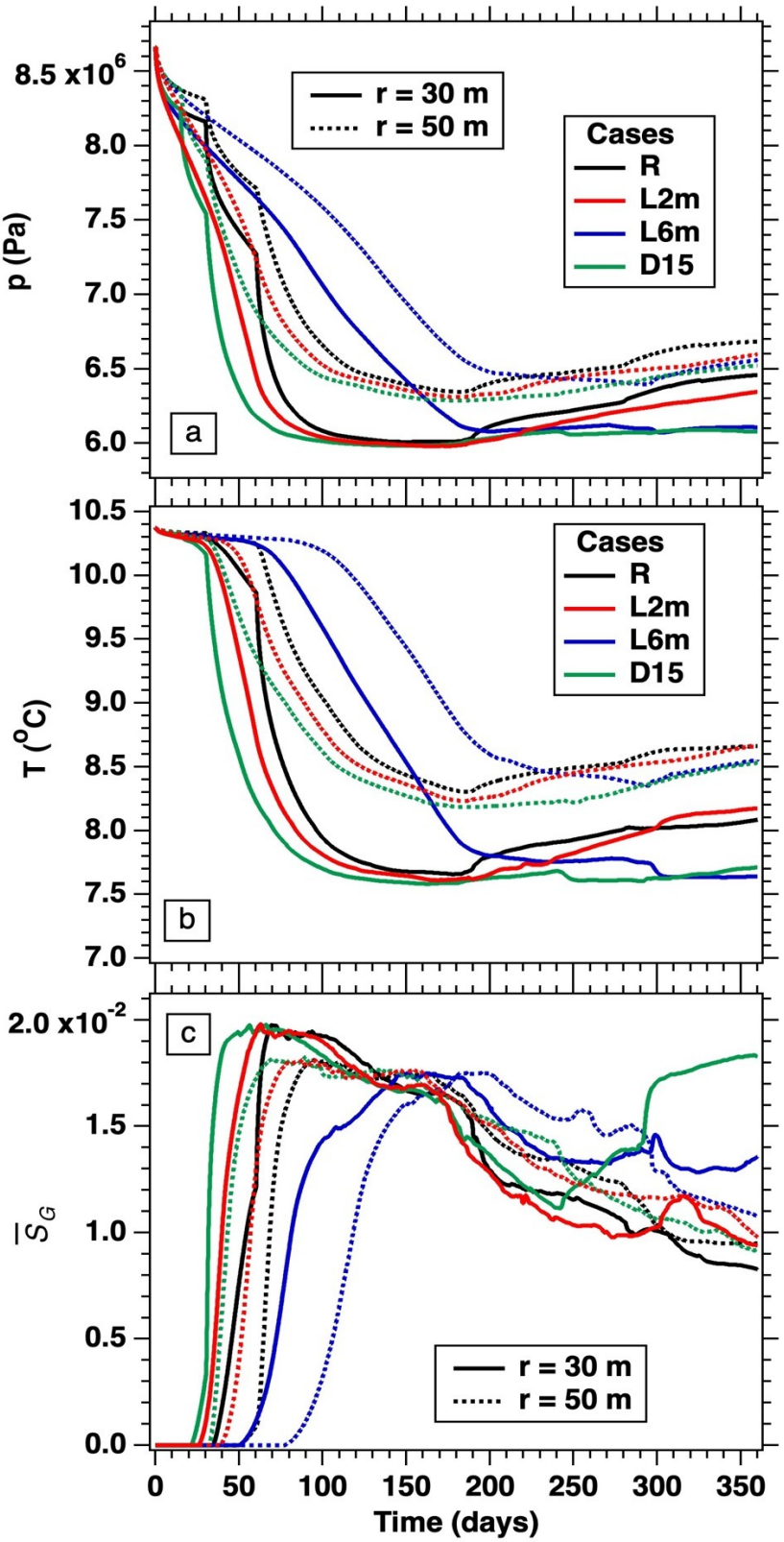

Figure 30. Evolution of (a) P, (b) T and (c) of the average gas saturation $\acute{S}_G$ at the observation wells during the production test in in Cases R, L2m, L6m and D15.

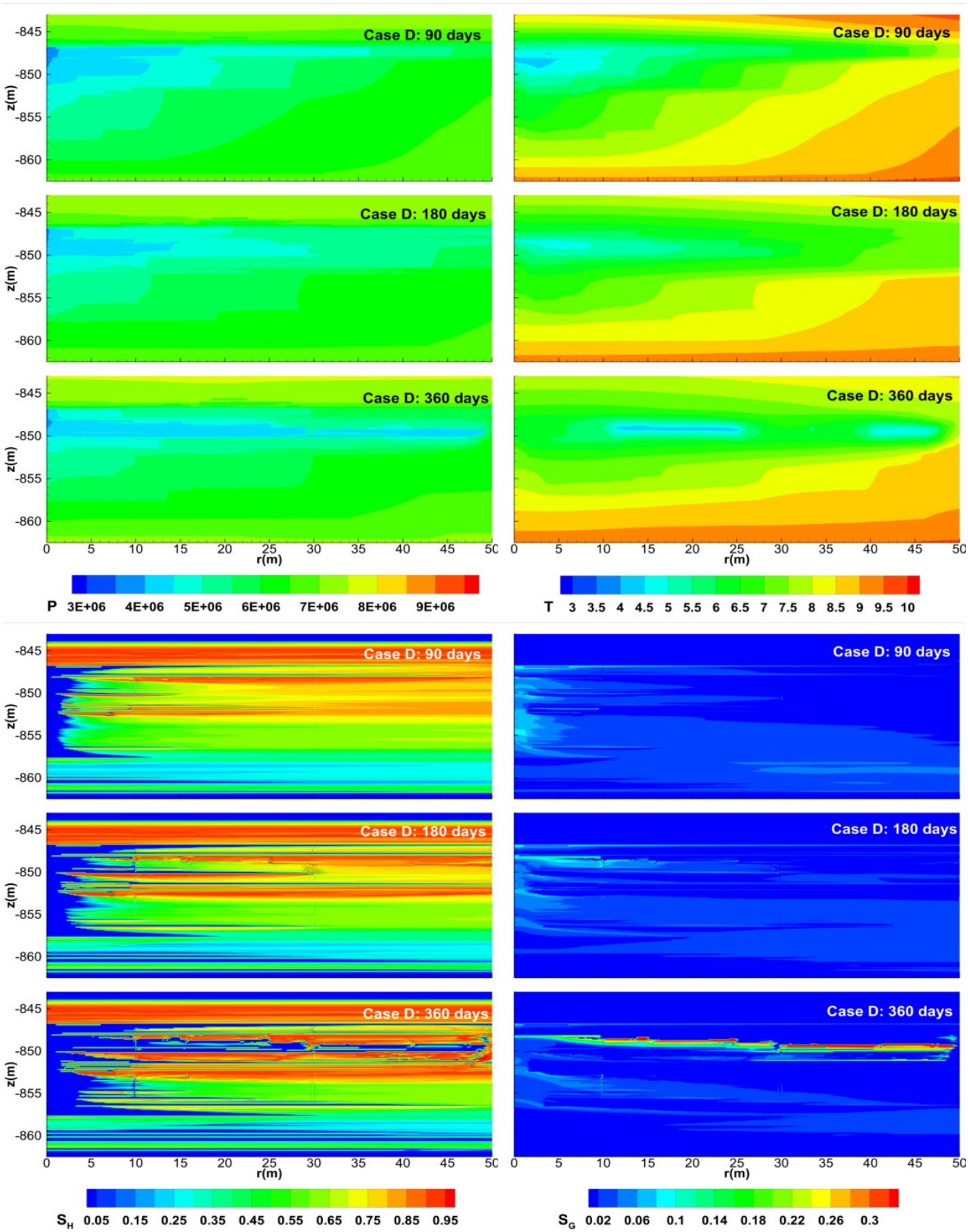

Figure 31. Case D15: Evolution over time of the spatial distributions of P (upper left), T (upper right), S_H (lower left) and S_G (lower right) in the vicinity of the production well.